Examination of high Reynolds number flow around a spinning cylinder with different turbulence models

Dávid Kármán

Supervisors: Dr. ir. I. Akkerman
Prof. dr. ir. R.H.M. Huijsmans
Dr. ir. M.J.B.M. Pourquie

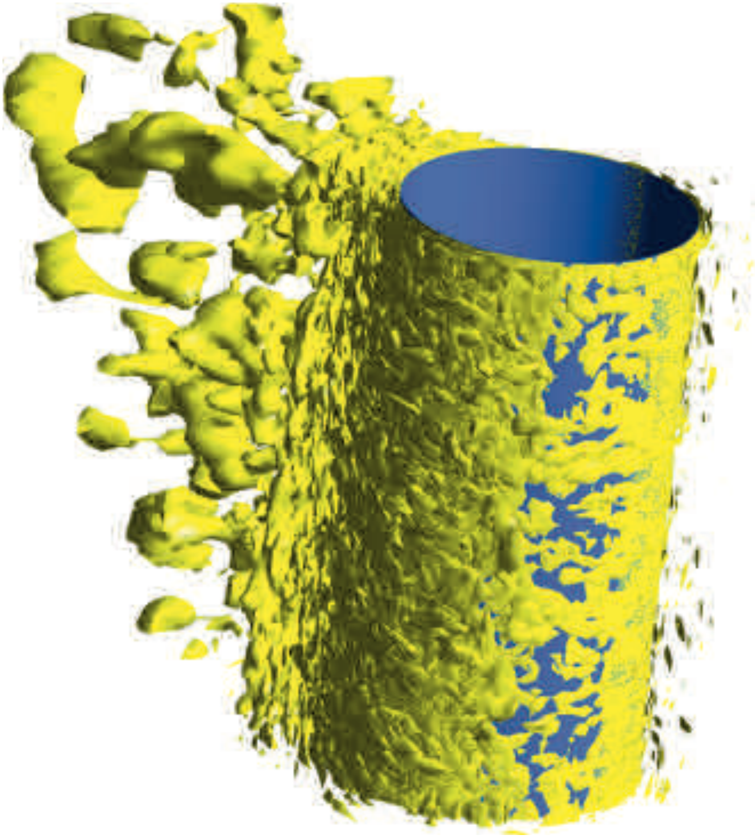

Delft University of Technology

Challenge the future

Thesis

Examination of high Reynolds number flow around a spinning cylinder with different turbulence models

by

Dávid Kármán

in partial fulfilment of the requirements for the degree of

Master of Science
in Ship Hydromechanics

at the Delft University of Technology,
to be defended publicly on Monday November 28, 2016 at 14:00.

Student ID:	4423364
Supervisors:	Dr. ir. I. Akkerman Prof. dr. ir. R.H.M. Huijsmans Dr. ir. M.J.B.M. Pourquie

This thesis is confidential and cannot be made public until November 27, 2016.

An electronic version of this thesis is avaiable at `http://repository.tudelft.nl/`.

Delft
University of
Technology

Contents

Abstract **viii**

1. Introduction **1**
- 1.1. Wind-assisted ship propulsion 1
- 1.2. Research at TU Delft and POLIMI 4
- 1.3. The main scope of the thesis 5
- 1.4. Case 6

2. Basic flow physics **9**
- 2.1. Flow around a stationary circular cylinder 9
- 2.2. Flow around a rotating circular cylinder 11
- 2.3. Boundary layer of the rotating circular cylinder 12

3. Summary of previous works **15**
- 3.1. Early works of flow around spinning cylinders 15
- 3.2. Works with low and moderate Reynolds number 16
- 3.3. Works with high Reynolds number 20

4. Numerical models **31**
- 4.1. Computational domain 31
- 4.2. Computational meshes 31
- 4.3. Boundary conditions 32
- 4.4. Turbulence models 33
- 4.5. Discretizational schemes 33
- 4.6. Simulation set-up 34

5. LES Results **35**
- 5.1. LES results at $\alpha = 2$ 35

6. RANS results **49**
- 6.1. Lift and drag coefficients 50
- 6.2. Velocities in the wake 53
- 6.3. Grid dependency 59

7. Conclusion and recommendation for further works **65**
- 7.1. Conclusion 65
- 7.2. Recommendations 67

Bibliography **69**

Appendices **71**

A. Turbulence modelling **73**
A.1. Introduction 73
A.2. Direct Numerical simulation (DNS) 75
A.3. Turbulence models 76

B. Velocities in the wake **105**

List of Figures

1.1. CO_2 emission from different ship types in 2012. Taken from: Third IMO Greenhouse Gas Study [1] 1
3figure.caption.6
1.3. Power saving diagram Taken from: Enercon E-Ship 1 [2] 4
1.4. Flettner-rotor and computational models 6

2.1. Evolution of the *Kármán-Bénard vortex street.* Taken from Homann [5] 9
2.2. Different flow regimes of flow around a stationary circular cylinder. Picture is taken from Mutlu and FredsØe, [6] 10
2.3. Representation of the flow around a slowly rotating cylinder. $Re = 40\,000$, $\alpha = 0.2$. Picture is taken from Swanson [7] 11
2.4. Nature of the boundary layer at different rotational ratios. Pictures are taken from Swanson [7] 12
2.5. Streamlines of an LES simuation of flow around a spinning cylinder. Cylinder rotates counterclockwise, flow comes from the left. $Re = 140\,000$, $\alpha = 1.3$. Taken from: Karabeles [8] 13
2.6. Streamlines of an LES simulation of flow around a spinning cylinder. Cylinder rotates counterclockwise, flow comes from the left. $Re = 500\,000$, $\alpha = 5$. Taken from: Rolfo et al. [9] 13
2.7. Velocity vectors in the boundary layer. Red dots: separation points, orange dot: stagnation point. 14

3.1. *Buckau*, the first rotor-ship in the history. The ship was constructed by the famous Germaniawerft (Germania shipyard). Taken from: Wikipedia 15
3.2. Locations of vorticity crests and valleys in the ensemble of 100 PIV snapshots: (+) positive vorticity; (◦) negative vorticity. Flow comes from the left, cylinder rotates clockwise. Taken from: Lam [15] 16
3.3. Variation of peak vorticity levels with downstream locations for vorticity crests and valleys. Positive vorticity (+) belongs to the lower side of the wake, whilst negative vorticity (◦) belongs to the upper side of the wake. Taken from: Lam [15] 17
3.4. Lateral profiles of mean streamwise velocity. Downstream stations at $x/D =$ 0.5, 1, 1.5, 2, ..., 5, 5.5, 6: first and last stations at $x/D = 0.5$ and 6 in bold lines. Taken from: Lam [15] 18
3.5. Computational grid and domain. Pictures are taken from Mobini and Niazi [16] 18
3.6. Velocity contours around the cylinder for the spin ratio of 1.5. Results are taken from: Mobini and Niazi [16] 19
3.7. Experimental results for the lift coefficient 22
3.8. Experimental results for the drag coefficient 23

3.9. Computational domain and grid. Picture is taken from Karabelas [8] 24
3.10. Streamlines for $0 \leq \alpha \leq 2$. Taken from Karabelas [8] 25
3.11. Magnitude of lift coefficients for $0 \leq \alpha \leq 2$. Taken from Karabelas [8] 25
3.12. Total resolved kinetic energy (k_f) for $0 \leq \alpha \leq 2$. Taken from Karabelas [8] . . 26
3.13. Kinematic Reynolds stress in the xy plane ($\langle u'v' \rangle$). Taken from Karabelas [8] 27
3.14. Computational mesh. Note presented results in thesis are from the bare cylinder case. Taken from Craft et al. [11] 28
3.15. Q-Criterion isosurfaces at $Q = -0.05$. $Re = 800\,000$, $\alpha = 5$. Flow comes from the left, cylinder rotates counterclockwise. Taken from Craft et al. [11] . 29
3.16. Streamlines at $Re = 140\,000$ and $\alpha = 5$. Flow comes from the left, cylinder rotates counterclockwise. Picture is taken from Craft et al. [11] 29
3.17. Numerical results for the lift coefficient 30
3.18. Numerical results for the drag coefficient 30

4.1. Examples for the computational meshes 32

5.1. Lift coefficients at $Re = 140\,000$ with $\alpha = 2$ 36
5.2. Drag coefficients at $Re = 140\,000$ with $\alpha = 2$ 36
5.3. Streamlines around the cylinder at $Re = 140\,000$ with $\alpha = 2$. Last picture is taken from Karabelas [8] 38
5.4. Positive and negative radial velocity areas around the upper half of the cylinder at $Re = 140\,000$ with $\alpha = 2$. Green: negative velocity, orange: positive velocity, blue: borderline 39
5.5. Mean peressure coefficients along the cylinder. Blue data set is taken from Karabelas [8] 40
5.6. Resolved turbulent kinetic energy (k_r) at $Re = 140\,000$ with $\alpha = 2$. Last picture is taken from Karabelas [8] 41
5.7. Kinematic Reynolds stresses at $Re = 140\,000$ with $\alpha = 2$. Last picture is taken from Karabelas [8] 42
5.8. A closer view on the resolved turbulent kinetic energy (k_r) on the top side of the cylinders. In the simulation: $Re = 140\,000$ and $\alpha = 2$. 43
5.9. Positive and negative tangential velocity areas around the upper half of the cylinder at $Re = 140\,000$ with $\alpha = 2$. Green: negative velocity, orange: positive velocity 44
5.10. Streamlines around the cylinder at $Re = 140\,000$ with $\alpha = 2$. 45
5.11. Resolved turbulent kinetic energy (k_r) at $Re = 140\,000$ with $\alpha = 2$. 45
5.12. Kinematic Reynolds stresses at $Re = 140\,000$ with $\alpha = 2$. 46
5.13. Subgrid viscosity ratios at $Re = 140\,000$ with $\alpha = 2$. 46

6.1. Examples for drag coefficient variations 50
6.2. Q-Criterion isosurfaces 52
6.3. Enercon E-Ship 1 53
6.4. Affected region 54
6.5. Position of the second cylinder and the ship 55
6.6. Velocities with R8 at 30° and 150°. 56
6.7. Velocities with R8 at 61° and 119°. 56
6.8. Velocities with R8 at 90° 56

6.9. Velocities with R9 at 30° and 150° 57
6.10. Velocities with R9 at 61° and 119° 57
6.11. Velocities with R9 at 90° 57
6.12. G7 the computational mesh for the coarse RANS runs 60
6.13. Velocities with R5 and R12 at 30° and 150° 62
6.14. Velocities with R5 and R12 at 61° and 119° 62
6.15. Velocities with R5 and R12 at 90° 62
6.16. Velocities with R9 and R13 at 30° and 150° 63
6.17. Velocities with R9 and R13 at 61° and 119° 63
6.18. Velocities with R9 and R13 at 90° 63

A.1. Schematic diagram of the energy cascade. Taken from Breugem [25] 74
A.2. Different scales in a turbulent mixing layer. Picture is taken from Van Dyke [28] 75
A.3. Stochastic signal and its decomposition. Upper picture: the signal itself, middle picture: the mean of the signal, lower picture: the fluctuating part of the signal. Taken from Breugem [25] 77
A.4. Profiles of the fractional contributions of the turbulent stress and viscous shear stress to the total stress. DNS data of Kim et al. [30]: dashed lines, Re = 5600; solid lines, Re = 13750. 83
A.5. Mean velocity profile of a smooth-flat-plate turbulent boundary layer plotted in log-linear coordinates with viscous scales normalizations. Taken from: Perlin et al. [31] 88
A.6. Different layers and regions in a turbulent boundary layer 89
A.7. Profiles of DNS of channel flow at Re = 13750. Results are obtained from Kim et al. [30] 90
A.8. Boundary layer modelling in FLUENT. Taken from: FLUENT User's Guide 12.10.1 [22] 92
A.9. Upper curves: a sample of the horizontal component of the velocity field $U(x)$ together with its filtered field $\overline{U}(x)$ (bold line), residual field $U^R(x)$ and the filtered field of the residual field $\overline{U^R}(x)$ (bold line). Taken from Pope [23] 95
A.10. LES statistics in two distinct flow types. Taken from: Pope 2004 [27] 97
A.11. The solution domain in wavenumber space for a DNS of isotropic turbulence. Only 0.016% of the modes lie within the sphere of radius K_{DI}, representing motions in the energy-containing range and in the inertial subrange. Taken from Pope [23] 98

B.1. Velocities with R1 at 30° and 150° 106
B.2. Velocities with R1 at 61° and 119° 106
B.3. Velocities with R1 at 90° 106
B.4. Velocities with R2 at 30° and 150° 107
B.5. Velocities with R2 at 61° and 119° 107
B.6. Velocities with R2 at 90° 107
B.7. Velocities with R3 at 30° and 150° 108
B.8. Velocities with R3 at 61° and 119° 108
B.9. Velocities with R3 at 90° 108
B.10. Velocities with R4 at 30° and 150° 109

B.11. Velocities with R4 at 61° and 119°. 109
B.12. Velocities with R4 at 90° 109
B.13. Velocities with R5 at 30° and 150°. 110
B.14. Velocities with R5 at 61° and 119°. 110
B.15. Velocities with R5 at 90° 110
B.16. Velocities with R6 at 30° and 150°. 111
B.17. Velocities with R6 at 61° and 119°. 111
B.18. Velocities with R6 at 90° 111
B.19. Velocities with R7 at 30° and 150°. 112
B.20. Velocities with R7 at 61° and 119°. 112
B.21. Velocities with R7 at 90° 112
B.22. Velocities with R8 at 30° and 150°. 113
B.23. Velocities with R8 at 61° and 119°. 113
B.24. Velocities with R8 at 90° 113
B.25. Velocities with R9 at 30° and 150°. 114
B.26. Velocities with R9 at 61° and 119°. 114
B.27. Velocities with R9 at 90° 114
B.28. Velocities with R10 at 30° and 150°. 115
B.29. Velocities with R10 at 61° and 119°. 115
B.30. Velocities with R10 at 90° 115
B.31. Velocities with R11 at 30° and 150°. 116
B.32. Velocities with R11 at 61° and 119°. 116
B.33. Velocities with R11 at 90° 116

List of Tables

4.1. Computational meshes . . . 32
4.2. Used turbulence models . . . 33
4.3. Spatial discretizational schemes. Note: Grad.: Gradient, Mom.: Momentum, CD: Central Differencing, LS: Least Square Cell Based . . . 33

5.1. Different LES runs . . . 35
5.2. Mean lift and drag coefficients. Exp.: experimental; N/D: no data . . . 37
5.3. Mean lift and drag coefficients. . . . 47

6.1. Different RANS runs . . . 49
6.2. Mean lift and drag coefficients. . . . 50
6.3. Coarser RANS runs . . . 60
6.4. Mean lift and drag coefficients with the original and the coarser mesh for the 3D unsteady runs with the $k - \omega$ and the RSM models . . . 60

7.1. Simulation times . . . 67

Abstract

> "Röviden: optimista vagyok. Hiszem, hogy jót hoz a jövő.
> És, ha csekély mértékben ehhez én is hozzájárulhattam,
> akkor meg vagyok elégedve."
> "Briefly: I'm optimistic. I believe in a bright future. And if I could contribute to this just a little bit, I'm already satisfied."
>
> *Theodore Von Kármán*

This thesis work is a starting point for the Flettner-rotor field of the wind-assisted ship propulsion research of TU Delft and POLIMI. During the development of this project, the flow around a bare spinning cylinder is investigated, introducing the Flettner-rotor without its end plate. The simulations were carried out in 2D and 3D with the commercial CFD package FLUENT 15. The main assumptions for the simulation are: the flow in the transcritical regime, a Reynolds number of 140 000, keeping the ratio between the cylinder's peripheral velocity and the incoming flow velocity in a value of 2.

As part of this project, comparisons among several turbulence models are performed. The models chosen are: the *Smagorinsky-Lilly*, the *Wall-Adapting Local Eddy-Viscosity (WALE)*, the $k-\epsilon$, the $SST\, k-\omega$ and the $RSM\, stress-\omega$. As a consequence of the rotational speed set for the simulation, the vortex shedding in the wake of the cylinder is suppressed, thus with the RANS models steady runs were also performed.

In high Reynolds number shear flows better accuracy is expected from the LES approach. In the first part of the project, an accurate LES run is sought. Afterwards, during the second part of the project, the evaluation of the RANS runs is based on the comparison with the reference LES results.

A new concept of the boundary layer around the spinning cylinder is introduced. This concept subdivides the boundary layer to an *inner portion* and to an *outer portion.* The inner portion moves bonded to the surface of the cylinder, while the outer portion flows in the direction of the free stream. The WALE analysis will show that only the outer portion should be turbulent. Contrary, the Smagorinsky-Lilly model produces a fully turbulent inner layer. The main difference between these two models is the lack of an appropriate damping in the near wall region for the subgrid viscosity in the case of the Smagorinsky-Lilly model. As an outcome of the simulations, it is shown that the turbulent boundary layer is significantly thicker. The thickness of the inner layer influences the pressure distribution around the cylinder, leading to differences in the aerodynamic forces for the two subgrid models.

A comparison between the RANS results and reference WALE is executed, based on the aerodynamic coefficients and the velocities in the wake. As a result of the simulations and comparison, the 2D steady $SST\, k-\omega$ model due to its prominent cost-accuracy ratio and the 3D unsteady $RSM\, stress-\omega$ model because of its accuracy are suggested for further work.

1. Introduction

1.1. Wind-assisted ship propulsion

Today, in an engineer's dictionary the expression environmental friendly has become as important as performance or cost-effectiveness. Indeed, if we do not create a sustainable future our beautiful Earth would be perished within a few hundred years. Probably one of the most known harmful effects to the environment is the global warming which is mainly caused by the augmented concentration of CO_2 in the atmosphere. The emission of CO_2 has been growing from the industrial revolution and it has been dramatically rising over the 20^{th} century. As a result, the total concentration of CO_2 in the atmosphere increased by almost 50% [1] from the start of the industrial revolution until 2015. A very significant part, almost 20% [2] of the total emission is attributed to the transportation sector, in which shipping plays a very important role. As stated in the Third IMO Greenhouse Gas Study [1] in 2012, 618 million tonnes of CO_2 were released to the atmosphere from the most typical ship types. In Figure 1.1 we can see that this is comparable with the total CO_2 emission of Central-Europe and the Baltics.

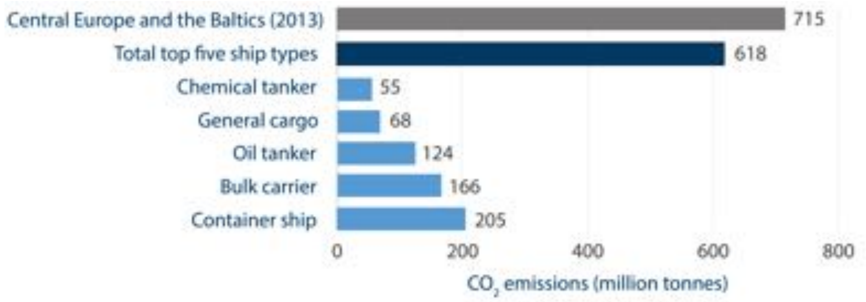

Figure 1.1.: CO_2 emission from different ship types in 2012. Taken from: Third IMO Greenhouse Gas Study [1]

It is important to mention that apart from CO_2 ships emit other pollutants as nitrogen oxides (NO_x) and sulfur oxides (SO_x) Besides, from a ship's engine hydrocarbons (HC), particulate matters (PM) and carbon-oxide (CO) are also discharged to the environment. NO_x itself is carcinogenic, moreover it reacts with sunlight and the outcome contains ground level ozone. Ozone is only desirable in the upper atmospheric region, since it causes respiratory problems in humans and damages plants. Furthermore, (NO_x) together with (SO_x) is the main contributor to acid rain. PM and HC are carcinogens and cause smog; finally CO

---

[1] Based on the data of National Oceanic and Atmospheric Administration (NOAA).

[2] According to the data of Emission Database for Global Atmospheric Research (EDGAR).

is only a very weak direct greenhouse gas, but it has important indirect effects on global warming. The above mentioned pollutants are the direct products of combustion. Every now and then a new International Convention for the Prevention of Pollution from Ships (MARPOL Convention) comes into force. These MARPOL Conventions are assigned to regulate the emission of pollutant materials. Thanks to these conventions over the last 20 years the amount of emitted pollutant materials has decayed significantly. Nonetheless, as long as we use combustion engines the augmentation of the concentration of CO_2 in the atmosphere is inevitable. Although alternative fuels have gained ground in the shipping sector, in the near future diesel engines as primary energy sources will remain dominant. Recently a new concept for the reduction of CO_2 emission started to spread in maritime design. *Wind-assisted ship design* as its name suggests, uses the the energy of the wind as an auxiliary power source, thereby mitigating the thrust requirement from the main engine so that its fuel consumption. However, wind-assisted ship propulsion as a technique itself is not new, it has already popped up in design as an economical alternative for the high crude oil prices. In 1973 the first oil crisis blew up the price of crude oil and the price of a barrel tripled in one year. Between 1975-1979 the prices kept growing, but in a significantly smaller pace, so the market was more or less stable. Nevertheless, in 1979 the second oil crisis came and the prices rocketed again. Altogether, from 1973 until 1980 the market experienced a 6-fold increase in the price of crude oil. In these times, ship owners were desperately seeking a new possibility to decrease the fuel consumption. Commercial vessels with huge sails and kites started to pop up on the oceans. Responding to a new demand of the market in design usually takes 3-4 years, conversely to set back the design to the original state just lasts for a moment. Wind-assisted ship design became the victim of this very simple phenomenon. By the time wind-assisted shipping would have spread the oil prices collapsed. In the beginning of the '80s company owners either did not know about the hazard of pollution or simply they ignored it, the only goal was to maximize the profit. As such, the interest towards these solutions has faded out. Nonetheless, nowadays in a sector like shipping where the vast amount of emission is that evident a company without an environmentally-aware profile cannot survive and hence wind-assisted ship propulsion has 'sailed' back to the picture. Although the base concept has not changed, the design has adopted the development of the last 30 years. The current solutions are typically fully automatised. The computers always set the propulsors to a thrust maximizing position. Moreover, the ship's track can also be optimized for the prevailing weather conditions, thus in this type of shipping 'the shortest is the cheapest' consideration almost never holds. The main types of the wind propulsors are listed below and in Figure 1.2 a realization for each type is depicted.

- *Wingsails*: rigid sails that are similar to airplane wings and are often used with flaps.
- *DynaRig*: a square shaped entirely automated canvas sail system, that has no rigging and is fully rotatable
- *Towing kites (SkySails)*
- *Flettner rotors*: cylindrical shaped spinning structures that deployed on the deck and spun by a built-in engine. The lift is generated via the Magnus-effect.

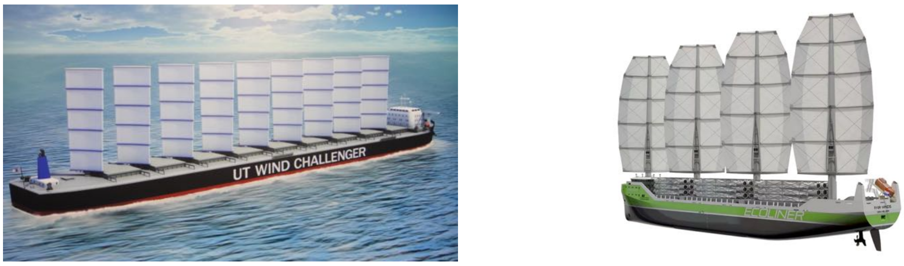

(a) Wingsails

(b) Dynarig

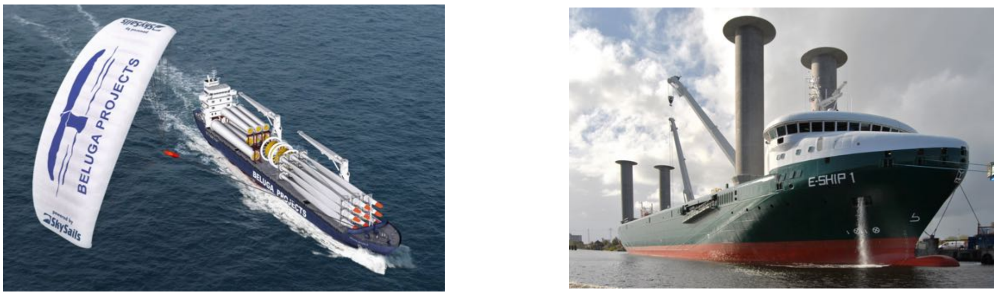

(c) Kite

(d) Flettner rotors

Figure 1.2.: Different wind-assisted sail propulsion designs [3]

As one can see the propulsors have large dimensions and (except the kite) are deployed on the deck of the ship. To allow passage under short constructions the system should be recovered in any case which is obtained through reefing (Dynarig, windsail, Flettner rotor), turning the propulsors down (Flettner rotor) or simply recover them (kite).

In Figure 1.3 an example for the power saving is shown. The graph belongs to the Enercon E-ship (Figure 1.2d), which operates with 4 Flettner-rotors. Obviously, like in sailing there is a limit in effectiveness with respect to the wind angle. Moreover, it is important to mention that due to the physics of Flettner rotors, they cannot produce thrust in 'running' either. Nonetheless, in the useful area the power saving percentage is almost always double-digit with a maximum of 45%. This double-digit fuel saving can easily be reached by any type of wind-assisted propulsion, this fact makes the concept of wind-assisted ship propulsion to be very promising.

---

[3] sources:
http://www.motorship.com/__data/assets/image/0021/411708/12.jpg
http://i0.wp.com/fairtransport.eu/wp-content/uploads/2014/03/Fairtransport-Ecoliner_aft.png?w=1080
https://commonknowledge.files.wordpress.com/2008/05/mv_beluga_skysails_16001.jpg
https://upload.wikimedia.org/wikipedia/commons/6/6e/Cargo_E-Ship_1,_Emder_Hafen,_CN-02.jpg

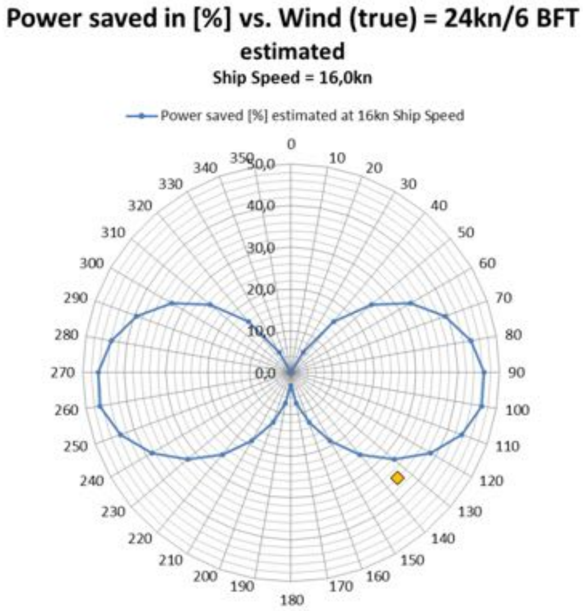

Figure 1.3.: Power saving diagram Taken from: Enercon E-Ship 1 [2]

1.2. Research at TU Delft and POLIMI

A shared research project between Delft University of Technology (TU Delft) and Politecnico di Milano (POLIMI) about wind-assisted ship propulsion launched in 2014. The research consists of two main areas:

– Examination of the aerodynamic interaction among the propulsors

– The effect of the propulsors on the hydromechanics behaviour of the hull (for instance ships with wind propulsors, similarly to sailing yachts, will operate under a heel angle)

The final goal of the project is to create a Power Prediction Program (PPP) which by analogy to Figure 1.3 would calculate the contribution of the auxiliary wind propulsors to the thrust force as a function of wind angle and speed. It is important to mention, that this PPP would be used in the preliminary state of the design. It would be a tool to the designer that allows to try out the effect of the number of propulsors and their positioning. As such, outstanding accuracy is not, but big freedom in terms of number, type and position of the propulsors is expected from such a prediction tool. The resultant aerodynamic force of the propulsors can be analytically calculated (with vortex methods) or it can be obtained via regression formulae. For the latter a built-in database which is filled up with results of wind tunnel experiments or CFD simulations is necessary. Obviously, the regression formulae would give higher accuracy. Nevertheless, as was mentioned above, in the PPP rather just an acceptable accuracy is the goal which might be achieved by the analytical results too. The vortex lattice method in the research of Caponetto [3] or the even simpler horseshoe vortex method in the paper of Roncin and Kobus [4] produced surprisingly good accuracy for the interaction of sailing yachts. Encouraged by these results, in the research vortex methods started to be put into use for wind-assisted sail systems (Wingsails, Dynarigs).

The accuracy of the methods will be tested with CFD simulations and with the wind-tunnel experiment which was carried out in Milan, in April 2016. The results of these examinations are still under evaluation when this thesis work is written. Unlike sails, Flettner rotors so far have not been investigated in the research of TU Delft and POLIMI and this thesis work is intended to be the starting point in this field. Here we should mention that in this work the Flettner rotor is introduced in a simplified form without the so-called *end plate*. The end plate is a circular disc at the end of the rotor with a diameter larger than the diameter of the cylinder. Consequently, this work examines the flow around a spinning bare cylinder. As one can see, testing the viability of the vortex methods is a very essential part of the research. However, it is important to note that this work will not deal with the testing of these vortex methods for rotors. The reason for this is quite simple: so far in the research neither numerical nor experimental results have been obtained for rotors. As such, the main goal here is to contribute to the build-up of an accurate CFD model with which the vortex methods would be compared in the future.

1.3. The main scope of the thesis

Flow around a stationary cylinder is probably one of the most examined problems in fluid dynamics and one can also find huge amount of research for the case of a rotating cylinder. However, Flettner rotors rotate relatively fast and their huge dimensions results in a Reynolds number [4] of the flow to order of one million even at a moderate apparent wind speed. Later we will see that the flow field around a spinning cylinder is strongly dependent on the Reynolds number as well as on the speed of rotation. Unfortunately, the number of published researches decreases radically when someone looks for cases from high Reynolds number and rotational speed. The situation is even worse if one seeks studies about interaction among spinning cylinders. To the author's knowledge there is no published work which examines the interaction of spinning cylinders in the high Reynolds and rotational speed regime. The lack of data for validation prevented this thesis work from starting the investigation immediately with the interaction of the cylinders and hence here only the flow around 1 cylinder will be examined. Furthermore, as we see later, already for 1 spinning cylinder there is only one experimental study where the speed of the cylinder and the Reynolds number of the flow at least are similar to the current simulation. Among the numerical works one finds mainly Reynolds Averaged Navier Stoke (RANS) models with one exception where Large Eddy Simulation (LES) was considered. In the present problem the strong shear layer in the wake of the cylinder suggests that the LES technique will give superior results to the RANS results.

If in the future it turns out that neglecting turbulence completely poses a huge error on the interaction then the idea of vortex methods should be discarded and a built-in database for the PPP will be inevitable. Unfortunately, the cost of LES simulations is orders of magnitude higher than the cost of RANS simulations. Consequently, this database can only be produced by experiments or by RANS simulations. Therefore, the main goal of this work is to examine how different RANS models perform on this type of flow. This will be realized through the following:

---

[4] In the thesis: $Re = \frac{UD}{\nu}$, where U: free stream velocity, D: diameter of the cylinder, ν: kinematic viscosity of the fluid.

1. We seek an LES model which is as accurate as possible
2. With the same domain type RANS runs will be performed and the results will be compared with the reference LES run. Paying in mind that in the future work cylinders will be placed in the wake of the investigated cylinder, in the comparison the main interests are:
    - lift and drag coefficients with different models
    - the velocities in the wake

Although it is not listed above, the cost of the RANS simulation is also a very important question, that will also be taken into account in the final evaluation. In the end of this work an accurate and a economicRANS model will be suggested for the future, interaction involving work.

1.4. Case

Figure 1.4 shows a typical Flettner-rotor and the cylinders that were used for the simulations. In the simulations the free stream is coming in the horizontal direction (along the x axis), while the cylinder rotates counterclockwise around its vertical axis ($\vec{\omega} = (0, 0, \omega_z)$).

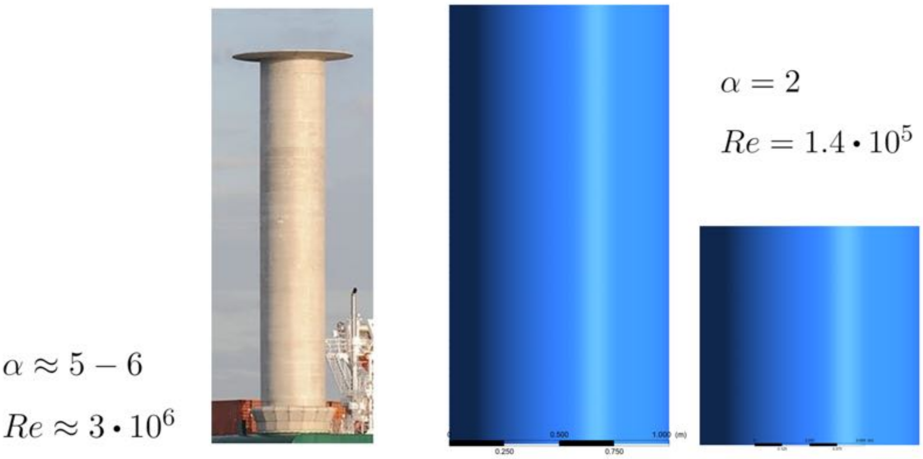

(a) Flettner-rotor with its operational condition

(b) Models and operational regime for the CFD simulations

Figure 1.4.: Flettner-rotor and computational models

Apart from the lack of the end plate another big difference is present in the aspect ratio. In the current simulation it is imagined that the cylinder is built up from segments, like those that are depicted in Figure 1.4b and whose height is either 1 or 2 cylinder diameter. Furthermore, the flow field is considered to be the same in each segment, which means in practice that a 'periodic boundary condition' was used on the top and bottom face of the domain. Consequently, the aspect ratio in the simulations is infinite. With the above described simulation set up, the mean velocity of the flow in the third direction is expected to be statistically zero ($\langle w \rangle = 0$). Nevertheless, real 3 dimensional (real in a sense that they are not extruded 3D structures from a 2D base, such as a vortex street behind a stationary cylinder in low Reynolds number flow) are expected to develop in the wake. The 3 dimensionality of the domain therefore is intended to make possible the evolution of these structures. In Figure 1.4 one can see that the Reynolds number and the rotational *rotational ratio*[5]: α, which is the ratio between the circumferential velocity of the cylinder and the free stream velocity has been changed too. Both are scaled down by an order of magnitude for the simulation. The reasons behind the choice of $Re = 140\,000$ and $\alpha = 2$:

- Doing LES simulations with Reynolds number of the order of one million is still very challenging because of the high involved costs.
- Most of the numerical studies are from that particular Reynolds number, rotational speed pair
- As we will see in the following chapter the nature of the flow around a spinning cylinder is the same for the two sets of Reynolds number rotational ratio pairs depicted in Figure 1.4

---

[5] In the thesis, the names: *rotational rate* or *rotational speed* will also be used for α.

2. Basic flow physics

2.1. Flow around a stationary circular cylinder

Flow around bluff bodies, especially around cylinders is a widely investigated area of fluid dynamics. Already at $Re = 4 - 5$ flow separation happens from the surface of the cylinder. The two shear layer demarcate the wake and meet downstream in the so called *confluence point.* The bounded near wake cannot remain stable for $Re > 30 - 40$ and sinusoidal oscillation of the vortex trail starts in the confluence point (Figure 2.1a). The amplitude of the oscillation grows with Reynolds number and finally for $Re > 40 - 65$, the shear layers roll up and the well-known *Kármán-Bénard vortex street* (Figure 2.1b) [1] starts evolving. With further increasing the Reynolds number a beautiful staggered array of laminar eddies form the wake (Figure 2.1c).

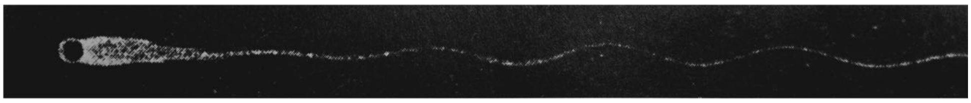

(a) Oscillating vortex trail. $Re = 54$

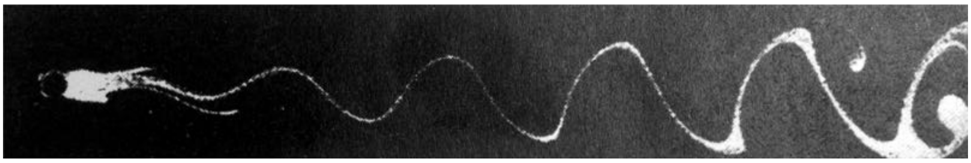

(b) Evolving vortex street. $Re = 65$

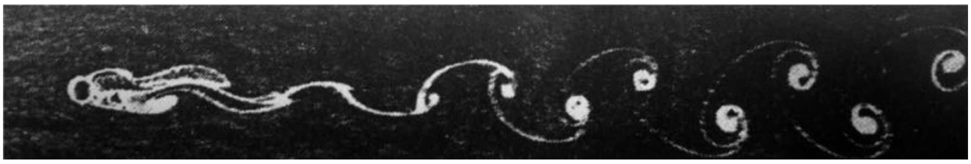

(c) Developed vortex street. $Re = 102$

Figure 2.1.: Evolution of the *Kármán-Bénard vortex street.* Taken from Homann [5]

As we can see the wake behind the cylinder is strongly dependent on the Reynolds number. In Figure 2.2 the different wake patterns for different Reynolds regimes are summed up.

---

[1] Henri Bénard was the first who visualised the vortex street in 1908, whilst Theodore von Kármán provided a descriptive mathematical model (by means of stability analysis) for the phenomena in 1911.

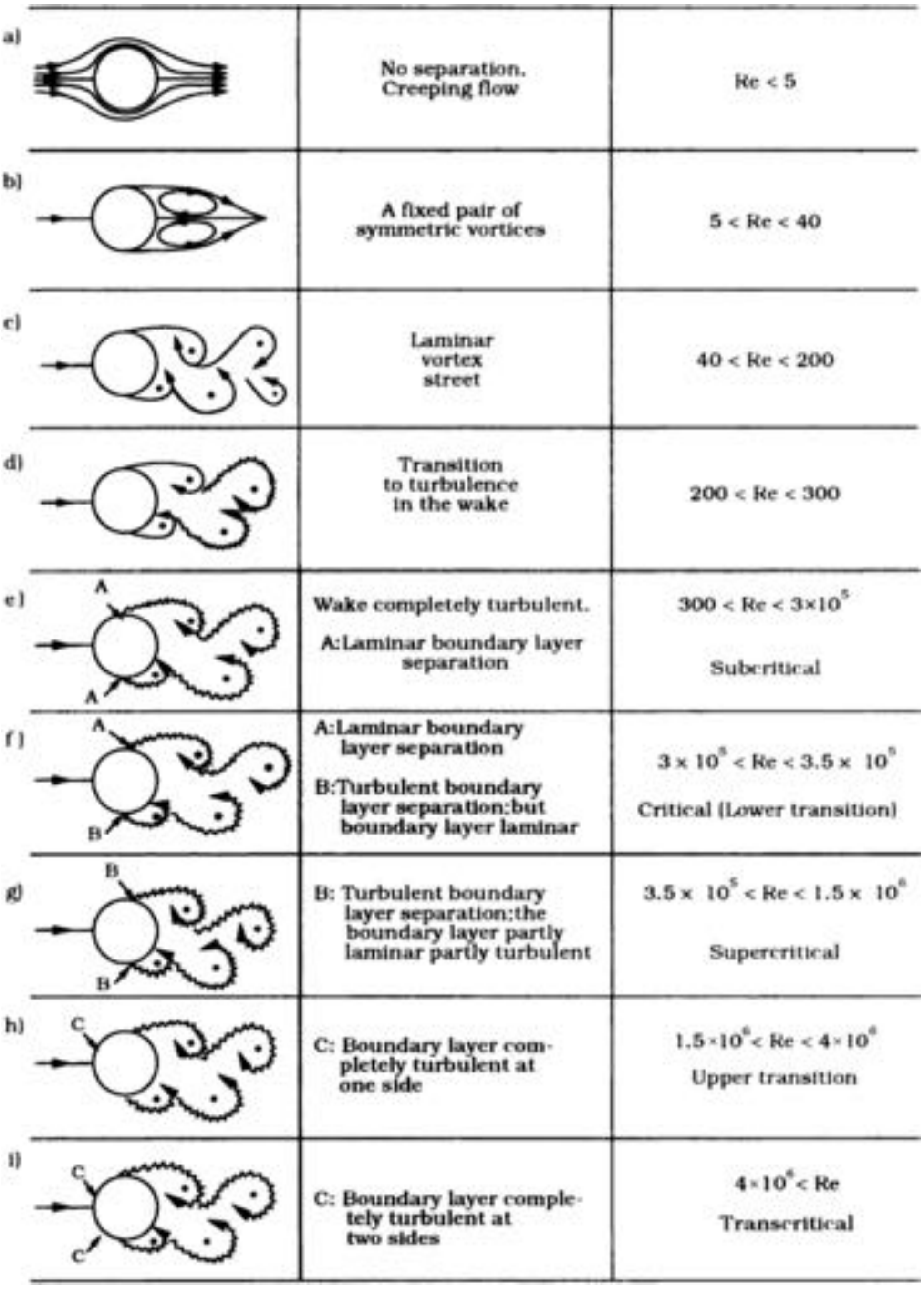

a)	No separation. Creeping flow	Re < 5
b)	A fixed pair of symmetric vortices	5 < Re < 40
c)	Laminar vortex street	40 < Re < 200
d)	Transition to turbulence in the wake	200 < Re < 300
e)	Wake completely turbulent. A:Laminar boundary layer separation	$300 < Re < 3\times10^5$ Subcritical
f)	A:Laminar boundary layer separation B:Turbulent boundary layer separation:but boundary layer laminar	$3\times10^5 < Re < 3.5\times10^5$ Critical (Lower transition)
g)	B: Turbulent boundary layer separation:the boundary layer partly laminar partly turbulent	$3.5\times10^5 < Re < 1.5\times10^6$ Supercritical
h)	C: Boundary layer completely turbulent at one side	$1.5\times10^6 < Re < 4\times10^6$ Upper transition
i)	C: Boundary layer completely turbulent at two sides	$4\times10^6 < Re$ Transcritical

Figure 2.2.: Different flow regimes of flow around a stationary circular cylinder. Picture is taken from Mutlu and FredsØe, [6]

The first 3 pictures were already described above. The transition from laminar to turbulent flow happens first in the wake further downstream of the cylinder at Re $\approx$ 200. Subsequently, the transition gradually spreads upstream until at $Re \approx 300$ it already occurs during the formation of the vortices. Once the wake becomes fully turbulent, transition gains ground in the shear layers too. After the wide transitional regime of the shear layers the vortex street becomes fully turbulent at $Re \approx 3 \cdot 10^5$. Finally, transition takes place in the boundary layer. Vortex shedding dies out during this last process, nonetheless, it is re-established after the boundary layer arrives at a fully turbulent stage (transcritical regime) at $Re \approx 4 \cdot 10^6$. The turbulent boundary layer is capable of staying attached longer to the surface than the laminar one, thereby reducing the width of the wake and allowing a higher pressure regain at the back of the cylinder. As a result a sudden decrease in the drag coefficient can be seen after the boundary layer starts becoming turbulent, this phenomenon is known as *drag crisis*. In the transcritical regime the drag coefficient grows with Reynolds number up to a certain limit and finally it becomes independent of the Reynolds number.

2.2. Flow around a rotating circular cylinder

The flow field around a smooth, infinite length rotating cylinder is dependent on the Reynolds number as well as on the rotational-ratio.

Due to the rotation of the cylinder, the free stream flow experiences deceleration on the side which rotates against: *pressure side*, whilst acceleration on the side which rotates with the free stream: *suction side*. The velocity difference on the 2 sides of the cylinder implies a pressure drop which yields a lift force. The pressure drop along the cylinder forces the free stream to bend toward the lower pressure side, hence demolishes the statistical streamwise symmetry of the wake around the centerline of the cylinder. Besides, with the increase of the rotational speed the stagnation point moves azimuthally downstream and further from the cylinder on the side which rotates opposite to the free stream (on the pressure side). As a result, the vertical component of the resulting pressure force along the cylinder grows, while the horizontal reduces. In flow around stationary or spinning cylinders the pressure forces have a significantly larger contribution to the aerodynamics forces than the frictional forces, thus the lift coefficient increases, whilst the drag coefficient reduces with α. Furthermore, it was found that the rotating cylinder only produces vortex shedding until a critical rotational velocity: α_c. α_c is a function of Re number, usually with a value approximately 2. Figure 2.3 sums up the above mentioned considerations for a slowly rotating cylinder:

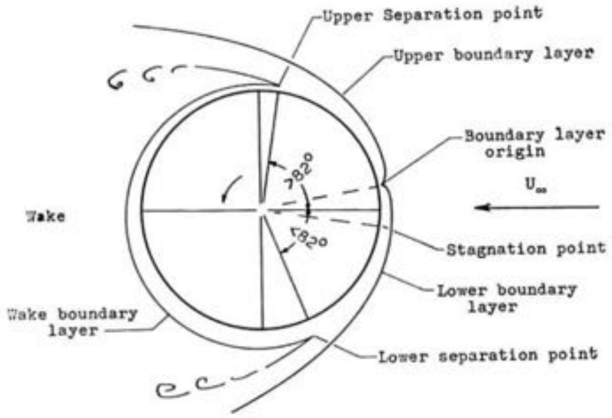

Figure 2.3.: Representation of the flow around a slowly rotating cylinder. $Re = 40\,000$, $\alpha = 0.2$. Picture is taken from Swanson [7]

2.3. Boundary layer of the rotating circular cylinder

The boundary layer around a spinning cylinder is of special interest. The rotation forces the stagnation point to move azimuthally to a greater angle and away from the cylinder surface (see explanation later) at the side where higher pressure is present. The transition from laminar to turbulent as well as the separation points are functions of the boundary-layer length Reynolds number. In aerodynamics, in case of flow around stationary bodies the origin of the boundary layer is defined to the stagnation point. However, in a spinning cylinder case the rotation introduces an additional shear on the free stream flow. As a result, at the stagnation point the cylinder moves exactly with the same speed but opposite to the direction of the bulk. Another problem with considering the stagnation point as origin is that the stagnation point no longer lays on the cylinder's surface. Therefore, it is more logical to place the boundary layer origin at the point where the relative velocity between the cylinder's surface and the fluid velocity is zero. Figure 2.4 shows the velocity profiles around the cylinder for two rotational rates:

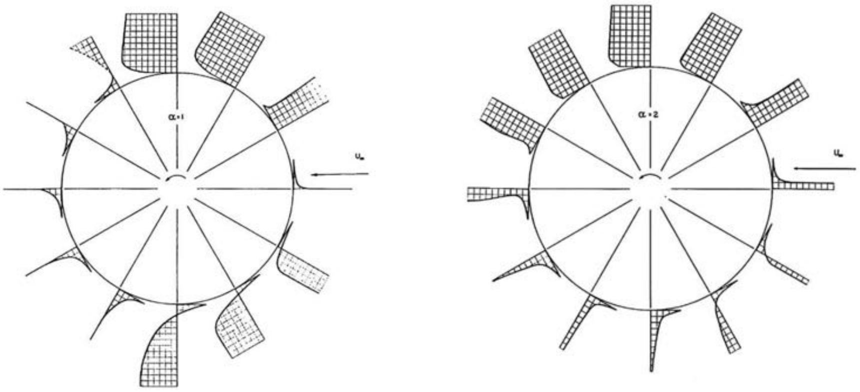

(a) Nature of the boundary layer at $\alpha = 1$

(b) Nature of the boundary layer at $\alpha = 2$

Figure 2.4.: Nature of the boundary layer at different rotational ratios. Pictures are taken from Swanson [7]

The rotating wall drags the fluid in the vicinity of the cylinder's surface forming the *inner portion* of the boundary layer, what we call rotating boundary layer (RBL). RBL increases the velocity of the flow through entrainment on the side which rotates in favour of the free stream (suction side), hence causing a general deflection of the wake. On the opposite side (pressure side) the free stream slides over the RBL, which triggers the transverse deflection of the free stream. In Figure 2.5 one can see that even at a moderate rotational speed, the stagnation point is pushed away from the cylinder's surface. Besides, the separation point on the lower pressure side (suction side) and the corresponding vortex formation are also moved away from the cylinder.

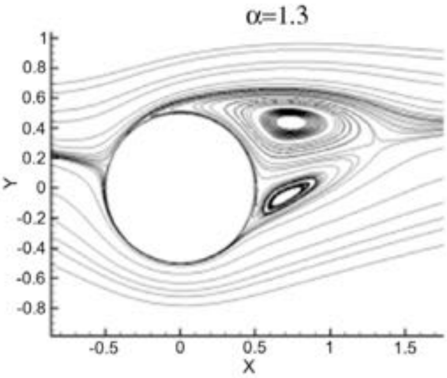

Figure 2.5.: Streamlines of an LES simulation of flow around a spinning cylinder. Cylinder rotates counterclockwise, flow comes from the left. *Re* = 140 000, $\alpha = 1.3$. Taken from: Karabeles [8]

Furthermore, with further increase of the rotational speed, after a certain point the rotational boundary layer will possess everywhere higher velocities than the velocity of the free stream. As a result the separation point on the high pressure side likewise moves away from the cylinder's surface allowing an evolution of a continuous RBL along the surface of the cylinder. Such a situation is depicted below:

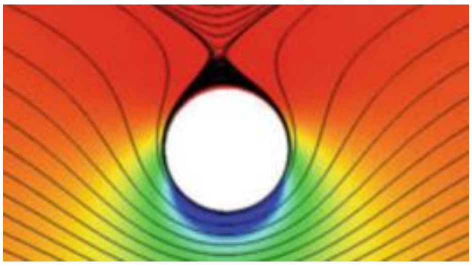

Figure 2.6.: Streamlines of an LES simulation of flow around a spinning cylinder. Cylinder rotates counterclockwise, flow comes from the left. *Re* = 500 000, $\alpha = 5$. Taken from: Rolfo et al. [9]

So far we have introduced the RBL, the part of the boundary layer which is the direct consequence of the rotation. However, if we are strict to the common definition of the boundary layer, then the boundary layer should end where the velocity in the boundary layer is 99% of the free stream velocity. Consequently, RBL is just the *inner portion* of the total boundary layer. Apart from the RBL, the total boundary layer consists of an *outer portion*, which comes from the free stream. Depending on the location this outer portion slides over or slides with the RBL. In between the two portion a shear layer or a recirculation region is present. To have a better imagination of the portions, Figure 2.7 shows a velocity plot in the boundary layer. The results belong to one of the LES simulation of the thesis and depicts a situation where only a strong shear layer is present between the portions. As we will see later such a velocity plot belongs to a region before separation on the front cap of the top side of the cylinder.

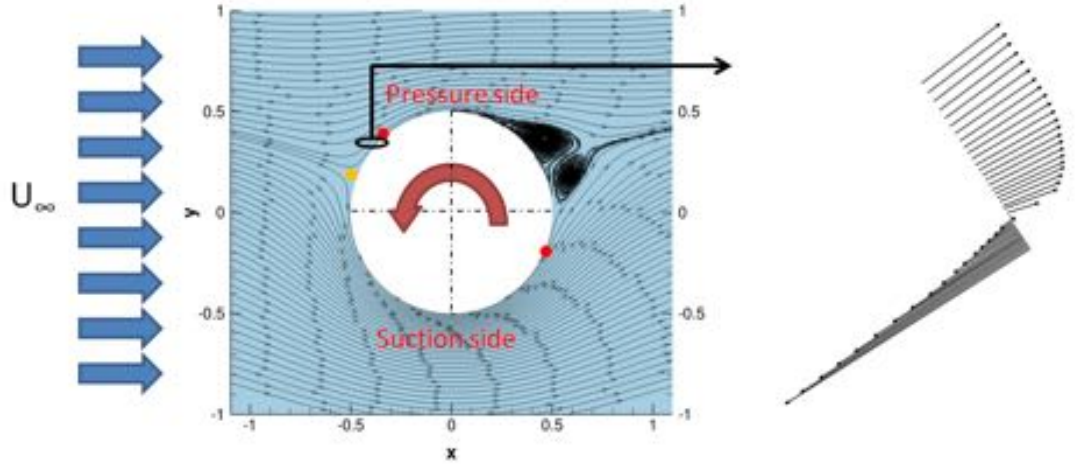

Figure 2.7.: Velocity vectors in the boundary layer. Red dots: separation points, orange dot: stagnation point.

The drag reduction due to laminar to turbulent boundary layer transition for a stationary cylinder was introduced in the previous section. In the stationary case the flow is symmetrical, thus transition statistically happens at the same angle on both sides of the cylinder. However, the situation is different for rotating cylinders because of the RBL. RBL moves with the incoming flow on the suction side, hence the relative velocities in the shear layer of the boundary layer are decreased, conversely the relative velocities are increased on the pressure side. Consequently, the local Reynolds number in the shear layer of the pressure side is higher. As such, transition first occurs on the pressure side and it is delayed on the suction side. It is crucial to point out here that the transition happens in the shear layer. Turbulence is introduced to the flow in the shear layer and makes the outer portion of the boundary layer to be turbulent. However, the inner portion, the RBL which moves bonded to surface of the cylinder should not to be turbulent. Indeed, as we will see later, the fact whether the RBL is modelled as laminar or turbulent would make substantial differences in the results! After transition in the outer portion on the pressure side, a longer attached boundary layer and hence a bigger area of suction is present on this side which results in a lift reduction. This reduction can be as big to change the sign of the lift! In the transitional regime the boundary layer is very vulnerable even for the smallest disturbances. The RBL transports turbulence from the pressure side and hence it feeds with disturbances the incoming flow. As a result, laminar to turbulent transition starts in the outer portion on the suction side as well. Finally, the effect vanishes once the outer portions of the boundary layers become fully turbulent on both sides. In literature the above described phenomena is called *Inverse Magnus Effect.* The effect already occurs for $Re = 35\,800$. It is more pronounced for lower rotational rates and for $\alpha \geq 1$ it totally disappears.

3. Summary of previous works

3.1. Early works of flow around spinning cylinders

Flow around spinning cylinders has first become of interest to researchers in the middle of the 1920's. Anton Flettner designed his first rotor ship: *Buckau* in 1924 which was a refitted schooner with 2 rotors approximately 15 metres high, and 3 metres in diameter:

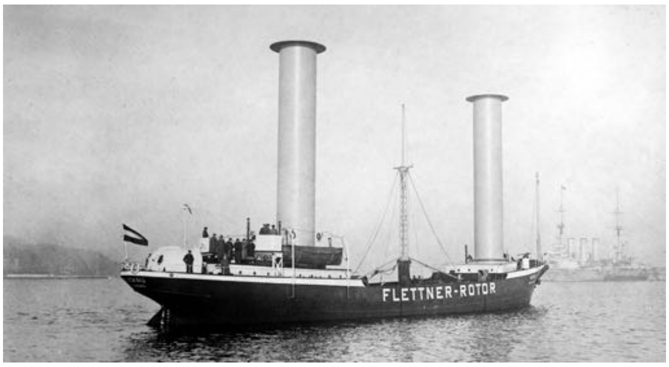

Figure 3.1.: *Buckau*, the first rotor-ship in the history. The ship was constructed by the famous Germaniawerft (Germania shipyard). Taken from: Wikipedia

In the design of Buckau Ludwig Prandtl also took part. He was devoted to have a better insight in the flow physics, thus he carried out his first experiments with spinning cylinders in 1925. Prandtl [10] from his experimental results determined the maximum lift coefficient as $c_l^{max} = 4\pi$. Although recent studies have revealed (for instance Rolfo [9] or Craft et al. [11]) that he had been incorrect in terms of the maximum obtainable lift coefficient, his works and Flettner's successful crossing of the Atlantic Ocean (already with his new ship: *Barbara*), had encouraged other scientists to work on the problem. One of the most interesting experiments was done by Thom [12] in 1934. He examined the flow around a Flettner rotor as well as a case where he added evenly distributed discs with a diameter of the original rotor's end plate to the cylinder's surface. For rotational speeds greater than 4 he found a radical lift increase for the cylinder equipped with discs. Unfortunately, recent studies like Clayton [13] or Craft et al. [14], [11] have not had success in reproducing the very promising phenomeon reported by Thom. Just after that *Barbara* has sailed in the history, diesel engines started to gain ground in marine propulsion as well. Albeit, rotor-ships were faster than sail-boats, they were still dependent on the weather conditions. As a result of this, the interest towards Flettner rotors, and hence towards spinning cylinders has faded out. After a long break, the oil crisis in the 1970's has brought back wind-assisted ship propulsion to the picture. Nevertheless, as it was already mentioned in the introduction, the oil prices had collapsed and the interest has disappeared again. Finally, the last revolution of wind-assisted ship propulsion started in the 2000's and it is still lasting. This is due to the fact that now the main aim is to reduce the emission of CO_2 which is an environmental goal. Of course, in research a similar trend can be observed. When there is interest in design more paper are released and hence most of the papers that will be introduced subsequently are from the 2000's.

3.2. Works with low and moderate Reynolds number

Lam [15] carried out PIV measurements on a flow around rotating cylinders. The Reynolds number ranged from 3600 to 5000 and α was from 0 to 2.5. Although this Reynolds regime is almost 2 orders of magnitude smaller than the regime of the current simulation, his work is very important since he made extensive observations on the wake topology. He found that as α increases the wake deflects towards the pressure side and also gets narrower, besides the two vortex trails get closer together. Furthermore, he measured that the vortex shedding frequency slowly increased with α up to $\alpha_c = 2$ where finally the shedding died out. In a stationary cylinder case a distance of 2.5 D was needed behind the cylinder for the formation of the large-scale vortices which are then shed in the form of a vortex street, for the spinning case this distance became smaller as α raised. These findings are depicted below:

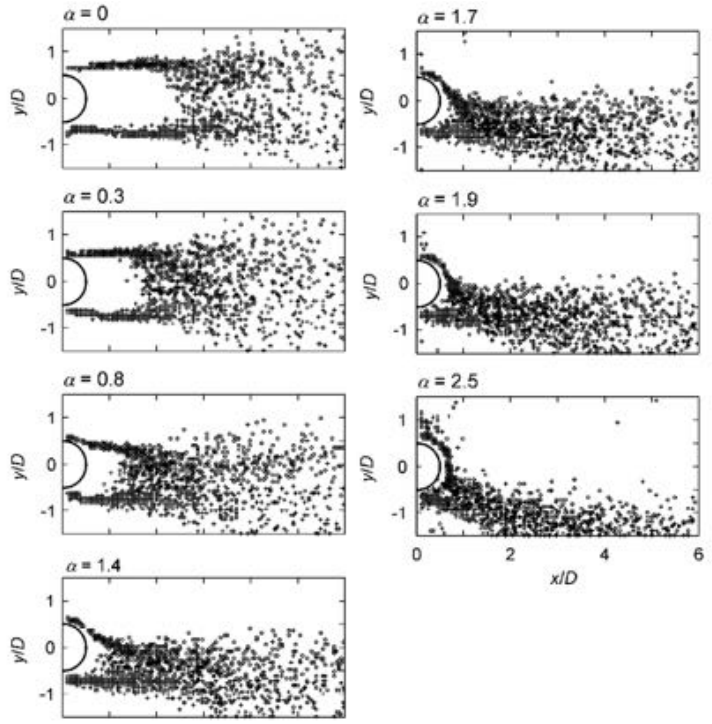

Figure 3.2.: Locations of vorticity crests and valleys in the ensemble of 100 PIV snapshots: (+) positive vorticity; (∘) negative vorticity. Flow comes from the left, cylinder rotates clockwise. Taken from: Lam [15]

He also observed a significant diminution in the strength of the vortices which was associated with the smaller size and lower vorticity magnitudes of the vortices. The reduction in size is explained by the higher shedding frequencies which yield a growth in the convection speed of the vortices. Due to the faster convection, the large-scale vortices cut off faster from the shear layers. Consequently, the size of the large-scale vortices diminishes tremendously with α.

The findings for the vorticity levels are summed up in Figure 3.3.

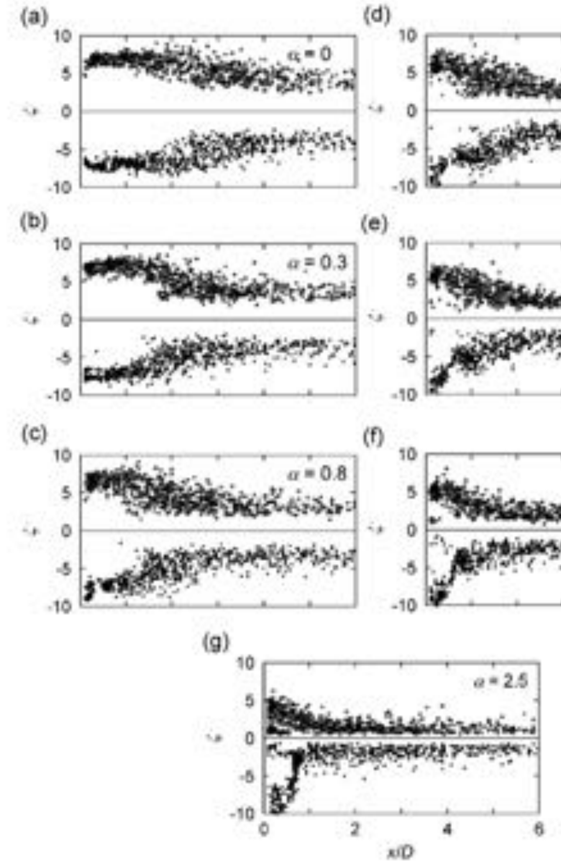

Figure 3.3.: Variation of peak vorticity levels with downstream locations for vorticity crests and valleys. Positive vorticity (+) belongs to the lower side of the wake, whilst negative vorticity (○) belongs to the upper side of the wake. Taken from: Lam [15]

The rotation results in a stronger shear layer and thus in higher vorticity magnitudes just behind the cylinder on the upper trail, nevertheless after cutting off there is no supplier shear layer anymore, the vortex starts diffusing, and the vorticity magnitudes drops down. As a result, the average vorticity magnitudes of the large-scale vortices reduce too. It is also important to mention that the shed vortices along the two trails possessed fairly equal strength at particular rotational rates.

Lam also measured that the wake behind a rotating cylinder recovers at a much faster rate as α increases. This finding is shown in Figure 3.4

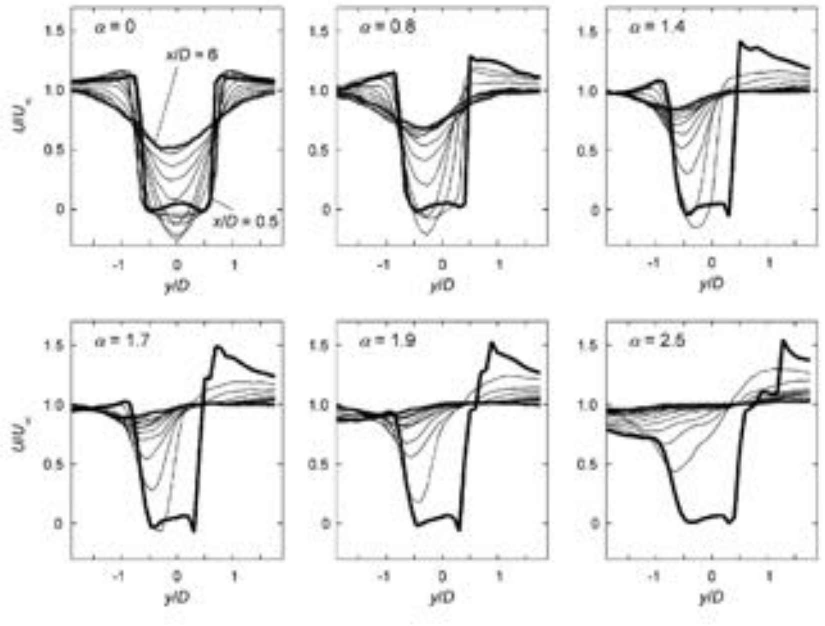

Figure 3.4.: Lateral profiles of mean streamwise velocity. Downstream stations at $x/D = 0.5, 1, 1.5, 2, \ldots, 5, 5.5, 6$: first and last stations at $x/D = 0.5 \, \text{and} \, 6$ in bold lines. Taken from: Lam [15]

Although Lam described extensively the wake topology, he did not publish any results either for the pressure distribution along the cylinder's surface or for the aerodynamic forces. The next important work is the numerical study of Mobini and Niazi [16]. They carried out Large Eddy Simulation (LES) of a spinning cylinder at $Re = 3\,900 - 10\,000$ with α ranging from 0 to 2. In the simulation a modified Smagorinsky model which accounted for the near wall regions through a Van Driest damping function was used. A rectangular domain shown in Figure 3.5a was considered, the extension in the spanwise direction was πD.

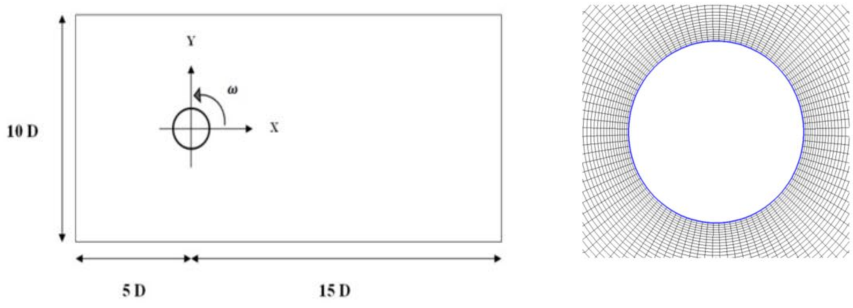

(a) Computational domain

(b) Grid in the vicinity of the cylinder

Figure 3.5.: Computational grid and domain. Pictures are taken from Mobini and Niazi [16]

A uniform inflow condition was imposed to the inlet boundary, while at the outlet, the flow is assumed to be fully developed. Symmetry conditions were used on the side walls and periodicity was assumed to the spanwise direction. The computational mesh consisted of 108 800 cells, it was of C type with O type refinement (shown in Figure 3.5b) in the near cylinder area. A fully implicit finite volume method was used to solve the unsteady 3 dimensional incompressible Navier-Stokes equations. For the spatial and time discretization central differencing scheme with second order accuracy was considered.

At this Reynolds regime the nature of the flow is *subcritcal* i.e. the boundary layer on the surface is entirely laminar, however once the separation happens the flow becomes turbulent and unstable. For higher rotational speeds, similarly to Lam [15] they also observed a narrower wake with weaker and smaller vortices. However their simulation also revealed that the length of the vortices grew with the rotational speed so that they became elongated. For higher Reynolds number the inclination of the wake reduced, while the wake was even more stretched. These results can be examined in the following velocity plots:

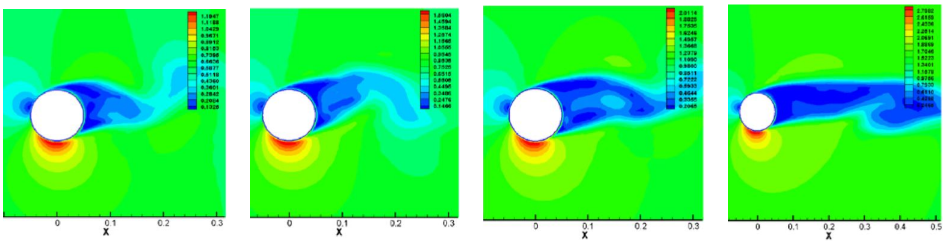

(a) $Re = 3\,900$ (b) $Re = 5\,000$ (c) $Re = 7\,000$ (d) $Re = 10\,000$

Figure 3.6.: Velocity contours around the cylinder for the spin ratio of 1.5. Results are taken from: Mobini and Niazi [16]

In the report, the effect of the Reynolds number as well as the rotational rate on the aerodynamic forces were also examined. The following results were found:

- c_l increases with α
- c_l decreases with Re
- c_d decreases with α
- c_d decreases with Re

For higher α's the increase in c_l and the diminution in c_d are due to the azimuthally greater dislocation of the stagnation point and the corresponding displacement of the high pressure area.

However, the location of the stagnation point is expected to be approximately constant at a particular α regardless of the Reynolds number. The unchanged location of the stagnation point is related to the fact that the angular velocity grows on the surface with Re (provided that α and ν are constant). The higher angular velocity tends to increase the azimuthal displacement of the stagnation points while the larger Reynolds number implies higher velocities on the surface of the cylinder and hence the stagnation point is dragged more upstream, so that the two effects cancel each other out. As such, the variation in c_l and c_d with Re should be explained by the changed wake area. The decline in c_l with Re is due to the reduced inclination of the wake. The higher Re number free stream basically blows away the wake, hence making the separation retarded on the pressure side which results in an extended suction area and lower pressure on this side. The decrease in c_d at higher Reynolds number is associated with the fact that if the Reynolds number augments the wake becomes more stretched and narrower. Therefore, at the back of the cylinder the overall pressure increases which results in drag reduction. changed wake area behind the cylinder.

3.3. Works with high Reynolds number

In the main simulations of the thesis the two parameters were chosen to be: $Re = 140\,000$ and $\alpha = 2$. According to Figure 2.2 at $Re = 140\,000$ the boundary layer is fully laminar in the stationary case. However, if the cylinder rotates, as we saw in the description of the boundary layer, the outer portion of the boundary layer is already fully turbulent at $Re = 35\,800$ for $\alpha \geq 1$. Consequently, with $Re = 140\,000$ and $\alpha = 2$ the simulations will be in the transcritical regime. The current computations can only be directly compared with numerical results since there are no available experimental results for this particular Reynolds number and α pair. Nevertheless, as long as the flow is in the transcritical regime, experimental results can be used for validation. Thus, a first part of this section sums up few experimental works and the second part will give an insight into relevant numerical studies.

3.3.1. Experimental studies with high Reynolds number

The first important experimental results are from Reid [17]. He carried out experiments with Reynolds number: 32 000, 45 000, 64 000 and 96 000. The rotational ratio was ranged from 0 to 4.32. The length-diameter ratio of the cylinder was infinite. Although the results are very old, they show good agreement (except in the transitional period) with other experimental data. Furthermore, the biggest value of the paper is that it gives results for $\alpha \leq 1$ as well (we will see later that, unfortunately, this is not always the case).

Swanson [7] was the first who ever measured the inverse Magnus effect. In his study the Reynolds number ranged from 35 800 to 501 000 and the rotational rate from 0 to 1. The cylinder had infinite span length. It was found that the inverse Magnus effect already appears for Reynolds number as low as $Re = 35\,800$ and it is still visible at $Re = 501\,000$. Moreover between the values $Re = 120\,800$ and $Re = 501\,000$ it is that strong to even be capable of swapping the sign of the lift! The first occurrence of the effect depends on the Reynolds number and α. Although in the measurements depending on the Reynolds number there was big variation in the starting point ($\alpha = 0\,..\,0.5$), the effect ended for all Reynolds number at $\alpha = 0.9$. Once the effect died out he found Reynolds number independent lift coefficients. The azimuthally greater location of the stagnation point as α increases and the inverse Magnus effect both have drag reducing effect, thus in the c_d measurement the effect was not shown that distinguishable.

Aoki and Ito [18] carried out experiments for $Re = 60\,000$ and $Re = 140\,000$ with $0 \leq \alpha \leq 1$ (c_l at $Re = 140\,000$ was only measured for $\alpha \leq 0.5$ though). Apart from the experiments they also made an attempt to attain same results numerically. The inverse Magnus effect was successfully captured by the experiments, however the numerical model has failed to reproduce it. The experimental results showed a similar trend to Swanson's results, nonetheless the effect started at higher α and for $Re = 60\,000$ the lift reduction was not as noticeable as in Swanson's experiments. In the numerical simulation the 2D unsteady Navier-Stokes equations, using the RNG $k-\epsilon$ turbulence model were solved with a fully implicit finite volume method in FLUENT. For the spatial derivatives the first order upwind, while for time derivatives first order implicit scheme were used. The velocity-pressure coupling was realised by the SIMPLE method. A rectangular domain was used, uniform horizontal velocity with 1% turbulent intensity was imposed on the left vertical edge as an inflow condition, at the right vertical edge a pressure outlet of $p = 0$ was considered. The top and bottom horizontal edges were treated as walls. Their mesh was unstructured and consisted of about 52 000 grid cells. As it was anticipated, the wall functions were incapable of dealing with the curved transitional boundary layer. As a result, the numerical simulation showed a totally different trend from the experimental results in the transitional regime. Moreover, the computation significantly overpredicted the lift and underpredicted the drag coefficients for α's at which the inverse Magnus effect was already not shown by the experiments. This was the first indication that RANS models have difficulties with handling the transitional boundary layer and they might give overpredicted lift for the fully turbulent state.

Badalamenti and Prince [19] recently performed experiments on spinning cylinders. The main purpose of their experiments was to investigate the effect of mounting endplates to the cylinders, thus they worked with a finite cylinder height (AR[1] $= 5.1$). The Reynolds number was ranged from 16 000 to 95 000 while α is from 0 to 8. The inverse Magnus effect was captured for $Re = 72\,000$ and for 92 000. The lift coefficients showed an outstanding agreement with other experimental data up to $\alpha = 1.5$, then the effect of the finite length became more pronounced. Interestingly, the c_l curve plateaued at 4.5 at $\alpha = 3$. Such a limit of c_l is not indicated in other studies and it is presumed to be present here due to the relatively low aspect ratio. By contrast, the drag curves not gave back that accurate results and showed discrepancy with the reference values even for low rotational ratios. However, it is important to note that to accurately measure the drag is more challenging than the lift and there is a big scatter among other experimental data as well.

The most relevant experimental results from the above mentioned four experiments in terms of lift and drag coefficients are depicted below:

---

[1] In the thesis AR: aspect ratio

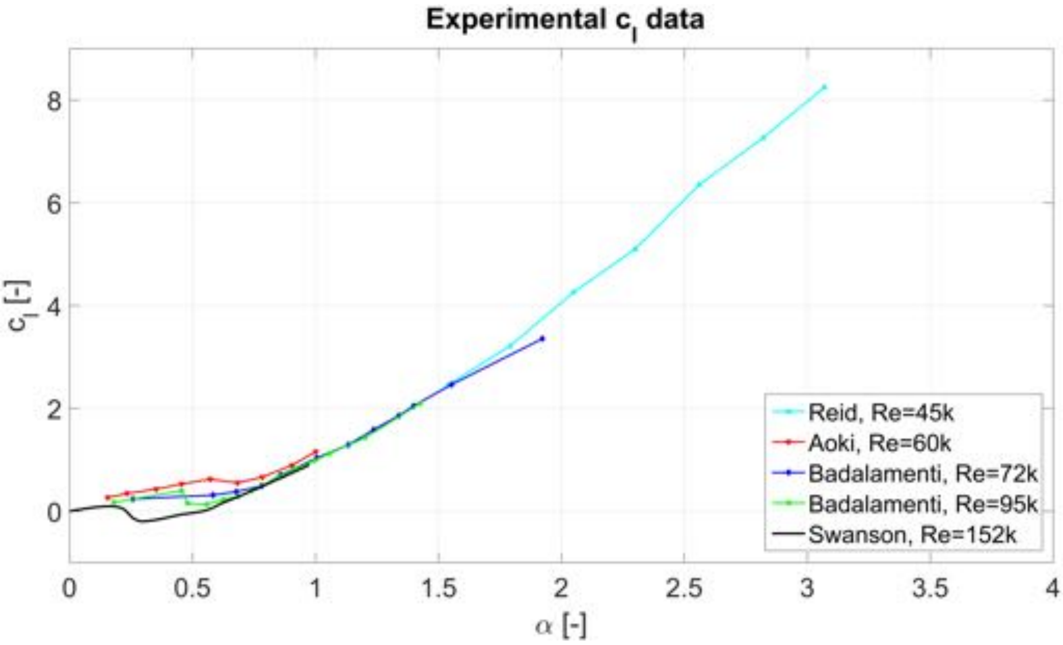

(a) Results up to $\alpha = 1$

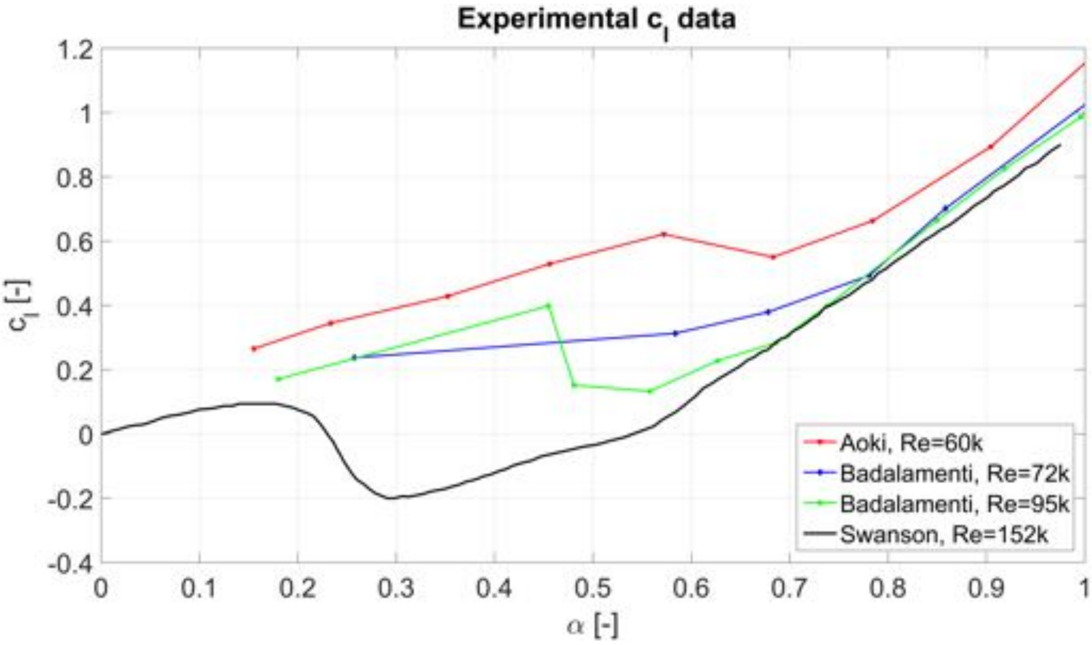

(b) Results for higher α's

Figure 3.7.: Experimental results for the lift coefficient

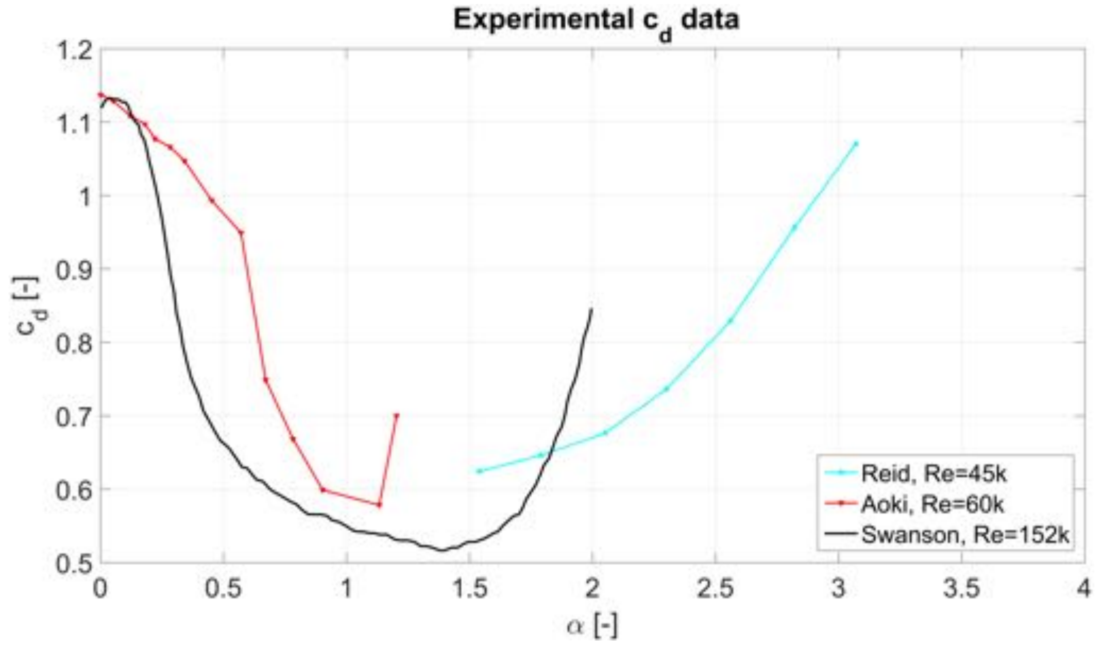

Figure 3.8.: Experimental results for the drag coefficient

3.3.2. Numerical studies with high Reynolds number

In the past 10 years simulations of high Reynolds number flow around spinning cylinder gained ground in CFD. The University of Manchester made special efforts to use URANS for the simulation of the flow around Flettner rotors and as a starting point the bare cylinder situation was always published. The rationale behind URANS is that Flettner rotors are operating at higher rotational rates, at $\alpha \approx 5-7$, where the transition of the boundary layer has surely happened and a fully turbulent boundary layer is present around the cylinder. Consequently, URANS models only need to handle the larger scale turbulence at the shear layer in the wake (which is by the way still challenging for them). Nonetheless, if we speak about shear layers at high Reynolds number Large Eddy Simulation seems to be the best choice (see explanation in the "Required resolution for LES" section of A.3.3). LES might also tackle the boundary layer transition, provided that the turbulent kinetic energy is well resolved in the near wall area. Apart from the work of Manchesterian scientists, in 2010 Karabelas [8] published his LES study of a flow around a spinning cylinder. In this section a brief summary of the above mentioned articles will be given.

LES study of flow around a spinning cylinder

Karabelas [8] carried out LES simulation of flow around a spinning cylinder for $0 \leq \alpha \leq 2$ at Reynolds number of 140 000. The domain is of O-type with local refinement close to the surface of the cylinder. Its size is $L = 20\,D$ in the radial and $z = 1\,D$ in the axial direction. In the z direction 32 equivalent layers are distributed uniformly. Each layer contains 125 points in the radial as well as 125 in the azimuthal direction, resulting in a total of 500 000 grid points. The resolution of the grid close to the surface of the cylinder is such that

$y^+ < 5$ everywhere for each rotational ratio. Figure 3.9 depicts the computational domain with the grid:

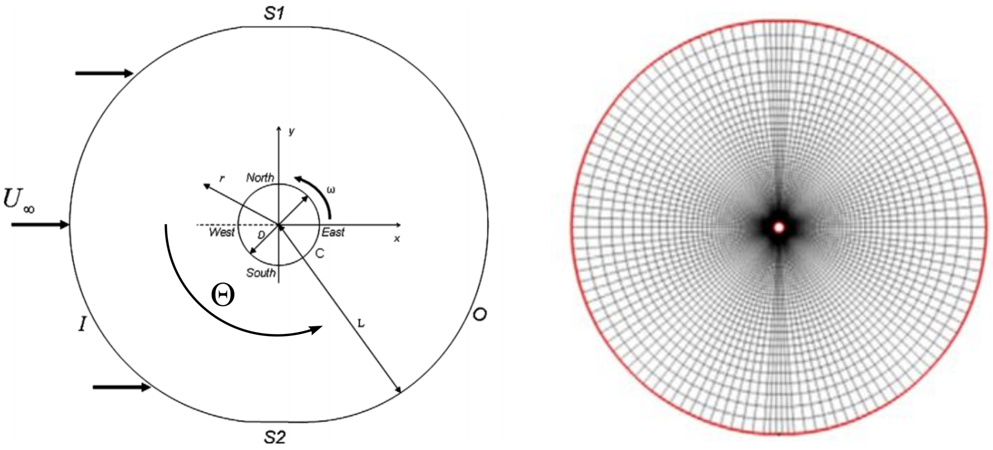

(a) Computational domain (b) Computational grid

Figure 3.9.: Computational domain and grid. Picture is taken from Karabelas [8]

A uniform, perturbation free horizontal velocity inlet is imposed on the inflow I boundary, far away from the cylinder on S_1 and S_2 symmetry condition is applied while on O an outflow condition is prescribed. On the surface of the cylinder (C) the velocity is $\vec{U} = \left(\frac{\alpha U_\infty}{R}\right)\hat{z} \times \vec{r}(x,y)$ (where $\hat{z}$ is the unit vector in the z direction). Finally, periodicity of the flow is assumed in the spanwise direction. In FLUENT 6.3 the 3 D incompressible time-dependent Navier-Stokes equations were solved. Finite-volume discretization was applied to the governing equations, a central differencing scheme was used for the spatial and fully implicit second order scheme for the time discretization. In each time step the pressure correction was carried out by the PISO velocity-pressure coupling. For the subgrid-scale modelling FLUENT's Smagorinsky model (see in A.3.3 "Implementation in FLUENT, the WALE model") was used. In the simulation the dimensionless time-step was $dt' = dt\frac{U_\infty}{D} = 0.001$, with this time-step the Courant–Friedrichs–Lewy Number (CFL number) was kept below 1 everywhere in the solution domain.

Figure 3.10 depicts the streamlines for each rotational rate. In the stationary case two vortices of equal form are seen, but once the cylinder starts rotating the deflection of the wake towards the pressure side is evident. RBL on the pressure side pushes away the incoming flow allowing hence a more expanded vortex formation on the top. Contrary, on the suction side the flow is dragged with the RBL causing the contraction of the lower vortex. The $\alpha = 2$ is of special interest for this thesis work. At this rotational speed the upper vortex is found to be not as elongated as it was expected to be from the previous results, nevertheless the deflection of the wake is still the greatest at this speed. The lower vortex is totally collapsed, which was explained by the combined action of the position of the upper vortex together with the high momentum of the fluid coming from the suction side. The stagnation point was found to be at $\theta = 332^\circ$ and dislocated from the cylinder.

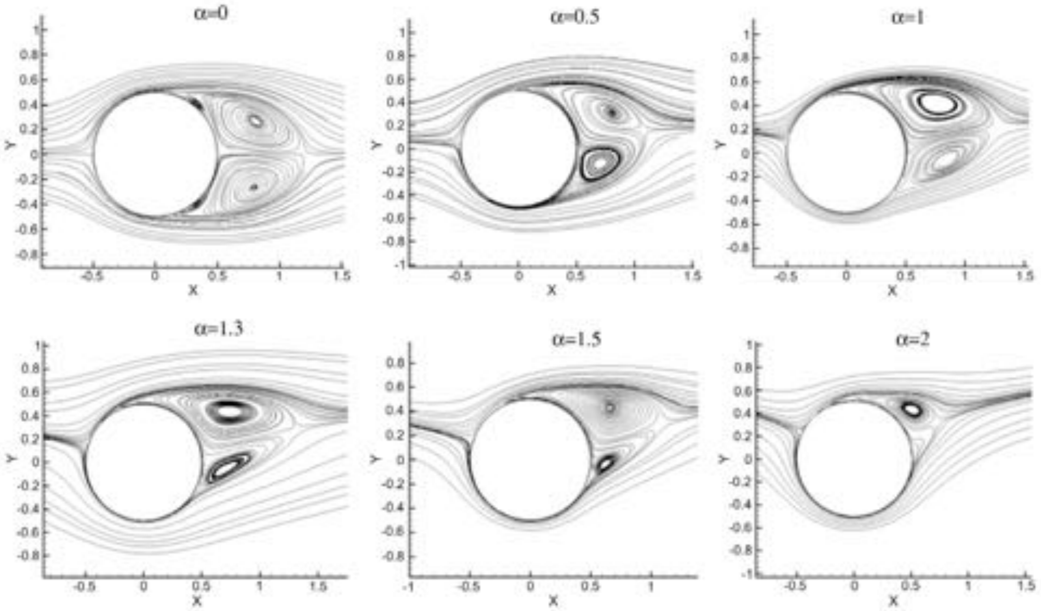

Figure 3.10.: Streamlines for $0 \leq \alpha \leq 2$. Taken from Karabelas [8]

In the study the loads started becoming stable at $\alpha = 1.3$ and after $\alpha = 1.5$ no vortex shedding was found. The mean drag coefficient shows quite good agreement with the experimental results of Aoki and Ito [18]. As such, it is not highlighted here, but it is depicted with the drag coefficients of other numerical studies in Figure 3.18. However, the mean lift coefficient as function of α is shown here in Figure 3.11, since, surprisingly the results rather follow the trend of the laminar solution.

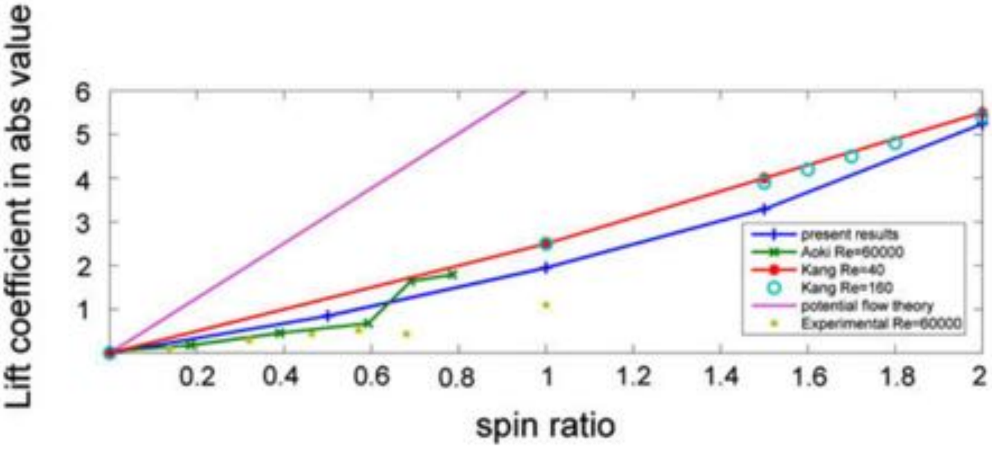

Figure 3.11.: Magnitude of lift coefficients for $0 \leq \alpha \leq 2$. Taken from Karabelas [8]

The inverse Magnus effect was not captured at all. Furthermore, what is even more eye-catching, is the big discrepancy between the experimental result of Aoki and Ito [18] and Karabelas's results at $\alpha = 1$. The difference is around 70 %. Although the Reynolds numbers are not the same in the simulation and in the experiment, according to Figure 3.7 the c_l values do not show significant scatter for different Reynolds numbers as long as these Reynolds numbers lay in the same regime. Moreover, the experiments demonstrate the trend which was also observed by Lam [15]; namely that c_l decreases with Re. Hence, the deviation is even bigger when it is compared with Swanson's results, indicated in Figure 3.7. Conforming to the experimental studies of Swanson [7], Badalamenti and Prince [19] and Aoki and Ito [18] the inverse Magnus effect has surely had to die out until $\alpha = 1$, thus the deviation should emerge due to another reason. Unfortunately, in the paper this big overprediction in the lift was not explained. Furthermore, comparing the mean lift coefficient values of Karabelas with Reid's [17] values in Figure 3.7b we can see that, despite the higher Reynolds number the mean lift coefficients of Karabelas's simulation show again higher values for each $\alpha > 1$. However, it should be noted (see Figure 3.17) that all numerical simulations give similar c_l values to Karabelas's results at $\alpha = 1$, moreover they also reproduce that c_l increases with Re in the transcritical regime. The source of these discrepancies is still not known.

In the study the total resolved kinetic energy (k_f) as well as the kinematic Reynolds-shear stress in the xy plane ($\langle u'v' \rangle$) were also plotted. These results make an important part of the comparison with the current results, thus they are presented here briefly:

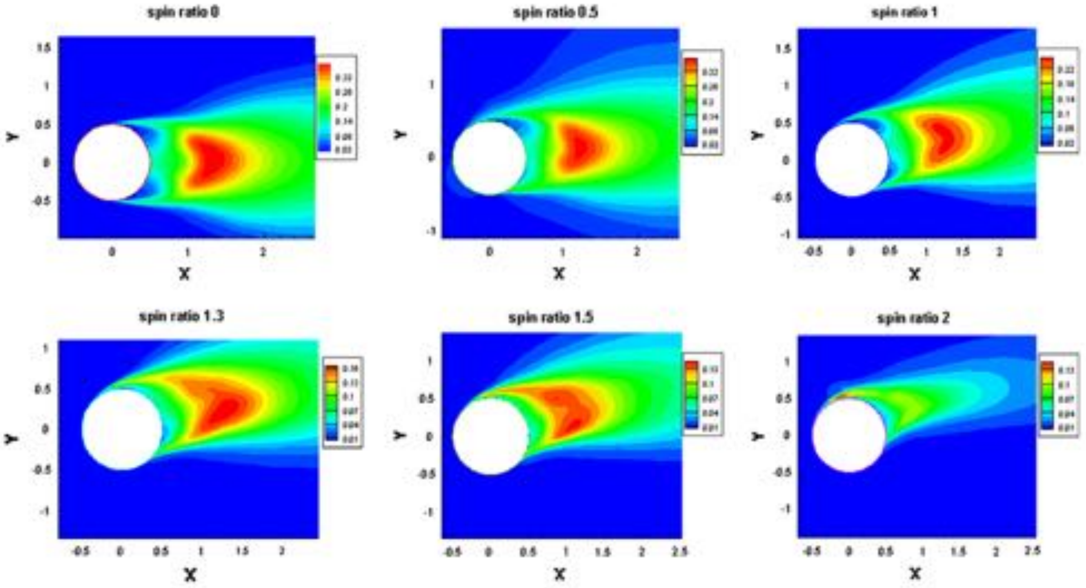

Figure 3.12.: Total resolved kinetic energy (k_f) for $0 \leq \alpha \leq 2$. Taken from Karabelas [8]

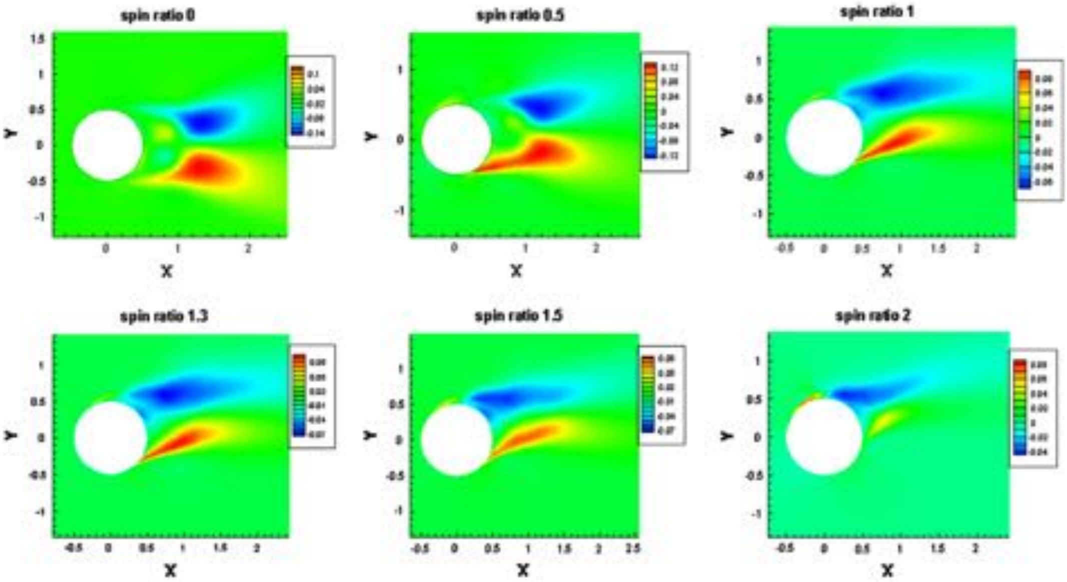

Figure 3.13.: Kinematic Reynolds stress in the xy plane ($\langle u'v' \rangle$). Taken from Karabelas [8]

As a general trend one can see that the magnitudes of k_f and $\langle u'v' \rangle$ decreases with α. This is explained by the stability of this type of flows. The low frequency oscillations are attributed to the vortex shedding, whilst the high frequency variations belong to the turbulent fluctuations. As we have seen before vortex shedding is getting to be suppressed as α increases, however at the same time turbulent fluctuations become more pronounced (this was conformed by the observed higher vorticity values close to the upper surface). Vortex shedding forms a larger part of the fluctuation energy than turbulent motions, this yields the diminution in k_f and $\langle u'v' \rangle$. In the stationary case the transition lies downstream of the separation point. As the rotation starts, the plots show a similar deflection towards the pressure side as was reported for the streamlines. Furthermore, the flow becomes turbulent both at $\theta > 90°$ and close to the point where the free stream deflected from the upper surface. It was also reported that for $\alpha > 1$ the downstream region attached to the cylinder is entirely turbulent. Furthermore, for $\alpha = 2$ it was found that the flow is highly turbulent everywhere close to the surface of the cylinder.

RANS studies of flow around spinning cylinders

Craft with his team in Manchester published several papers [20], [21], [14] and [11] in connection with Flettner-rotors. The group extensively examined the effect of endplates and evenly distributed discs (as suggested by Thom) along the cylinder. The applied computational mesh and calculation methods are the same from article to article, furthermore the most recent paper always contains the results of the previous ones. Therefore, here only the last paper [11] from 2013 will be introduced in detail.

In this work URANS simulations were carried out at $Re = 140\,000$, $Re = 800\,000$ and $Re = 1\,000\,000$. The rotational speed ranged from 0 to 8. The 3 D incompressible URANS equations were discretized on a non-orthogonal multi-block collocated mesh with about 500

000 points (for a cylinder height of 1 D). The mesh was equipped with grid refinement in the near cylinder area and had a C-type form, as can be seen in Figure 3.14:

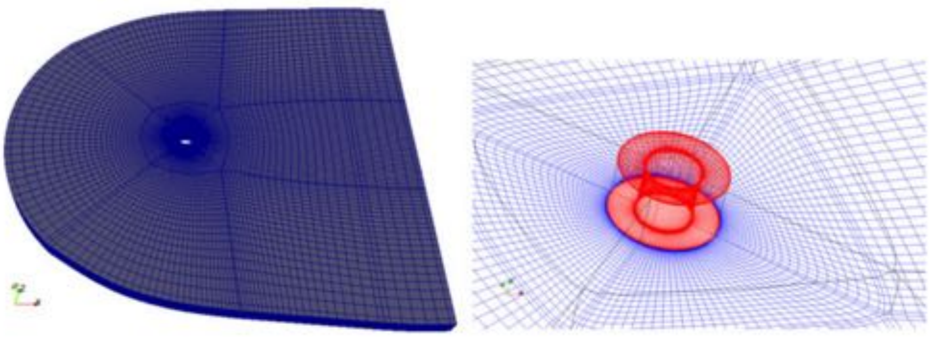

Figure 3.14.: Computational mesh. Note presented results in thesis are from the bare cylinder case. Taken from Craft et al. [11]

The grid extended either 1 or 3 diameters in the axial direction. The inflow boundary was located eleven diameters upstream from the rotor whilst the outlet was placed 16.5 diameters downstream from it. The equations were solved by a customized version of the STREAM code. The convective flux terms were discretized by the UMIST scheme, whereas temporal discretizaton was realised by second-order accurate Crank-Nicolson scheme. With the time-step applied the maximum CFL numbers were reported to be of order of unity. Turbulence was modelled either by the $k-\epsilon$ eddy-viscosity model (with a constraint to limit the near-wall length scale) or by the two-component-limit (TCL) stress-transport closure. The latter was developed by the lead author and it solves transport equations for the kinematic Reynolds stresses $\langle u_i' u_j' \rangle$. At the inlet a uniform inflow boundary condition is imposed, while at the outlet an outflow condition is applied and on the cylinder's surface a no-slip condition is defined. In the boundary layer two types of wall functions were tested: standard wall functions and analytical wall function (AWF). AWF is again developed by Craft, it prescribes the viscosity distribution near the wall and hence it can capture the near-wall skewing of the velocity profile.

The obtained aerodynamic coefficients are shown with other numerical simulations' data in Figure 3.17 and in Figure 3.18. In the results significant differences can be seen between the two and three dimensional results. The Q-criterion plot reveals that indeed real 3 dimensional vortical structures are formed in the wake of the cylinder. Furthermore, mean-flow streamlines show remarkable deviation at higher rotational rates ($\alpha = 5$) for the 2D and 3D cases. These findings are depicted below:

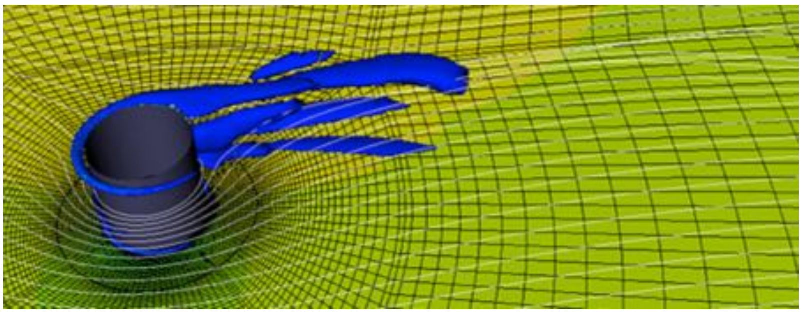

Figure 3.15.: Q-Criterion isosurfaces at $Q = -0.05$. $Re = 800\,000$, $\alpha = 5$. Flow comes from the left, cylinder rotates counterclockwise. Taken from Craft et al. [11]

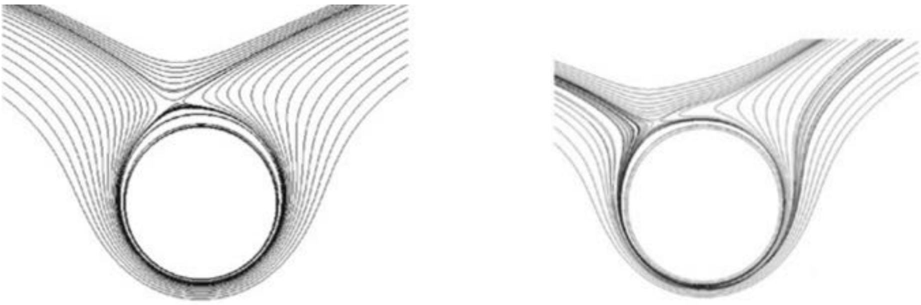

(a) Streamlines for 2 D

(b) Streamlines for 3 D. $AR = 1$

Figure 3.16.: Streamlines at $Re = 140\,000$ and $\alpha = 5$. Flow comes from the left, cylinder rotates counterclockwise. Picture is taken from Craft et al. [11]

Despite the differences in 2D and 3D, once the flow was treated as 3 dimensional the aspect ratio of the cylinder did not have significant impact on the flow (the aerodynamics coefficient were equal until hundredths).

Aerodynamic summary of numerical studies with high Reynolds number

By analogy to the experimental section, in Figure 3.17 and in Figure 3.18 the obtained magnitudes of the aerodynamic coefficients as functions of the rotational ratio are depicted in single figures:

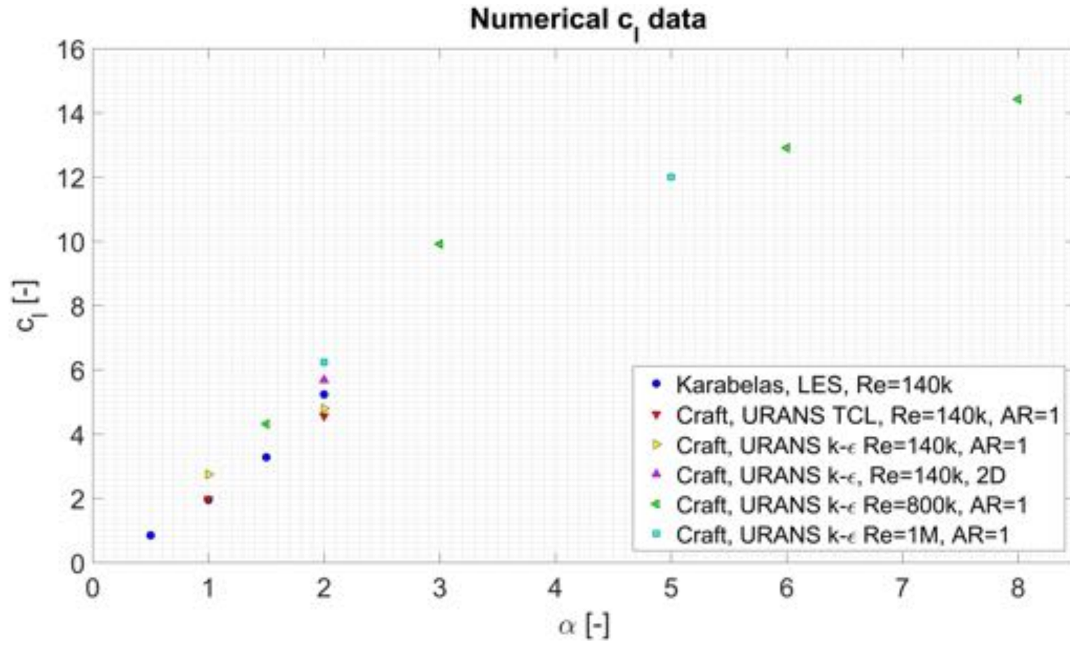

Figure 3.17.: Numerical results for the lift coefficient

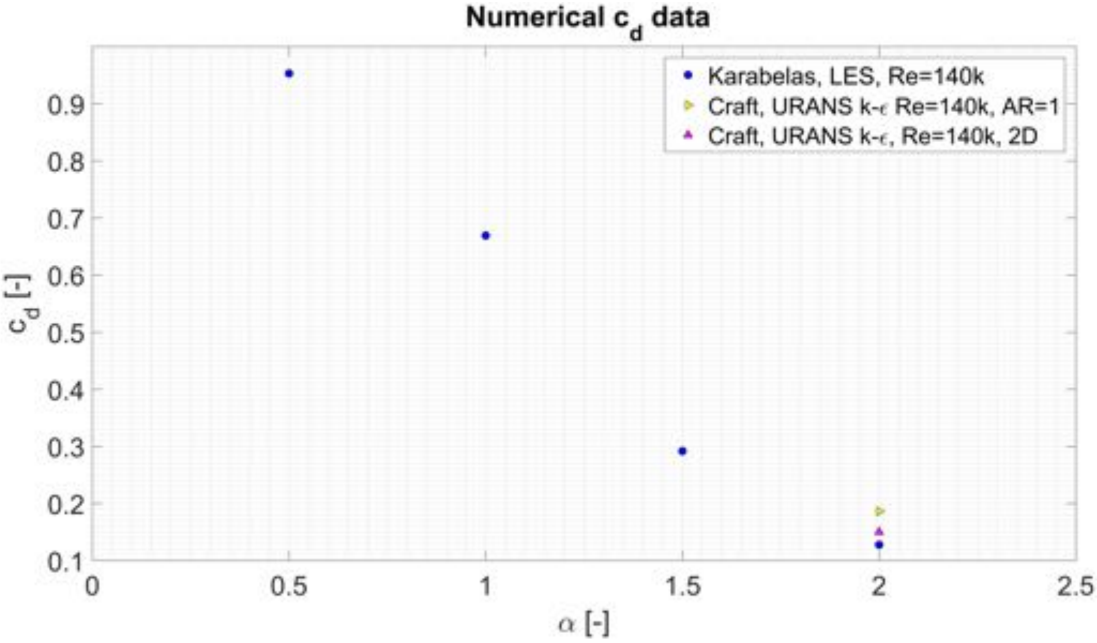

Figure 3.18.: Numerical results for the drag coefficient

4. Numerical models

The cumpotations in the thesis were carried out in FLUENT 15. The computations highly involve turbulence. Those of the readers who are not experienced in the usage of FLUENT or in the field of turbulence, especially in eddy-viscosity, Reynolds stress and Large Eddy Simulation models is very recommended to read the "Turbulence modelling" chapter in Appendix A.

4.1. Computational domain

A direct comparison will be made between our computations and Karabelas's results. Therefore the by far most logical decision was to choose exactly the same O-type computational domain which is depicted in Figure 3.9a. The diameter of the cylinder was chosen to be: $D = 1\,m$. The extension of the domain in the axial direction is either 1 D or 2 D.

4.2. Computational meshes

The grids are again very similar to the one which was used by Karabelas. In the azimuthal direction 126 points are considered (Karabelas used 125). However, in order to keep the growth ratio between cells below 1.05 a more significant modification was made in the distribution of the points. In Figure 3.9b we see a jump in the length of the cells in the azimuthal direction. It is obvious that at the boundaries of the jumps the ratio between the azimuthal length of the cells exceeds 1.05. In the current work with introducing 1 more point and redistributing the points the jumps were smoothed out. In order to obtain the best results in LES simulations, FLUENT suggests to keep the wall unit around 1. To fulfil this recommendation, in LES simulations a finer resolution than Karabelas's resolution was used. The growth rate limit for RANS simulations is 1.3 which allowed us to use coarser grids while keeping wall y^+ values low. The meshes consist of 32 points per 1 diameter length in the axial direction. Examples of an LES and a RANS computational mesh are shown in Figure 4.1, while Table 4.1 sums up the main features of the used computational grids.

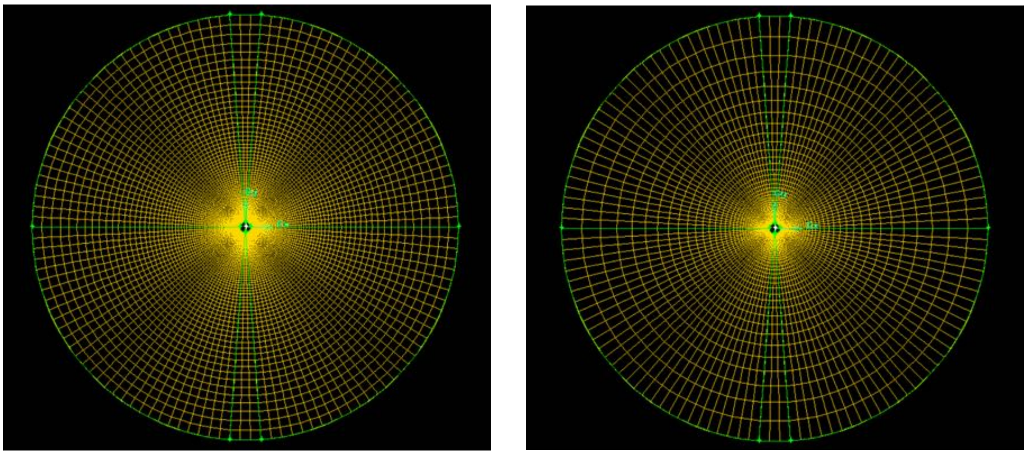
(a) G3

(b) G5

Figure 4.1.: Examples for the computational meshes

Grid	Extension in z	Points in xy	Points along z	total points	Used for
G1	1 Diameter	20 160	32	645 120	LES
G2	1 Diameter	22 932	32	733 824	LES
G3	2 Diameter	22 932	64	1 467 648	LES
G4	1 Diameter	12 600	32	403 200	URANS / RANS
G5	-	20 160	-	20 160	URANS / RANS
G6	1 Diameter	7 560	32	241 920	URANS

Table 4.1.: Computational meshes

4.3. Boundary conditions

As indicated in Figure 3.9a the free stream is coming from the left and the cylinder rotates counterclockwise. At the inlet (I) a uniform horizontal velocity 1 m/s without any perturbation is prescribed. The rationale behind choosing the characteristic length (diameter of the cylinder) together with the characteristic velocity to be unity is that the plots (like k, $\langle u_i' u_j' \rangle$ etc.) and the simulation time will be non-dimensionalised automatically. An outflow boundary condition is applied at the outlet (O), whilst along the side boundaries (S_1 and S_2) a symmetry condition was chosen. The cylinder rotates around the axial axis, on its surface (C) no-slip shear condition is imposed, while the desired α is set by the angular velocity. Periodicity of the flow is assumed in the axial direction. In the 2D cases the boundary conditions are the same, obviously without using the periodicity due to the 2D nature.

4.4. Turbulence models

Several runs were performed with different turbulence models. The previous chapter explained the physics behind these models, thus here only the names of the models with the applied near wall treatment are listed in Table 4.2:

Model	Type	Model	Near wall treatment
M1	LES	Smagorinsky-Lilly	Default FLUENT's treatment (see in App. A)
M2	LES	WALE	Default FLUENT's treatment (see in App. A)
M3	URANS / RANS	Realizable $k - \epsilon$	Enhanced wall treatment
M4	URANS / RANS	SST $k - \omega$	Incorporated in the model
M5	URANS / RANS	Reynolds stress (RSM), stress-ω	Incorporated in the model

Table 4.2.: Used turbulence models

4.5. Discretizational schemes

4.5.1. Pressure coupling and temporal discretization

In each time-step for the velocity pressure coupling the PISO scheme was solved. Besides, the temporal discretization was always FLUENT's second order implicit scheme (see 25.3.2 and 25.5.4 in FLUENT User's Guide [22] for details). The spatial dicretization schemes are depicted in Table 4.3. Detailed description of the spatial discretization schemes can be found in 25.3.1 and 25.3.3 FLUENT User's Guide [22].

Model	Grad.	p	Mom.	k	ϵ	ω	$\langle u'_i u'_j \rangle$
M1	LS	2nd Order	CD	-	-	-	-
M2	LS	2nd Order	CD	-	-	-	-
M3	LS	2nd Order	2nd Order Upwind	2nd Order Upwind	2nd Order Upwind	-	-
M4	LS	2nd Order	2nd Order Upwind	2nd Order Upwind	-	2nd Order Upwind	-
M5	LS	2nd Order	2nd Order Upwind	-	-	2nd Order Upwind	2nd Order Upwind

Table 4.3.: Spatial discretizational schemes. Note: Grad.: Gradient, Mom.: Momentum, CD: Central Differencing, LS: Least Square Cell Based

4.6. Simulation set-up

In the thesis seceral unsteady (LES and URANS) and steady (RANS) simulations were carried out. In the unsteady simulations the time-step was chosen to be: $dt = 0.001$. In general, with the chosen time-steps maximum CFL numbers were falling between 0.2-0.4. For the convergence criteria, both in the steady and unsteady runs all residuals were set to 10^{-4}. Unless the solution converged faster, in the unsteady simulations the number of iterations per time-step was 20.

5. LES Results

The main purpose of this chapter is to introduce the results of the LES computations. In high Reynolds number shear flows a general superiority is expected from LES . In the subsequent chapter a quantitative comparison between the LES and RANS computations is intended to be carried out. Consequently, it is very important to choose from the LES results the simulation which most likely reproduces the real flow field around the cylinder. According to Table 5.1 LES simulations were performed at $Re = 60\,000$ and at $Re = 140\,000$ with $\alpha = 0$ and $\alpha = 2$. The $Re = 60\,000$ $\alpha = 1$ and $Re = 140\,000$ $\alpha = 0$ pairs used for experimental validation while as mentioned earlier $Re = 140\,000$ with $\alpha = 2$ are the main parameters of the simulation. The simulations usually were ran until 100 dimensionless time. All of the simulations were initialised either by unsteady 2 D $SST\, k - \omega$ results or by previous LES results which let the solutions to converge faster. After the initial effects have died out, in FLUENT the data sampling for time statistics command was turned on.

Id.	Model	Grid	α	Re
L1	Smagorinsky (M1)	G1	2	140 000
L2	WALE (M2)	G1	2	140 000
L3	WALE (M2)	G2	2	140 000
L4	WALE (M2)	G3	2	140 000
L5	WALE (M2)	G3	1	60 000
L6	WALE (M2)	G3	0	140 000

Table 5.1.: Different LES runs

5.1. LES results at $\alpha = 2$

The main interest of the thesis is the $\alpha = 2$ case. As a starting point the aerodynamic coefficients will be examined for the different LES runs. Later, the two used subgrid scale models: the Smagorinsky-Lilly and the WALE will be compared. Finally, the effect of grid refinement and domain extension will be examined with the chosen model. The Reynolds number was kept at 140 000 in these runs.

5.1.1. Lift and drag coefficients

Figure 5.1 and 5.2 show the time evolution of the lift and drag coefficient respectively. In Table 5.2 the mean values of the magnitudes of the coefficients together with other works' results are shown. In the calculation of the mean values the initial effects were removed, the averaging started after 10 dimensionless time scales.

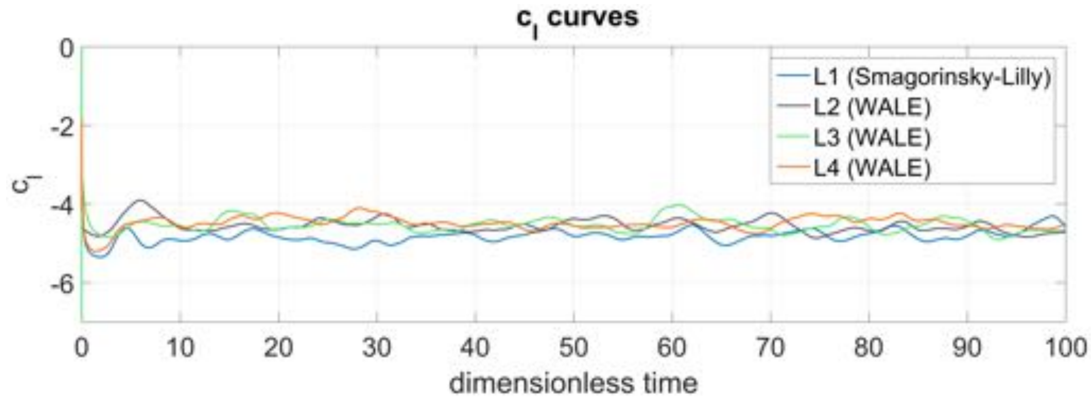

Figure 5.1.: Lift coefficients at $Re = 140\,000$ with $\alpha = 2$

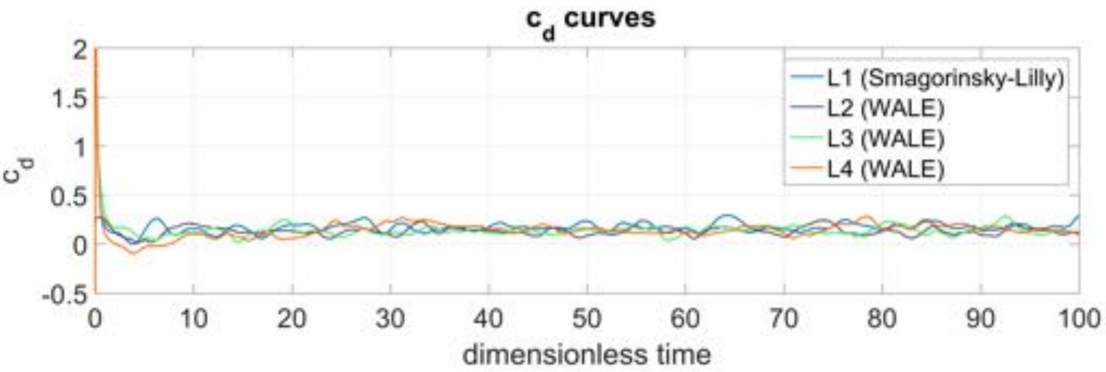

Figure 5.2.: Drag coefficients at $Re = 140\,000$ with $\alpha = 2$

As one can see, the choice of the turbulence model has bigger impact on the aerodynamic forces than the resolution of the grid or the extension of the domain. In general, we can say that the present results are the closest to the only available experimental data. Unfortunately, the Reynolds number in Reid's experiment was much smaller than here, therefore it is more relevant to compare the results with the other numerical data. Surprisingly, the current simulations show better agreement with the RANS results of Craft than with the LES results of Karabelas. L1 with the Samgorinsky model gives identical lift and very similar drag to the results obtained by Craft [11] with the $k - \epsilon$ model. The WALE runs slightly differ from the Smagorinsky and from the $k - \epsilon$ models, however they perfectly match with the results of TCL.

Id.	Model	Re	α	cl_{mean} $[-]$	cd_{mean} $[-]$
L1	Smagorinsky-Lilly	140 000	2	4.8046	0.1743
L2	WALE	140 000	2	4.5708	0.1336
L3	WALE	140 000	2	4.5309	0.1387
L4	WALE	140 000	2	4.4711	0.1514
Karabelas	Smagorinsky-Lilly	140 000	2	~ 5.23	~ 0.13
Craft	$k-\epsilon$	140 000	2	4.8	0.186
Craft	TCL	140 000	2	~ 4.56	N/D
Reid	Exp.	45 000	2	~ 4.06	~ 0.67

Table 5.2.: Mean lift and drag coefficients. Exp.: experimental; N/D: no data

5.1.2. Smagorinsky-Lilly vs WALE model

.

For the comparison of the two subgrid scale models L1 (with the Smagorinsky-Lilly model) and L2 (with the WALE model) were chosen (Table 5.1). In the only available LES reference from Karabelas [8], the subgrid model was modelled by the Smagorinsky-Lilly model. As a reference, here Karabelas's results with $\alpha = 2$ will be indicated again. Figure 5.3 shows the streamlines based on the time and space averaged (averaged in the z direction) resolved velocities.

The general trends are the same on all graphs. The free stream on the pressure side slides over a counter rotating layer and deflects horizontally, while on the suction side the flow is dragged with the surface of the cylinder and the streamlines mimic the inviscid case. However, in the wake one can see significant differences. Probably the most eye-caching one is the number of vortices. Karabelas's result shows that the lower vortex collapses at $\alpha = 2$ while in the current simulation there is no indication about collapse and clearly two vortices are formed behind the cylinder. An exact explanation cannot be given to this phenomenon, although some guesses exist for the discrepancies. Albeit, G1 and Karabelas's mesh have the same dimensions, G1 consists of about 15 % more grid points, thus the wake area is surely better resolved. Furthermore, the jumps in the length of the grid cells in the azimuthal direction are removed, hence the growth ratio between cells is kept below 1.05. Besides, in FLUENT for discretizing the momentum equations two central differencing schemes exist, the "Central Differencing" and the "Bounded Central Differencing" and from Karabelas's description it is not evident that which one he took. Finally, neither the convergence criteria nor the maximum number of iteration steps were mentioned in the paper.

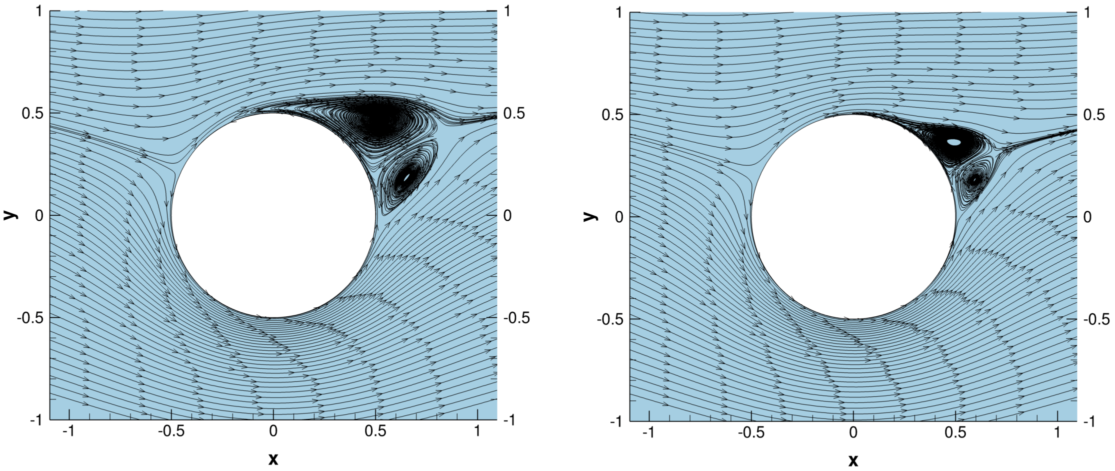

(a) Streamlines with
the Smag.-Lilly model (M1)

(b) Streamlines with the
WALE model (M2)

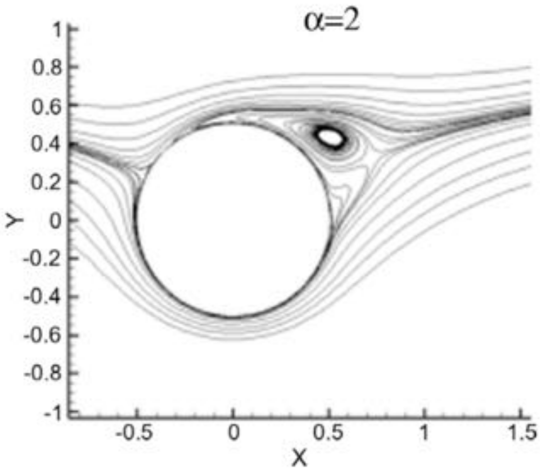

(c) Streamlines from Karabelas [8]
with the Smag.-Lilly model

Figure 5.3.: Streamlines around the cylinder at $Re = 140\,000$ with $\alpha = 2$. Last picture is taken from Karabelas [8]

After a closer look, we find deviations between the Smagorinsky-Lilly (M1) and the WALE (M2) results as well. In case of the Smagorinsky-Lilly model the vortices are noticeably larger. The vortex formation ends at 1D behind the cylinder while for the WALE model recirculation are not be visible for $x > 0.75\,D$. In addition vortices possess a larger extension in the vertical direction too. In case of the Smagorinsky-Lilly model the upper vortex penetrates more into the free stream hence causing a larger deflection of the wake.

The behaviour of the flow is different for the two models near the upper separation point too. As was explained in the Chapter of Basic flow physics the separation does not happen on the surface. Consequently, the well-known process of capturing the separation point by the point where the friction force disappears is not applicable for this type of flow. Instead, the separation point was detected with the help of the radial velocity component, more precisely by determining the point where the radial velocity first becomes positive from negative:

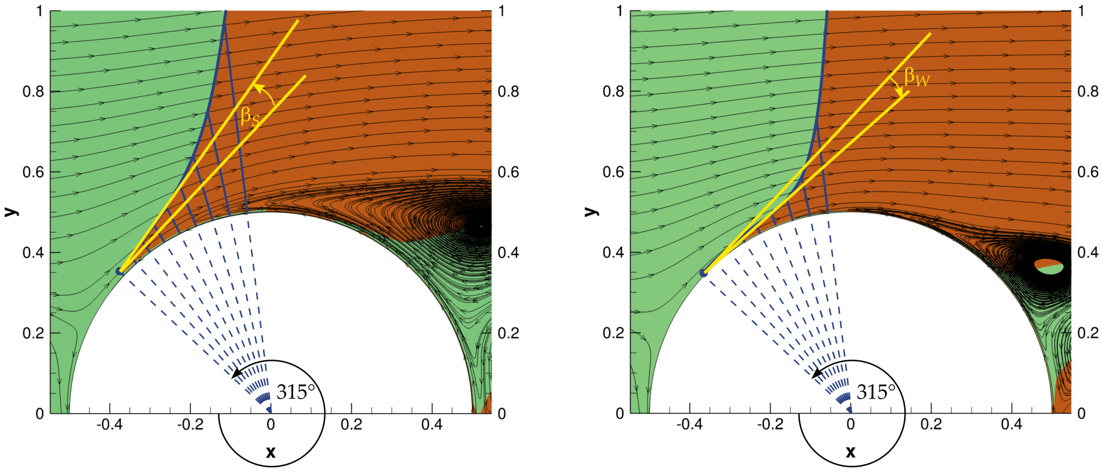

(a) Radial velocities with Smag.-Lilly model (M1)

(b) Radial velocities with WALE model (M2)

Figure 5.4.: Positive and negative radial velocity areas around the upper half of the cylinder at $Re = 140\,000$ with $\alpha = 2$. Green: negative velocity, orange: positive velocity, blue: borderline

According to the plots in both cases separation of the free stream on the pressure side (marked with a blue dot) starts at $\theta_{sep} \approx 315°$. In the figures with blue colour the borderline between the negative and positive velocities is highlighted. One can see that in case of WALE simulation the borderline stays closer to the surface of the cylinder over a larger distance. Or in other words with the WALE model as we are moving further and downstream from the surface of the cylinder, the radial velocity component swaps sign from negative to positive in a slower pace. Oppositely for the Smagorinsky-Lilly model we see that, the free stream gains positive radial velocities faster, so separation happens under a larger angle. Conforming to the notation of Figure 5.4 this means $\beta_W < \beta_S$. The slower separation pace associated with a longer suction area on the pressure side. As a result, the lift diminishes for the WALE model (M2), which is consistent with Table 5.2. Figure 5.5shows the time and space averaged cp values on the cylinder's surface.

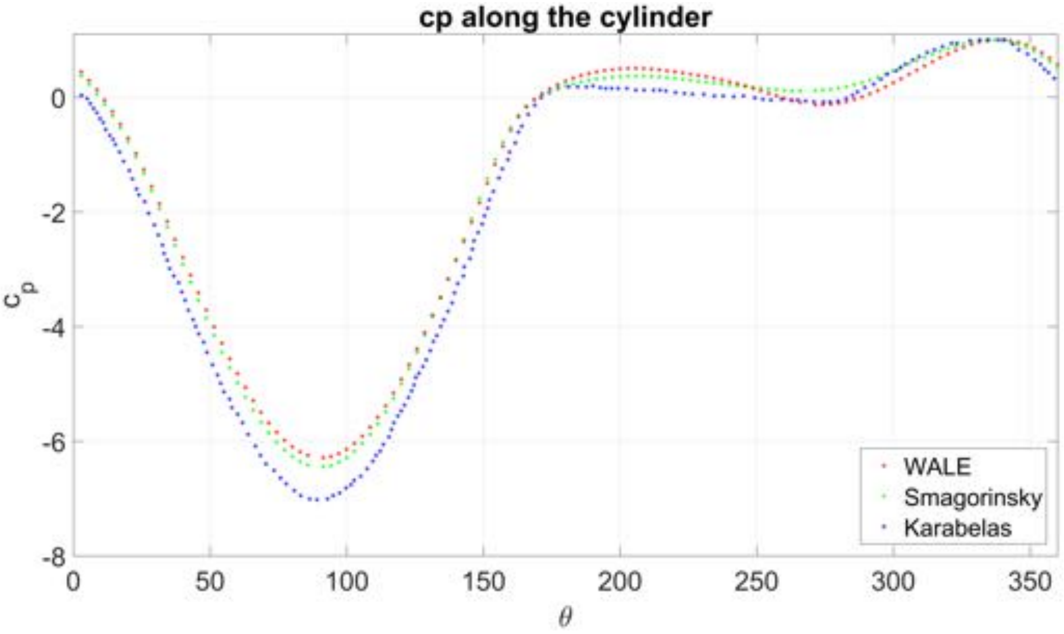

Figure 5.5.: Mean peressure coefficients along the cylinder. Blue data set is taken from Karabelas [8]

In conjungtion with the above mentiond considerations, we see higher cp values between the stagnation point ($\theta_{stag} \approx 335°$and it is further from the cylinder!) and $\theta = 250°$. Comparing the cp curve of the WALE model with the one obtained by Karabelas, we can see that Karableas's simulation likewise was failed to capture the pressure reduction on the top of the cylinder. His results shows similar trend to our Smagorinsky-Lilly simulation, the extrema of the curve are on the same location as well. Nevertheless, his minimum value is significantly smaller. To have a better understanding about the differences between the Smagorinsky-Lilly and the WALE model in Figure 5.6 and in Figure 5.7 the turbulent kinetic energy as well as the kinematic Reynolds stresses of the resolved field in the xy plane were plotted. Again these plots are space and time averaged results.

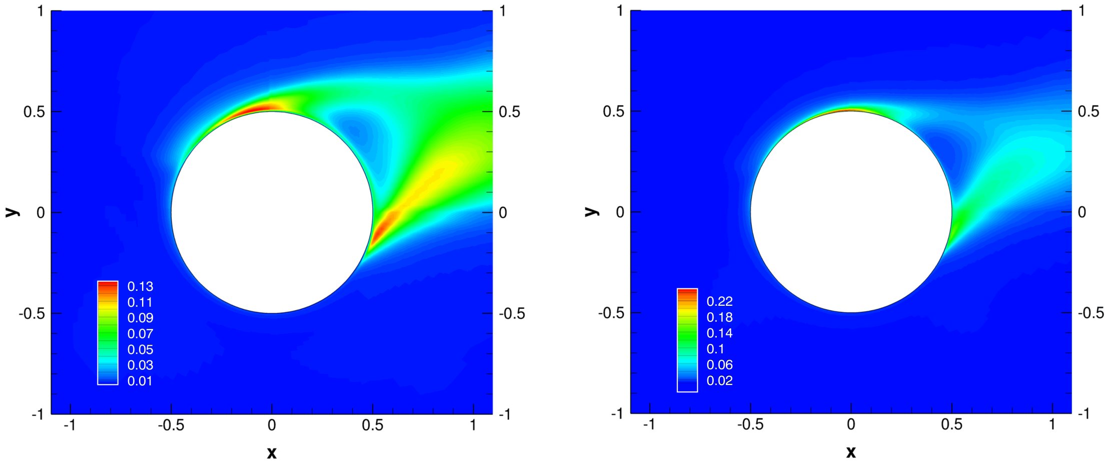

(a) k_r with the Smag.-Lilly model (M1)

(b) k_r with the WALE model (M2)

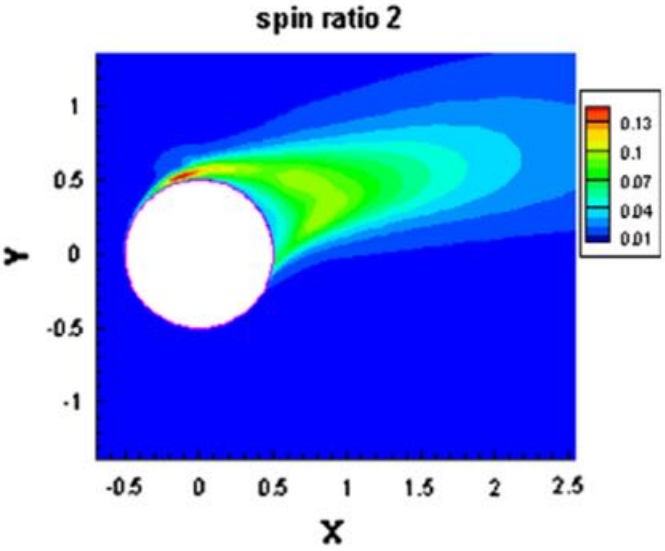

(c) k_r from Karabelas [8]
with Smag.-Lilly model

Figure 5.6.: Resolved turbulent kinetic energy (k_r) at $Re = 140\,000$ with $\alpha = 2$. Last picture is taken from Karabelas [8]

The Smagorinsky-Lilly run shows quantitatively very similar values to Karabelas's results. However, as is clearly seen, significantly larger values are obtained in the vicinity of the lower separation point. In order to explain this discrepancy first we make the assumption that the residual motions have negligible contribution to the turbulent kinetic energy so that the whole turbulence is resolved ($k = k_r$). Hence, the variation of k_r can be calculated by Equation (A.30). Applying the consideration that the resolved flow is statistically homogeneous in the z direction and based on Equation (A.31) one can write for the production term of k:

$$P_k = -\rho \left\langle (\overline{u} - \langle \overline{u} \rangle)(\overline{v} - \langle \overline{v} \rangle) \right\rangle \left\langle \frac{\partial \overline{u}}{\partial y} + \frac{\partial \overline{v}}{\partial x} \right\rangle = -\rho \langle u'v' \rangle \left\langle \frac{\partial \overline{u}}{\partial y} + \frac{\partial \overline{v}}{\partial x} \right\rangle \tag{5.1}$$

In Figure 5.7c and in Figure 5.7a one can see that the resolved kinematic Reynolds stresses have a positive sign and are approximately same for the two simulation in the inspected region. As such, the difference should come from the spatial variations of the resolved velocities. According to the streamlines and in accordance with $\langle u'v' \rangle > 0$ in the investigated area: $(\partial \langle \overline{u} \rangle / \partial y) < 0$, $(\partial \langle \overline{v} \rangle / \partial x) > 0$ and $|(\partial \langle \overline{u} \rangle / \partial y)| > |(\partial \langle \overline{v} \rangle / \partial x)|$. In case of our Smagorinsky-Lilly run a vortex occurs in this region, which yields that the variation of the horizontal velocity component in the vertical direction is more pronounced, so the difference emerges from the presence of the lower vortex formation.

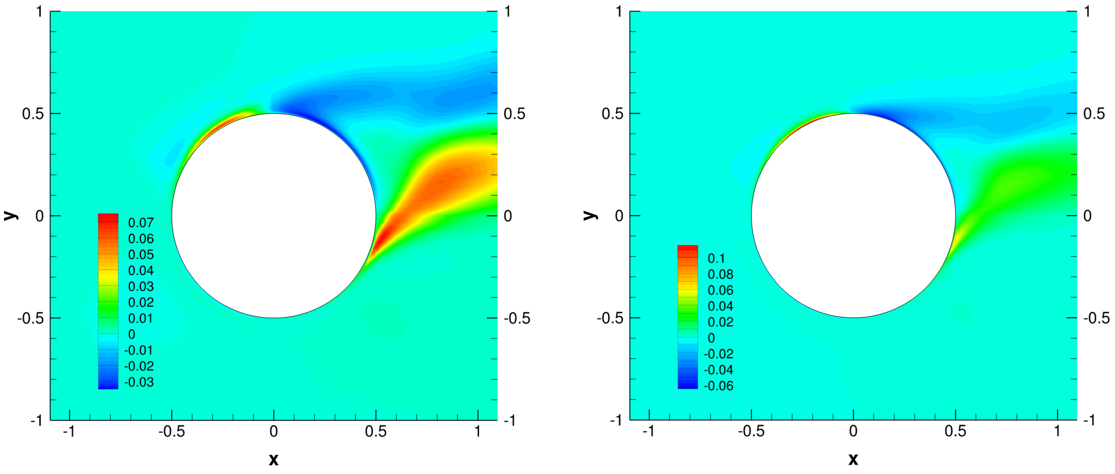

(a) $< u'v' >$ with the Smag.-Lilly model (M1)

(b) $< u'v' >$ with the WALE model (M2)

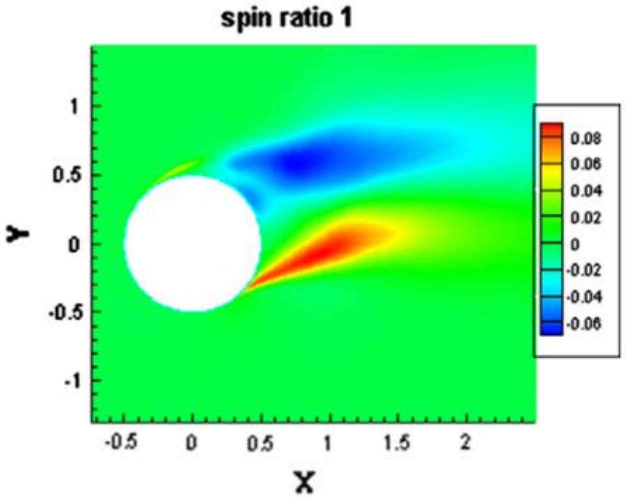

(c) $< u'v' >$ from Karabelas [8]
with Smag.-Lilly model

Figure 5.7.: Kinematic Reynolds stresses at $Re = 140\,000$ with $\alpha = 2$. Last picture is taken from Karabelas [8]

Comparing the results of the Smagorinsky-Lilly (L1) and WALE runs (L2) one can see that the maximum value of k_r is almost twice for the WALE run than for Smagorinsky-Lilly run. Although not that pronounced, but a difference in the magnitude of $< u'v' >$ in favour of the WALE run is present as well. Furthermore, after having a closer look at the region close to the top of the cylinder in Figure 5.8, it is clearly seen that in case of Smagorinsky-Lilly run the high regions of k_r pop up at a larger distance from the wall:

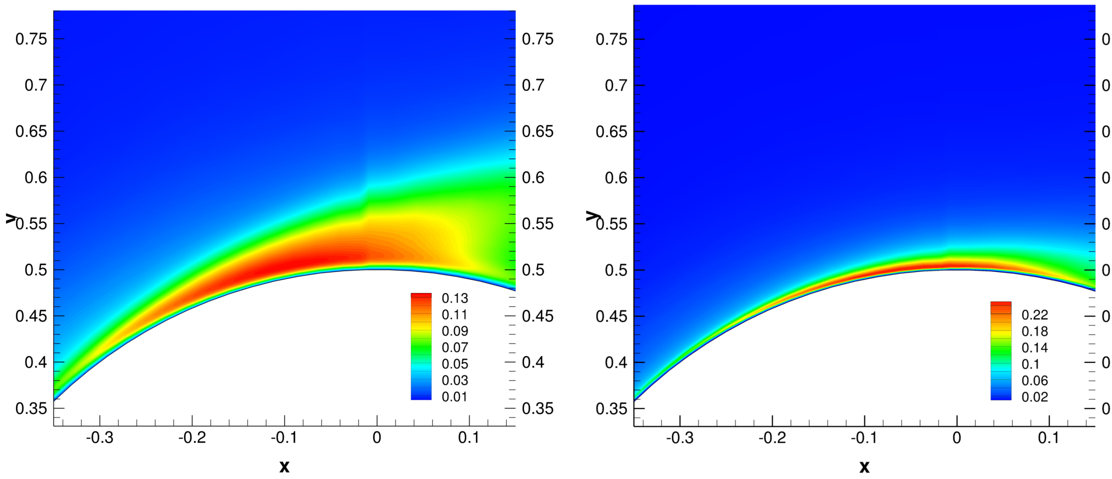

(a) k_r with the Smag.-Lilly model (M1)

(b) k_r with the WALE model (M1)

Figure 5.8.: A closer view on the resolved turbulent kinetic energy (k_r) on the top side of the cylinders. In the simulation: $Re = 140\,000$ and $\alpha = 2$.

This is consistent with the wider vortex formation after the separation point. So far we have seen that the size of the vortices has a huge impact on the flow, so here an explanation is given for the different vortex formations. First, we recall the rotating boundary layer (RBL) from Chapter 2, which was the fluid layer bonded to the cylinder. We have also seen that apart from the RBL (inner portion), the total boundary layer consists of an outer portion, which comes from the free stream that (depending on the location) slides with or over the RBL. In between the two portion a shear layer or a recirculation region is present. Here we focus our attention on the region between the stagnation and upper separation points, where only one strong shear layer separates the two countermoving portions. As was mentioned, in the original Smagorinsky-Lilly model the subgrid mixing lengthscale (Smagorinsky lengthscale, l_S) solely depends on the volume of the grid cell and on the Smagorinsky coefficient, which is constant everywhere and hence the different regions in the flow cannot be distinguished. However, one can see in Appendix A. (Equation (A.89)) that FLUENT uses a modified model which limits the Smagorinsky lenghtscale in the wall region. This limit sets the maximum of the Smagorinsky lenghtscale to be $l_S = \kappa d$ (where: κ is the Von Kármán constant and d is the distance to the wall) in case of grids which are not enough fine to resolve the large eddies in the near wall area. In the RANS discussion of Appendix A. this κd (Prandtl-mixing lenght hypothesis) was found to be the mixing length of the large eddies in the log layer. Furthermore, in the LES section of Appendix A. we called the above described approach LES with near wall modelling (LES-NWM).

The use of either the lenghtscale of the log-layer or the original Smagorinsky lenghtscale throughout the whole boundary layer implies that in FLUENT's Smagorinsky-Lilly model,the lenghtscale in the wake region and in the viscous wall region is overpredicted. The latter fact is because neither the original Smagorinsky lenghtscale nor the Prandtl's mixing length hypothesis can account for that in the near wall area $-u'v' \sim y^3$ and consequently $\nu_r \sim y^3$ (since $\langle u \rangle \sim y$ in the viscous wall region; see the whole deduction in Pope [23] p. 283 and p. 634). Unlike the Smagorinsky model, the WALE model [1] damps the turbulent viscosity correctly in the near wall region and hence ν_r is scaled as $\nu_r \sim y^3$. Indeed, careful inspection of ν_r (not plotted here for brevity) reveals that the subgrid turbulent viscosity ratio (ν_r/ν) in the RBL is 3 orders of magnitude higher for the Smagorinsky-Lilly model than for the WALE model ($\nu_r^{M1}/\nu = 8$ and $\nu_r^{M2}/\nu = 0.007$ respectively). The undamped turbulent viscosity causes a highly turbulent RBL for M1, while in the WALE model turbulence first generated by the separating shear layer so that the RBL is laminar everywhere around the cylinder. The turbulent RBL is significantly thicker than the laminar one, thus it is more capable of deflecting the free stream. Hence the inclination effect is stronger with the Smagorinsky-Lilly model even before the separation point. The greater deflection lets the evolving vortex to grow bigger and also explains why the radial velocity component swaps sign in faster pace for the Smagorinsky-Lilly model. Finally, let us plot the tangential velocities in the vicinity of the upper half of the cylinder. The colours clearly reveals the big deviation in the thickness of RBLs.

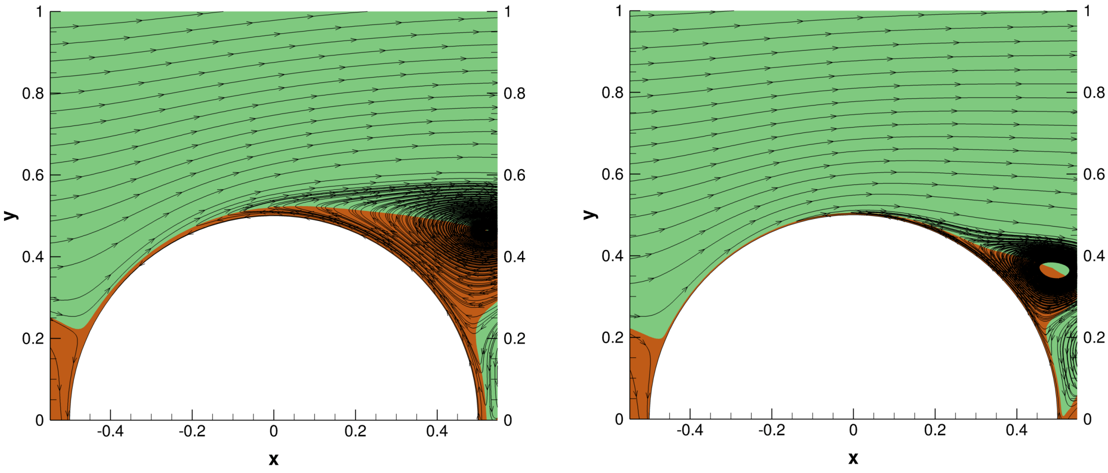

(a) Tang. velocities with Smag.-Lilly model (M1)

(b) Tang. velocities with WALE model (M2)

Figure 5.9.: Positive and negative tangential velocity areas around the upper half of the cylinder at $Re = 140\,000$ with $\alpha = 2$. Green: negative velocity, orange: positive velocity

In conclusion, we can say that the different results of the Smagorinky-Lilly model and the WALE model come from the fact that FLUENT's Smagorinsky-Lilly model cannot distinguish the different regions in the boundary layer. As we have seen, the Smagorinsky-Lilly model produces too much viscosity in the near wall area and thereby causes the RBL to become turbulent and hence to be thicker. Oppositely, the WALE model appropriately damps ν_r close to the wall, thus transition first occurs in the separating shear layer. Therefore, the WALE model mimics the involved physics better in the boundary layer and consequently, this model was chosen for further simulations.

---

[1] It is noteworthy to mention that the WALE model accounts for the near wall area by modifying the subgrid mixing velocity scale. Hence it ensures that both for the near wall modelling (LES-NWM) and near wall resolution model (LES-NWR) in the near wall area $\nu_r \sim y^3$. See deatails in 12.9.3 FLUENT User's Guide [22]

5.1.3. Effect of grid refinement and domain extension

As we have already seen in Table 5.2, the grid refinement and the domain extension had only minimal effect on the aerodynamic forces. However, a general goal was to find the "best" LES result for the RANS comparison. Due to the refinement the maximum y^+ values reduced from 3 to 1.2. In the following figures the streamlines, k_r and $< u'v' >$ plots are shown for M3 and M4 respectively.

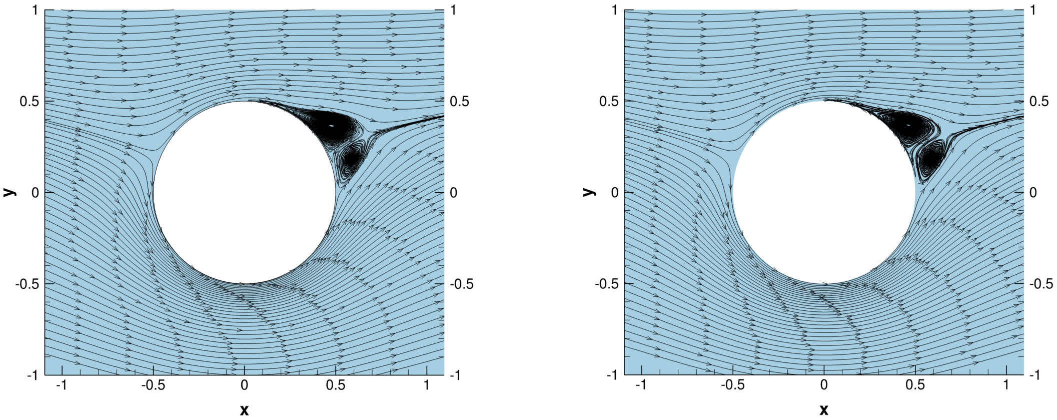

(a) Streamlines with L3

(b) Streamlines with L4

Figure 5.10.: Streamlines around the cylinder at $Re = 140\,000$ with $\alpha = 2$.

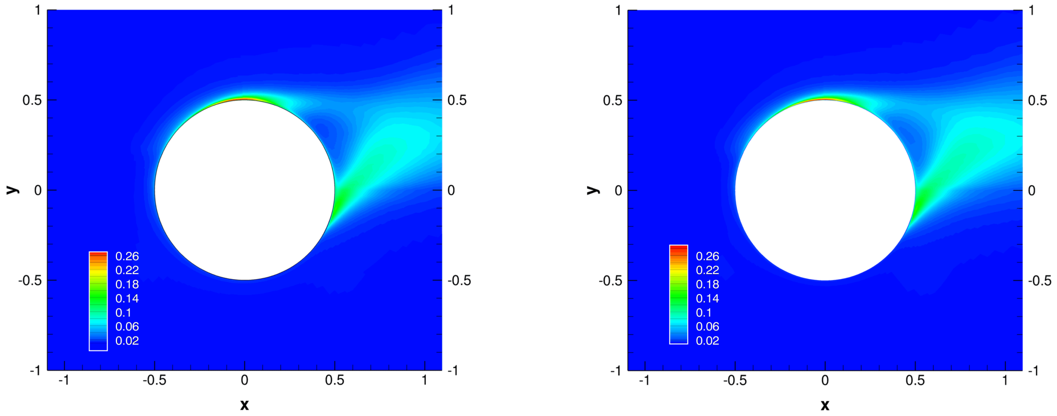

(a) k_r with L3

(b) k_r with L4

Figure 5.11.: Resolved turbulent kinetic energy (k_r) at $Re = 140\,000$ with $\alpha = 2$.

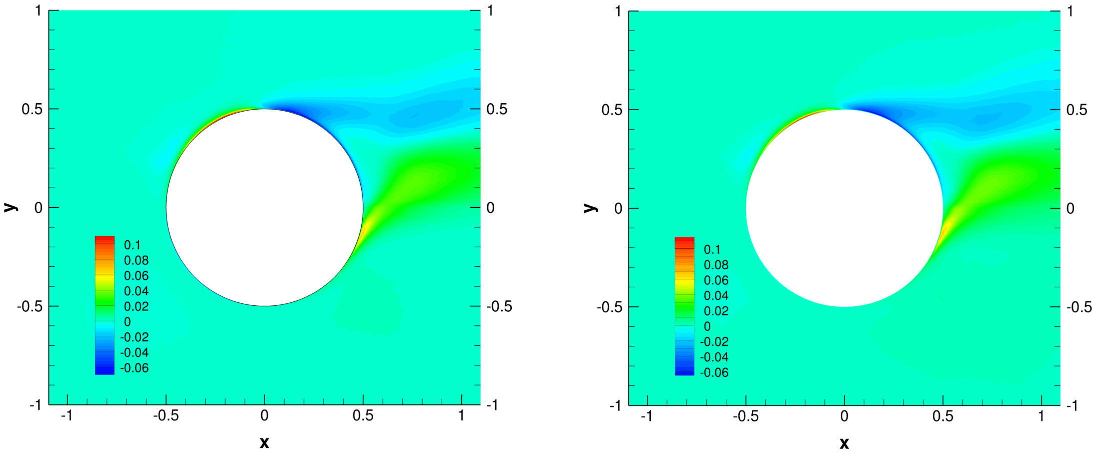

(a) $< u'v' >$ with L3

(b) $< u'v' >$ with L4

Figure 5.12.: Kinematic Reynolds stresses at $Re = 140\,000$ with $\alpha = 2$.

The additional grid points mainly were put in the near wall area, so the flow is surely better resolved there, thus a general superiority in favour of the two refined LES WALE run (L3 and L4) is approved. However, the choice between the two domain sizes is not that straightforward. Moreover, as we see there is almost no difference between the results of L2, L3 and L4. The streamlines give back very similar shapes and RBL is laminar for each simulation. From the radial velocities (not plotted here for brevity) we get $\theta_{sep}^{L3} \approx 316.25°$ and $\theta_{sep}^{L4} \approx 316.9°$. Very small quantitavely differences between L3 and L4 are present in the k_r and $< u'v' >$ plots, but again based on these differences it is impossible to make a decision. In LES simulations it is always desirable to have as little as possible turbulence in the subgrid model. As such, in the evaluation of the L3 and L4 we will rely on the subgrid viscosity ratio values. Subsequently, we will use the wake of the cylinder for comparison, so the values were examined in this area:

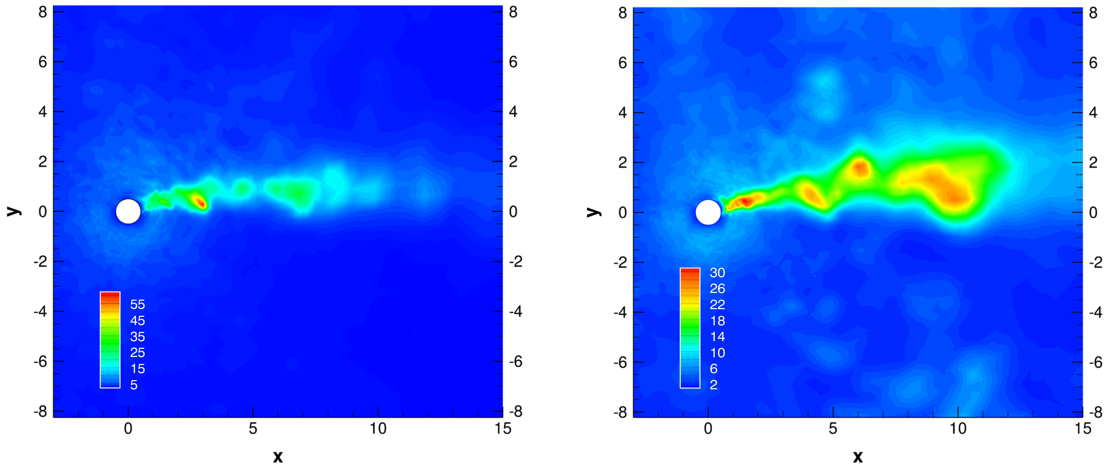

(a) ν_r/ν with L3

(b) ν_r/ν with L4

Figure 5.13.: Subgrid viscosity ratios at $Re = 140\,000$ with $\alpha = 2$.

In Figure 5.13 one can see that in the wake of the run with double extension in the z direction (L4) less turbulence is modelled, therefore this model was chosen for further comparison.

5.1.4. Experimental validation

In order to verify the choosen WALE run with experimental data two WALE runs were performed at $Re = 140\,000$ with $\alpha = 0$ and at $Re = 60\,000$ with $\alpha = 1$. Both simulations were ran on G2 with $dt = 0.001$ dimensionless time-step until 100 dimensionless time. The results are summed up below:

Id.	Model	Dimension	Re	α	cl_{mean} $[-]$	cd_{mean} $[-]$
L4	WALE	3D	140 000	0	0	1
Breuer [24]	Smag.	3D	140 000	0	0	0.97
Breuer [24] (finer mesh)	Smag.	3D	140 000	0	0	1.05
L5	WALE	3D	60 000	1	1.27	0.5
Aoki and Ito [18]	exp.	3D	60 000	1	1.16	0.58

Table 5.3.: Mean lift and drag coefficients.

According to Table 5.3, the stationary run shows outstanding agreement with the numerical results, while magnitude of the lift in the rotating case is also falls within 10% of the results of Aoki and Ito [18]

6. RANS results

In this chapter the RANS results will be summed up and compared with the reference LES run (L4). Altogether 3 different types of RANS models were used: the $k-\epsilon$, the SST $k-\omega$ and the RSM, stress-ω. The basic idea was to perform a steady (since it is proven that there is no vortex shedding at $\alpha = 2$) and an unsteady run in 2D as well as in 3D with each model. In case of the 2D steady RSM run, the domain was too small, reversed flow at the outflow boundary was detected, so that the flow could not be fully developed and the simulation finally crashed. As a consequence, in the table below only 11 runs are indicated:

Id.	Model	Grid	α	Re	Dim.	Type
R1	$k-\epsilon$ (M3)	G4	2	140 000	3D	Unsteady
R2	$k-\epsilon$ (M3)	G4	2	140 000	3D	Steady
R3	$k-\epsilon$ (M3)	G5	2	140 000	2D	Unsteady
R4	$k-\epsilon$ (M3)	G5	2	140 000	2D	Steady
R5	$k-\omega$ (M4)	G4	2	140 000	3D	Unsteady
R6	$k-\omega$ (M4)	G4	2	140 000	3D	Steady
R7	$k-\omega$ (M4)	G5	2	140 000	2D	Unsteady
R8	$k-\omega$ (M4)	G5	2	140 000	2D	Steady
R9	RSM (M5)	G4	2	140 000	3D	Unsteady
R10	RSM (M5)	G4	2	140 000	3D	Steady
R11	RSM (M5)	G5	2	140 000	2D	Unsteady

Table 6.1.: Different RANS runs

In Table 6.1 one can see that 2 types of grid are used in the RANS runs. The grids are not only different in their 2 or 3 dimensional nature, but according to Table 4.1 also in the number of points in the xy plane. The by far smaller involved computational costs allowed us to use a finer mesh (which has the LES grid resolution in the xy plane) for the 2D cases. Although the different resolution gives distorted picture about the differences between the 2D and 3D cases, our final goal is to compare each RANS run with the reference LES run and hence finer resolution is more desirable. The convergence criteria in case of unsteady runs remained the same as in the LES case i.e. residuals smaller than 10^{-4} or maximum 20 iteration steps per time step.

The residuals were set to 10^{-4} in the steady runs as well. It is important to mention that with the 3D steady cases this convergence criterion could not be fulfilled either with the $k-\epsilon$ (R2) or with the RSM (R10) models. Although the relaxation factors were significantly decreased and for the pressure-velocity coupling many models were tested after a certain limit further diminution in the residuals could not be reached. The residual of the continuity equation got stuck at around $2 \cdot 10^{-4}$ in case of the $k-\epsilon$ run. In Figure 6.1a we do not see any variation in the drag coefficient, which suggests that the eddy-viscosity models are capable of handling the problem as steady. Consequently, it is very likely that the convergence criterion might be achieved with the $k-\epsilon$ on a different domain or grid. Nevertheless, as we will see later the general performance of the $k-\epsilon$ is the poorest, thus additional 3D steady $k-\epsilon$ runs were not done. Unlike the $k-\epsilon$, the steady RSM model "wants to become" unsteady and reasonable fluctuations can be seen in the drag coefficient (Figure 6.1b). The residuals of the continuity and kinematic Reynolds stress equations could not go below 10^{-3}. Furthermore, we should mention that the discretization scheme for the Reynolds stresses and for the specific turbulence dissipation rate were only first order accurate. Therefore, the results with R10 can be only examined with some suspicion.

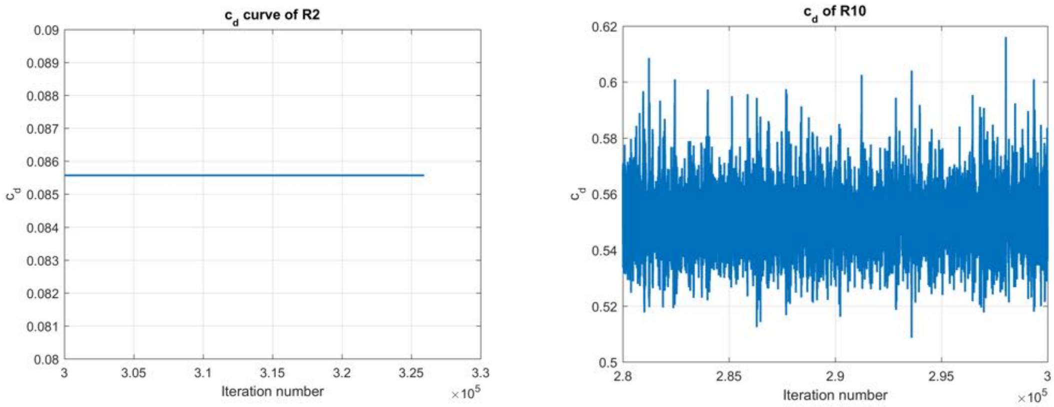

(a) 3D steady run with $k-\epsilon$

(b) 3D steady run with RSM

Figure 6.1.: Examples for drag coefficient variations

6.1. Lift and drag coefficients

As a first step of the comparison in Table 6.2 we look at the magnitudes of lift and drag coefficients of each model.

Id.	Model	Type	Dim.	cl_{mean} $[-]$	cd_{mean} $[-]$
R1	$k-\epsilon$	Unsteady	3D	6.1073	0.0896
R2	$k-\epsilon$	Steady	3D	6.0969	0.0856
R3	$k-\epsilon$	Unsteady.	2D	6.0914	0.0799
R4	$k-\epsilon$	Steady	2D	5.9960	0.0893
R5	$k-\omega$	Unsteady	3D	5.4284	0.1025
R6	$k-\omega$	Steady	3D	5.3601	0.0947
R7	$k-\omega$	Unsteady	2D	5.3680	0.1012
R8	$k-\omega$	Steady	2D	5.3728	0.0913
R9	RSM	Unsteady.	3D	5.0431	0.1471
R10	RSM	Steady	3D	4.7308	0.5480
R11	RSM	Unsteady	2D	6.1073	0.0896
L4	WALE	Unsteady	3D	4.4711	0.1514

Table 6.2.: Mean lift and drag coefficients.

Looking at the results of the $k-\epsilon$ and the $k\omega$ models in Table 6.2, probably the most eye-catching finding is the small differences between the 2 and 3 dimensional cases. Similarly, with the eddy viscosity models, the steady or unsteady nature has only a minor effect on the results. To investigate the 3 dimensional structures in the 3D unsteady runs we used the Q-criterion. By definition the Q values are:

$$Q = \frac{1}{2}\Bigg(\Omega_{ij}\Omega_{ij} - S_{ij}S_{ij}\Bigg) \tag{6.1}$$

in which:

$$S_{ij} = \frac{1}{2}\left(\frac{\partial u_i}{\partial x_j} + \frac{\partial u_j}{\partial x_i}\right) \tag{6.2}$$

is the rate of strain and

$$\Omega_{ij} = \frac{1}{2}\left(\frac{\partial u_i}{\partial x_j} - \frac{\partial u_j}{\partial x_i}\right) \tag{6.3}$$

is the rotation tensor.

By plotting isosurfaces of constant Q values, the 3D structures can be visualized better than by a vorticity plot where the high vorticity values in the boundary layer would gives us a distorted picture. Figure 6.2 [1] shows isosurfaces of Q-criterion for the unsteady 3 dimensional cases:

---

[1] These Q-criterion plots are based on the instantaneous mean velocity field

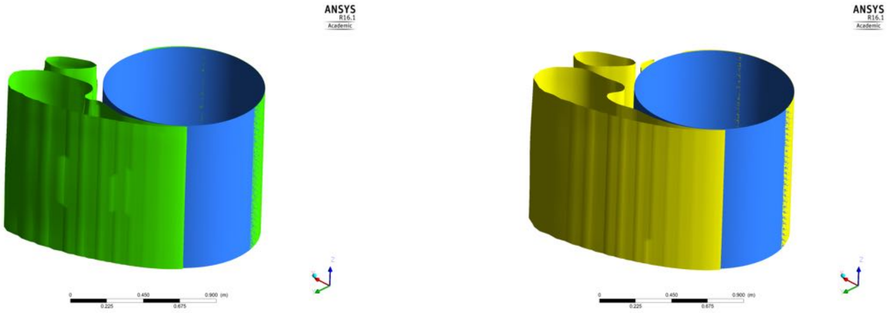

(a) 3 D unsteady $k - \epsilon$, $Q = 0.05\,s^{-2}$ (b) 3 D unsteady $k - \omega$, $Q = 0.1\,s^{-2}$

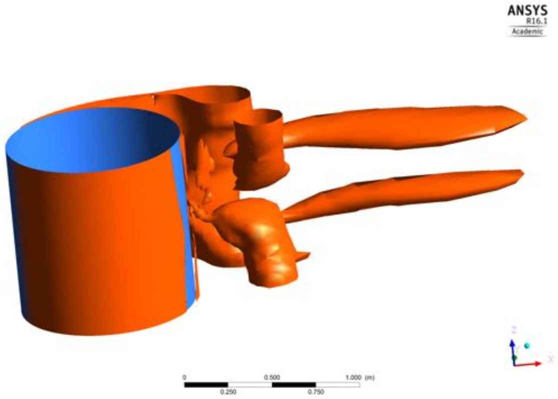

(c) 3 D unsteady RSM, $Q = 1\,s^{-2}$

Figure 6.2.: Q-Criterion isosurfaces

After very careful inspection one can see creases in the Q-criterion plots for the eddy-viscosity models. However, it is fair to say that 3 dimensional structures, in a sense that they are not extruded 2 dimensional structures only can be seen for the RSM run. From the two eddy-viscosity models, the $k-\omega$ shows closer values in terms of drag as well as lift coefficient to the reference LES results. Unambigiously, the unsteady 3D RSM run gives back most accurately the results of the LES run. This is the only simulation where the deviation of c_l and c_d from the reference does not exceed 15%. The steady RSM run shows extremely good agreement with the c_l (and at the same time extremely bad agreement with c_d) of the reference run. Nonetheless, due to the previously mentioned issues, the results of R10 should be rather discarded. It is important to mark the steady 2D $k - \omega$ run. The steady 2D $k - \omega$ run converged within 5 minutes, while for the 3D unsteady run almost 1 day of computational time was required. For this cheap price, the c_l results of R8 is more than acceptable. Although for Flettner rotors the drag coefficient has only secondary importance, it is worth noting that all of the eddy-viscosity models significantly underpredict the c_d of the LES run. As a conclusion from the comparisons of the drag and lift coefficients 2 cases seem to be promising: the unsteady RSM run due to its accuracy and the steady 2D $k - \omega$ because of its cost efficiency. In the next session the velocities in the wake of the cylinder will be examined, which has even higher impact on the interaction.

6.2. Velocities in the wake

In this section a realistic example is shown about how the incoming flow is influenced for a second cylinder which is placed in the wake of the first one. Enercon E-ship 1 was already shown in the introduction of the thesis in Figure 1.2d and in Figure 6.3 it can be seen from another angle. The ship is owned by the wind turbine manufacturer Enercon GmbH. She is in service from August 2010 so she is one of the first pioneering ships in the rebirth of wind-assisted shipping. Each of her 4 Flettner rotors has a diameter of 4 meter (without the end plate) and a height of 27 meter. We have seen in Figure 1.3 that thanks to her rotors fuel saving up to 45% can be achieved. The beam of the ship is 22.5 meter and according to Figure 6.3 the rotors have a base which is wider than the diameter of the rotors. Between the side of the deck and these bases there is a space enough to walk. Conforming to this, the distance between the rotational axis of two rotors which are at the same longitudinal coordinate is approximately 4 diameter.

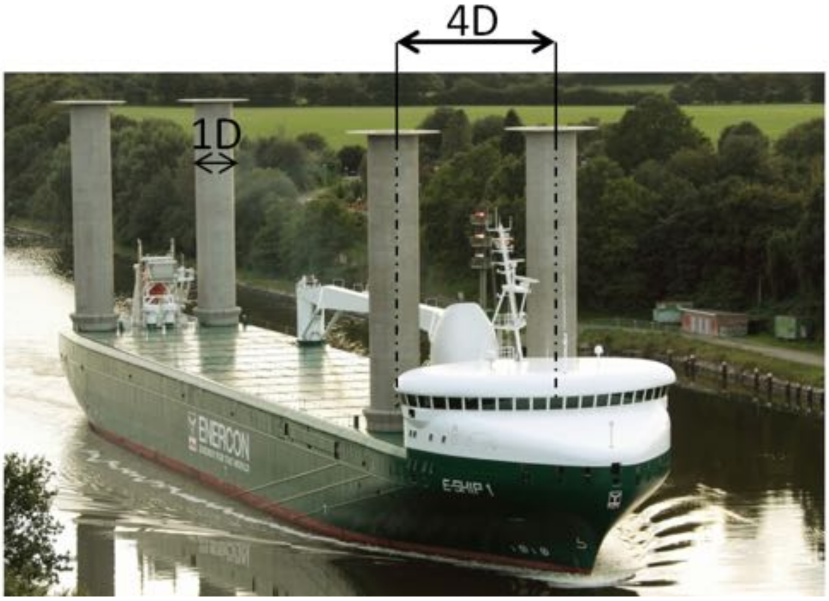

Figure 6.3.: Enercon E-Ship 1

A good indication of the wake effect is if we look at the incoming flow's velocities along a vertical line which is located just before the second cylinder. This line is marked with red in Figure 6.4 and in the following we refer to it as *affected region*. The choice of the position and the length of 3 diameter for the affected region are somewhat arbitrary.

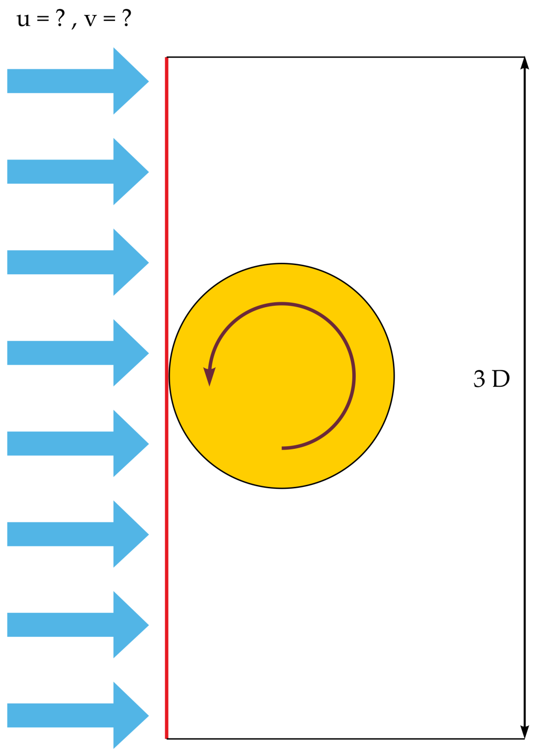

Figure 6.4.: Affected region

Furthermore, we should emphasize that the real flow field would obviously be different in the affected region since as we have seen in the streamlines plot the flow is already very disturbed because of the second cylinder. To take into account the effect of the second cylinder would be the subject of interaction study between the 2 cylinders which would be a topic of further work. Here, solely the effect of the first cylinder is considered and the performances of the different RANS models are tested by comparing the RANS runs with the reference LES run (L4).

From the time and space (averaged in the z direction) averaged flow field horizontal (along x axis) and vertical (along y axis) velocities were extracted along vertical lines at distance of 1.5D, 3D and 3.5D from the cylinder in the wake as depicted in Figure 6.5. Let us assume that the apparent wind is coming in the horizontal direction, the distance between the rotational axes (based on the E-Ship 1 example) is 4D and the cylinders rotate counterclockwise. By analogy to the first 2 rotors of E-Ship we imagine that the rotors are at the bow of the ship. In Figure 6.5 the dark grey marks the bow and consequently the angles (noted here as Θ) are the angles between the ship's direction and the apparent wind or in other words they are the heading angles to the apparent wind.

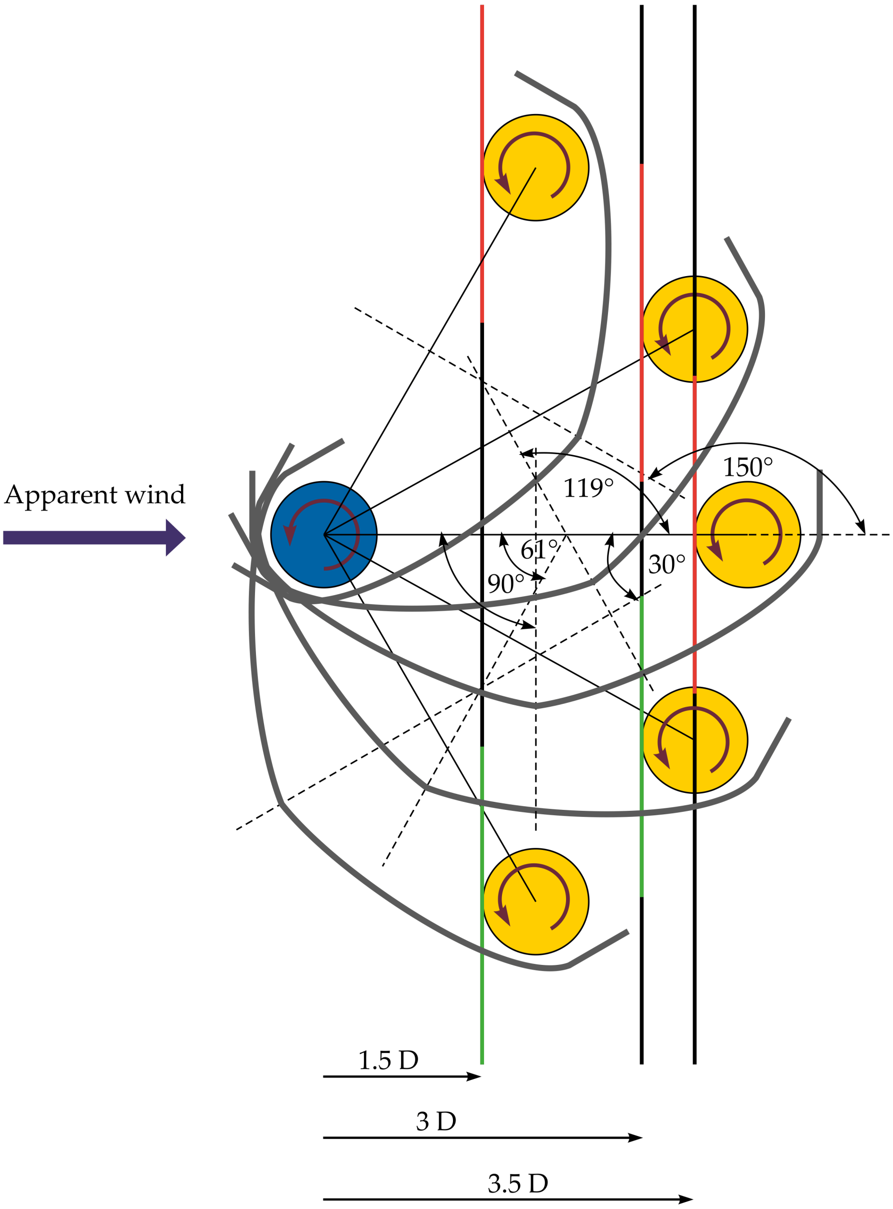

Figure 6.5.: Position of the second cylinder and the ship

In addition, one can see red and green segments on each vertical line. These segments mark the affected regions as in Figure 6.5, where the heading angle is: $\Theta \geq 90°$. In the following pages the velocity plots for the unsteady 3D RSM (R9) and for the 2D steady $k-\omega$ (R8) are depicted because of their importance. The velocity plots for the other runs can be found in Appendix B. The notation of the affected regions was kept for the graphs too. Green segments belong to $\Theta \leq 90°$ and the red ones to $\Theta < 90°$. In the plots, with black and blue '+' signs the velocities at the vertical coordinate of the center of the second cylinder (so these points are at (-0.5,0) in a coordinate system fixed to the second cylinder) are also marked.

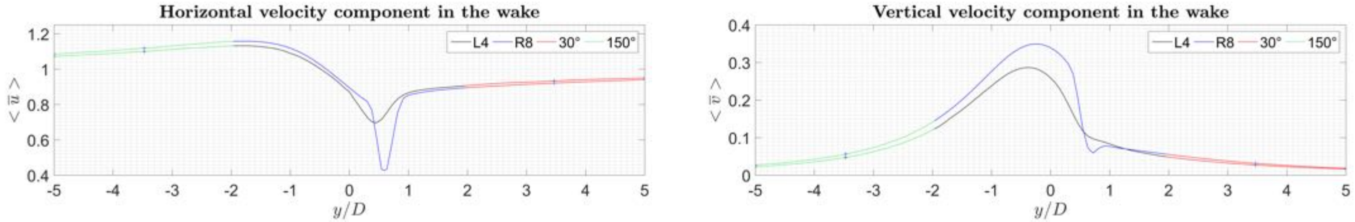

Figure 6.6.: Velocities with R8 at 30° and 150°.

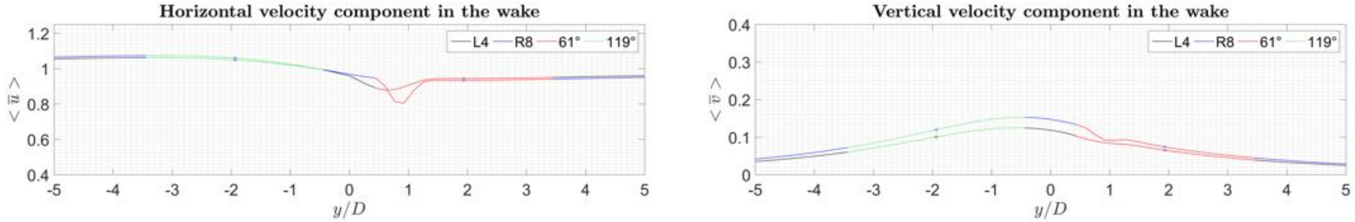

Figure 6.7.: Velocities with R8 at 61° and 119°.

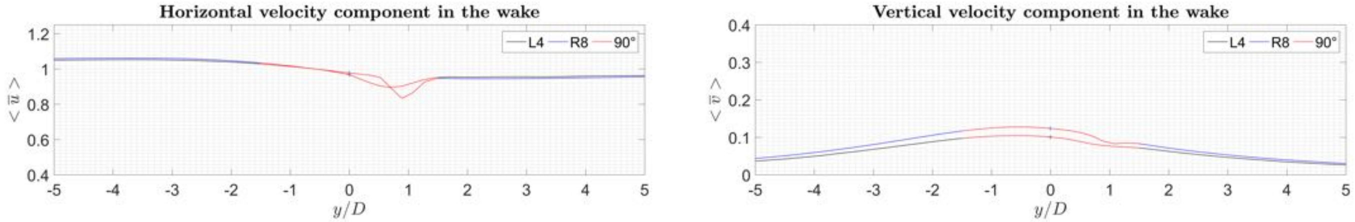

Figure 6.8.: Velocities with R8 at 90°

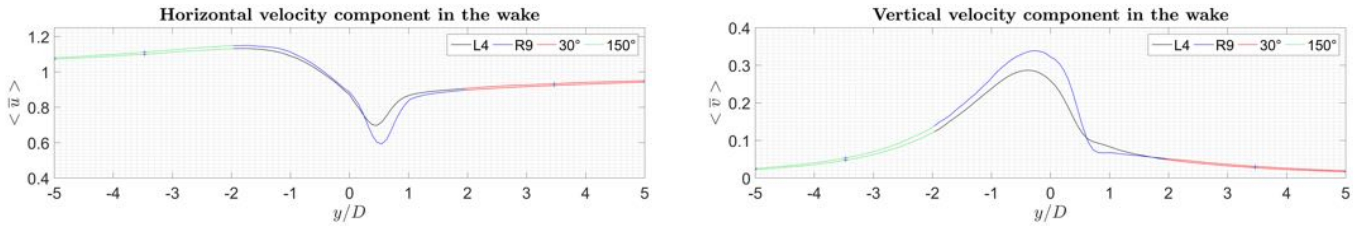

Figure 6.9.: Velocities with R9 at 30° and 150°.

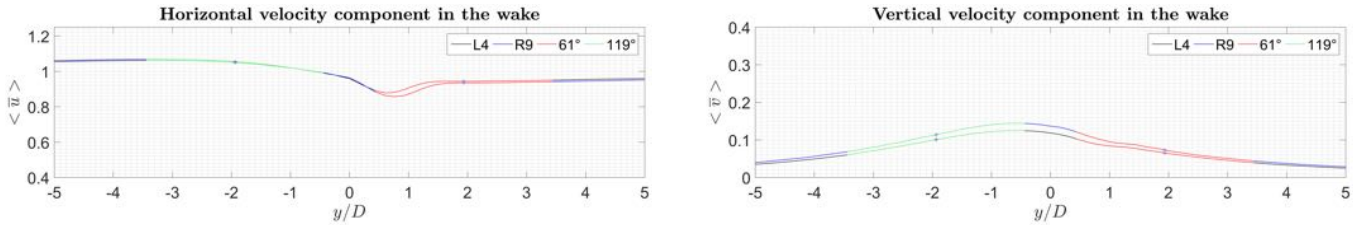

Figure 6.10.: Velocities with R9 at 61° and 119°.

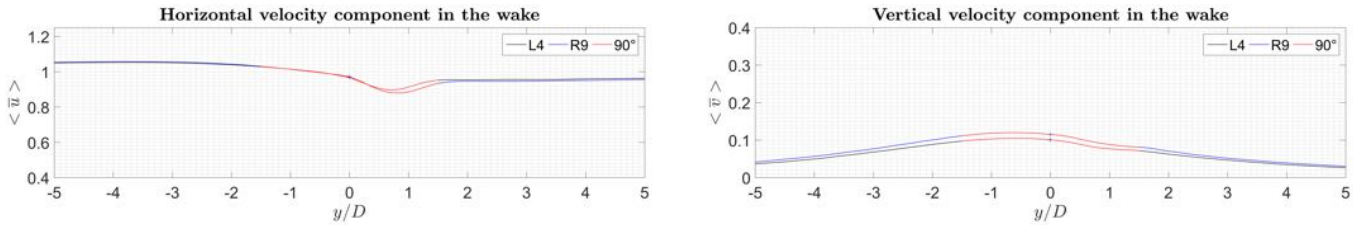

Figure 6.11.: Velocities with R9 at 90°

Looking at the results we see similar behaviour to the lift and drag values i.e. the $k-\epsilon$ performs the poorest and the RSM is the most accurate.
In general, one can see that the relative velocity difference from the reference LES run is greater in the vertical velocity component. Except a very tiny region which is close and almost behind to the first cylinder in Figure B.10 (the figure of the steady 2D $k-\epsilon$) run, the $k-\epsilon$ model always overpredicts the vertical velocity component. At the same position but over a wider region the $k-\omega$ model (Figure B.13, Figure B.16, Figure B.19 and Figure B.22) also underpredicts the vertical velocity component, otherwise the vertical velocities are overpredicted again. Since the inspected area where underpredicted velocities are popped up is not in the affected region, we can conclude that for this arrangement the second cylinder always experiences higher vertical velocity components with the eddy-viscosity models. The RSM models (Figure B.25–Figure B.33) do not always follow the trend of the eddy-viscosity models. Sometimes they give back smaller vertical velocities than the reference vertical velocities even at further distances from the cylinder. Nevertheless, the unsteady 3D RSM run which based on the aerodynamic coefficients was deemed to be the most accurate RANS model behaves similarly as the eddy-viscosity models, so in the affected regions it always gives back overpredicted vertical velocities.

After having a closer look at the horizontal velocity plots one can see a universal trend: the horizontal velocity component of the reference LES run is overpredicted for the negative y coordinates while it is overpredicted for most of the positive y coordinates. The change in the trend always happens in the region: $0 < y/D < 1$. To be exact, here we need to mention that the steady 3D RSM (R10) run shows a different trend (Figure B.28, Figure B.29 and Figure B.30). This fact, however just further strengthens the assumption that those results should be discarded. Generally, the further we go downstream from the cylinder the smaller the deviation from the reference is. However, close to the cylinder, especially in the plots of 30° and 150° which belong to the 1.5D distance from the cylinder huge differences can be seen! In the region: $0 < y/D < 1$ the reference horizontal velocity can be underpredicted by 20% even with the most accurate unsteady 3D RSM (R9) model (Figure 6.9) and by 40% with the economical 2D steady $k-\omega$ model (R8) (Figure 6.6). In the affected regions the velocities of the RANS runs show a quite good match with the velocities of the reference LES (L4) for the arrangement of 30° and 150°. However, we should not forget that the distance of 4D for the cylinders' rotational axes was arbitrarily chosen. If the cylinders were closer to each other the affected regions would move closer to the horizontal centerline of the first cylinder (as it does with 4D for higher angles) and touch the highly underpredicted regions. Consequently these findings suggest that there is a lower limit for the distance between the cylinders. In case of the distance between the cylinders does not exceed this limit, there will be highly undepredicted incoming velocities for the second cylinder. Next, let us have a look at the plot of 61° and 119° and the plot of 90° which belong to distance: $x = 3D$ and $x = 3.5D$ respectively. One can see that in these plots the red affected region and the region of the most distorted velocities coincide. The most important findings, now solely for the two most viable models, so for the 2D steady $k-\omega$ (Figure 6.7 and Figure 6.8) and for the 3D unsteady RSM (Figure 6.10 and Figure 6.11):

- For 119° the horizontal velocities are almost identical with the reference LES velocities in the affected region for both runs
- For 61° according to the '+' signs the bigger deviation from the reference horizontal

velocities are on the suction side of the second cylinder. With the $k - \omega$ run closer to the cylinder the velocities are underpredicted while away from the cylinder, in the end of the affected region the velocities are overpredicted. The RSM run underpredicts the velocities everywhere on the suction side, however its global deviation from the reference LES velocities is significantly smaller than that of the $k - \omega$ model. On the pressure side with both models the velocities are almost identical with the reference, they are just slightly underpredicted.

– Contrary to the case of 61°, for 90° the suction side is the side where the velocities almost match perfectly with the reference velocities for both runs.

Considering the effect of these changes in the incoming flow field without involving the interaction effect cannot be done accurately. Nonetheless, there is one finding whose consequence at least seems to be evident, namely the overpredicted vertical velocity component. Even with the most accurate RSM model the vertical velocity component is overpredicted by 10-15% everywhere in the affected regions. The higher vertical velocity component will provide additional pressure to the suction side, which results in lift reduction. However, the bigger vertical velocity component surely will influence the location of the separation points too. The larger vertical velocity will accelerate the separation and also its pace on the pressure side. Besides, by pushing the flow towards the surface of the cylinder it makes the flow stay attached longer and the lower separation points might move to the pressure side. Such displacements of the separation points are in favour of lift production. Consequently, in terms of lift production the larger pressure on the suction side and the displacement of the separation points counteract. Depending on which effect is the stronger we have lift production or reduction from the changed velocity field. Or in other words, even what seems to be evident is not evident. Therefore further guesses for the effects of the changed flow field on the second cylinder are not presented here, and a thorough examination with two cylinders is suggested.

Finally, let us have a closer look at the results of the unsteady 3D (Figure B.13, Figure B.14 and Figure B.15) and the steady 2D $k-\omega$ (Figure 6.6, Figure 6.6 and Figure 6.6) runs. The biggest deviations can be seen in the horizontal velocity component for the 30° and 150° arrangements. The area of the differences is behind the pressure side of the first cylinder ($0.5 < y/D < 1$). Although there are differences at further distances from the cylinder but the most pronounced ones belong to the 30° and 150° arrangement so to 1.5D distance from the first cylinder. Consequently, as long as someone does not choose the distance between the cylinders' axes to be small (for distances close to the cylinder the mentioned area is kept out from the affected region) the 3 dimensionality and the unsteadiness do not provide too much further information.

6.3. Grid dependency

As we have seen the first step was to examine the viability of the RANS models. Therefore, the resolution of the grid in the previous analyses was chosen to be fine. However, after knowing that the $k - \omega$ and the RSM models could be used for filling up the database of the PPP, a cost reduced solution is desirable. Here, the 3D unsteady case with the $k - \omega$

model and with the *RSM* model will be tested. In Figure 6.12 one can see the used grid's structure.

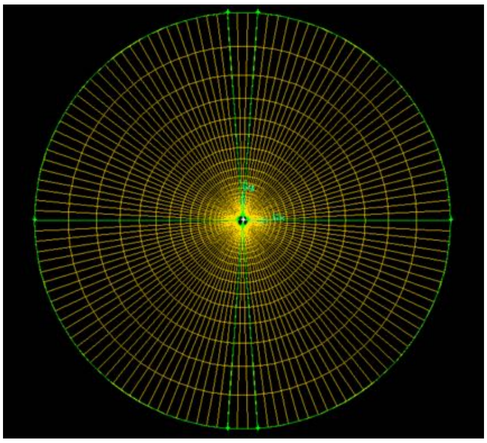

Figure 6.12.: G7 the computational mesh for the coarse RANS runs

The grid remained very fine close to the wall (wall y^+ is smaller than 5 everywhere around the cylinder), thus a big variation in the aerodynamic coefficients is not excepted. Nevertheless, one can see that the growth ratio between cells has increased significantly and hence this grid is significantly coarser in the wake area. A very important question is whether the poor resolution of the wake spoils the wake velocity results. Table 6.3 shows the identification and the main parameters of the runs:

Id.	Model	Grid	α	Re	Dim.	Type
R12	$k-\omega$ (M4)	G7	2	140 000	3D	Unsteady
R13	RSM (M5)	G7	2	140 000	3D	Unsteady

Table 6.3.: Coarser RANS runs

Table 6.4 shows the lift and drag coefficients with the original and with the coarser grid:

Id.	Model	Type	Dim.	Grid	cl_{mean} $[-]$	cd_{mean} $[-]$
R12	$k-\omega$	Unsteady	3D	coarse	5.3787	0.1002
R5	$k-\omega$	Unsteady	3D	fine	5.4284	0.1025
R13	RSM	Unsteady	3D	coarse	5.0100	0.1025
R9	RSM	Unsteady.	3D	fine	5.0431	0.1362

Table 6.4.: Mean lift and drag coefficients with the original and the coarser mesh for the 3D unsteady runs with the $k-\omega$ and the RSM models

As was expected there is just a very small variation in the coefficients. The results for the wake velocities were plotted together with the fine grid's result and can be found in Figure 6.13–Figure 6.18. One can see that there are differences, however just moderate ones. The area of the biggest differences is the wake behind the pressure side so it is the same region as it was in the RANS-LES comparison cases. The almost identical velocity results for the areas outside $0 < y/D < 2$ suggest that the grid could be made even coarser in these regions. The saved grid points then could be used to refine the grid in the wake behind the pressure side and hence improving the accuracy in that area. As a result even more accurate data could be obtained while keeping the costs to be low. In conclusion, we can say that although the solution is not grid independent, the results obtained with the coarser grids are more than acceptable. In addition, the observed weak sensitivity for the grid resolution of the RSM model makes that model very promising for the future research.

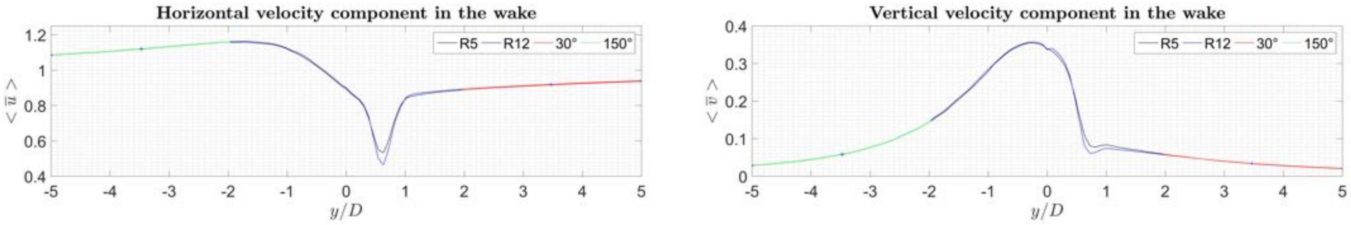

Figure 6.13.: Velocities with R5 and R12 at 30° and 150°.

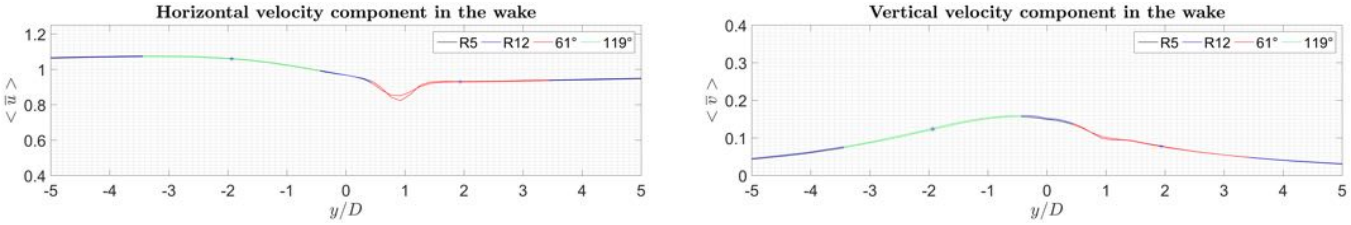

Figure 6.14.: Velocities with R5 and R12 at 61° and 119°.

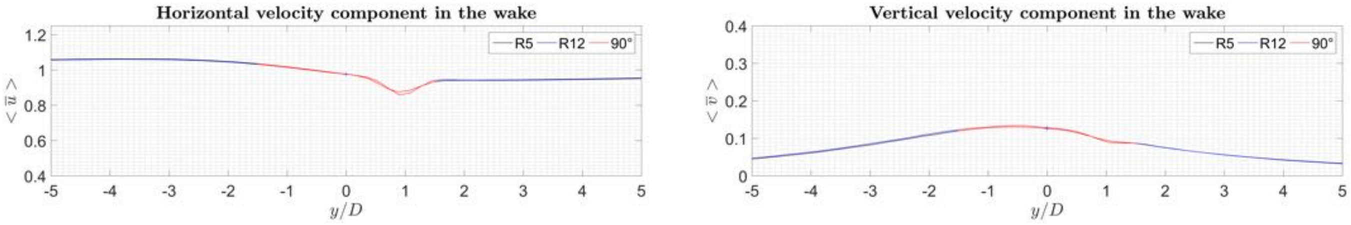

Figure 6.15.: Velocities with R5 and R12 at 90°

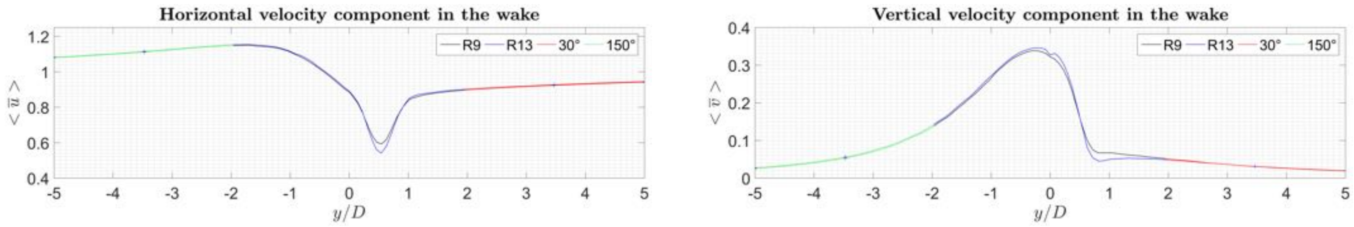

Figure 6.16.: Velocities with R9 and R13 at 30° and 150°.

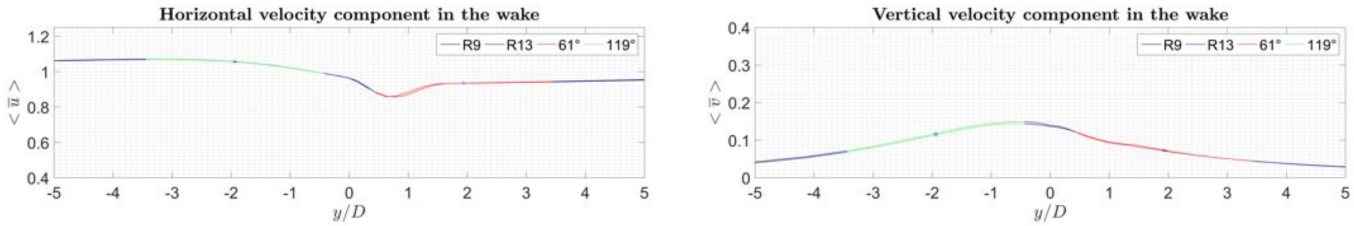

Figure 6.17.: Velocities with R9 and R13 at 61° and 119°.

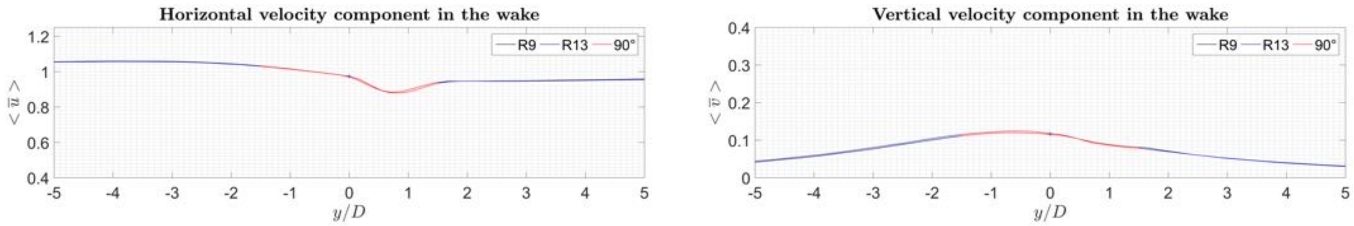

Figure 6.18.: Velocities with R9 and R13 at 90°

7. Conclusion and recommendation for further works

7.1. Conclusion

In the present work thorough examination was carried out with a flow around a spinning cylinder. The Reynolds number and the rotational ratio was chosen to ensure that the flow is in the regime which is representative for flow around Flettner-rotors (transcritical regime). The goal of the examination was to evaluate the performance of different LES and RANS turbulence models.

First we compared two LES subgrid models: the Smagorinsky-Lilly and the WALE models. The analysis showed that the boundary layer around a rotating cylinder is complex and it comprises of:

- an *inner portion*: a portion which moves bonded to surface of the cylinder and it was called rotating boundary layer (RBL)
- an *outer portion*: which flows in the direction of the free stream. Depending on which side we look at, this stream slides over or slides with the RBL.

According to the WALE model the boundary layer is significantly thinner than it was observed with the Smagorinsky model. The main difference comes from the fact that the Smagorinsky model produces too large subgrid viscosity in the near wall area, and hence it makes the RBL fully turbulent. On the contrary, in the WALE model a correct damping of the subgrid viscosity is incorporated, which ensured the RBL to stay laminar everywhere around the cylinder. The laminar RBL is less capable of deflecting the incoming flow as a result:

- A significantly thinner vortex formation was present on the pressure side with the WALE run
    - This thinner vortex does not penetrate as much into the free stream as the vortex of the Smagorinsky model does.
    - The smaller penetration results in smaller wake deflection.
- The flow separates under a smaller angle in the WALE model.
    - Because of the smaller separation pace the overall pressure reduction in the quadrant which belongs to the front cap of the top side of the cylinder was greater for the WALE case.

- This pressure reduction was clearly seen in the pressure coefficient plots. The pressure coefficients for the two models were identical in all but the mentioned region.
- The lower pressure of the area reduced the lift coefficient by 5% and the drag coefficient by 23% for the WALE model.

Contrary to the choice of the subgrid model, the grid refinement and domain extension for LES simulations have shown only minor effects. Finally, the WALE run (L4) with the refined mesh and with a 2 cylinder diameter height was deemed to be the most accurate simulation.

In the second part of the analysis several RANS runs were carried out with the $k-\epsilon$, $SST\,k-\omega$ and $RSM\,stress-\omega$ models. The evaluation of these simulations was based on the comparison of the aerodynamic coefficients and the wake velocities with the reference LES run (L4). The 3 dimensionality of the flow has only been clearly seen for the RSM case. Besides, the fact that the flow is in the regime where vortex shedding has died out, raised the question whether a steady and an unsteady run would give the same results. The results of the eddy-viscosity models showed very little difference for the steady and the unsteady case. However, the RSM model was more sensitive for the unsteadiness: convergence could not be reached with the steady RSM 3D case and the domain we used was not appropriate for the steady 2D RSM case. The fluctuation of the lift and drag coefficient with the steady 3D RSM run suggests that the RSM model still regards the flow to be unsteady. The comparison has suggested two models for further work, namely:

- 3D unsteady RSM run because of its accuracy.
- 2D steady $k-\omega$ run because of its prominent cost-accuracy ratio.

Grid dependency analysis was performed for the 3D unsteady RSM and the 3D unsteady $k-\omega$ models. The analysis has shown that the models have a weak sensitivity on the grid's resolution, which is very promising for the main research.

The required time for the simulations is very important in terms of the future research. During the thesis qualifiers 'faster' and 'slower' have been used many times. To have a clearer picture about the meaning of these qualifiers for the present work, in Table 7.1 the run-time of some jobs is indicated. The unsteady simulations have been ran on the same cluster and they depict the required simulation time for 100 dimensionless time-steps. The two 2D steady runs show the required simulation time for their convergence. These steady simulations were running on a significantly slower cluster, but still their simulation time is just a moment comparing to the simulation times of the unsteady ones.

Id.	Model	Type	Dim.	Time $[hrs]$	Comment
L4	WALE	Unsteady	3D	119	Double span!
R1	$k-\epsilon$	Unsteady	3D	11	-
R4	$k-\epsilon$	Steady	2D	0.1	Slower cluster
R5	$k-\omega$	Unsteady	3D	22	-
R8	$k-\omega$	Steady	2D	0.08	Slower cluster
R9	RSM	Unsteady	3D	41	-
R12	$k-\omega$	Unsteady	3D	8	Coarser grid
R13	RSM	Unsteady	3D	8.5	Coarser grid

Table 7.1.: Simulation times

It is very important to note that only the WALE run with the height of 2 cylinders diameter was running on this powerful cluster. Since the resolution of the grid was kept constant and only the height of the domain doubled, the WALE run with 1 diameter height would last for around 60 hours. One can see that due to the larger number of equations (comparing to LES +8 equations) on a fine grid the $RSM\, stress-\omega$ model has comparable run-time to the LES run-time. However, the coarser grid yielded a 5-fold decrease in the simulation time. Although this is a significant cost reduction, the cost of the 3D unsteady RSM model with the coarse grid is still 85 times higher than that of the 2D steady $k-\omega$. The question whether the 3 dimensionality is necessary for the interaction can be only answered after runs for 2 cylinders. Morover, at a further stage the research should involve true Flettner-rotors with end-plate, where obviously a 2D model cannot be used. The physics of the flow in the vicinity of the end-plate is complex so that to handle it with RANS models surely will be a challenge. Nevertheless, at least this thesis work has proved that the $RSM\, stress-\omega$ model can operate with a good accuracy-cost ratio on a flow around a spinning bare cylinder.

7.2. Recommendations

As we can see this thesis work is a starting point of the Flettner-rotor field of the wind assisted ship propulsion's research of TU Delft and POLIMI. Hence, there are many things to do. Here some of the most interesting recommendations are mentioned:

- Although it is not strongly connected to the research, it would be interesting to see whether the WALE model is capable of capturing the boundary layer transition (i.e. the Inverse Magnus Effect) for smaller rotational speed. Some trials were performed during the thesis work. Those results did not show transition and confirmed that even if there is transition with the WALE model, the grid should be extremely fine to be able to tackle it.
- Trying out another RSM models apart from the $RSM\, stress-\omega$ would make sense.
- It is also advisable to continue the grid dependency analysis. For instance by making finer the grid in the wake behind the pressure side and coarser elsewhere.
- Surely it is not an easy task, but due to the fast simulation time with tuning the coefficients in the eddy-viscosity models the accuracy of the 2D steady runs might be

increased.

- With the results of this work it is already worth to start the vortex methods analysis.
- The research has arrived to the stage where the examination for more cylinders is already possible.

Bibliography

[1] *Third IMO Greenhouse Gas Study*. International Maritime Organization, 2014. URL: `http://www.imo.org/en/OurWork/Environment/PollutionPrevention/AirPollution/Documents/Third\%20Greenhouse\%20Gas\%20Study/GHG3\%20Executive\%20Summary\%20and\%20Report.pdf`.

[2] "Enercon E-Ship 1 A Wind-Hybrid Commercial Cargo Ship." In: *4th Conference on Ship Efficiency*. Hamburg, Sept. 2013.

[3] M. Caponetto. "The aerodynamic interference between two boats sailing close-hauled." In: *International shipbuilding progress* 44.439 (1997). Ed. by Delft University Press, pp. 241–256. ISSN: 0020-868X.

[4] K. Roncin and J.M. Kobus. "Dynamic simulation of two sailing boats in match racing." In: *Sports Engineering* 7.3 (2004), pp. 139–152. ISSN: 1460-2687. DOI: `10.1007/BF02844052`. URL: `http://dx.doi.org/10.1007/BF02844052`.

[5] F. Homann. "Der Einfluß großer Zähigkeit bei der Strömung um den Zylinder und um die Kugel." In: *ZAMM - Journal of Applied Mathematics and Mechanics* 16.3 (June 1936), pp. 153–164. DOI: `10.1002/zamm.19360160304`.

[6] B.M. Sumer and J. Fredsøe. *Hydrodynamics Around Cylindrical Structures*. Advanced series on ocean engineering. World Scientific, 1997. ISBN: 9789810228989. URL: `https://books.google.nl/books?id=yJPHN\_VXwfIC`.

[7] W. M. Swanson. "The Magnus Effect: A Summary of Investigations to Date." In: *Journal of Basic Engineering* (Sept. 1961), pp. 461–470.

[8] SJ Karabelas. "Large eddy simulation of high-Reynolds number flow past a rotating cylinder." In: *International journal of heat and fluid flow* 31.4 (2010), pp. 518–527.

[9] S. Rolfo and A. Revell. "Effect of Span-Wise Resolution for LES of Flow Over a Rotating Cylinder at High Reynolds Number." In: *Direct and Large-Eddy Simulation IX*. Ed. by Jochen Fröhlich et al. Cham: Springer International Publishing, 2015, pp. 479–486. ISBN: 978-3-319-14448-1. DOI: `10.1007/978-3-319-14448-1_61`. URL: `http://dx.doi.org/10.1007/978-3-319-14448-1_61`.

[10] L. Prandtl. "The Magnus effect and wind-powered ships." In: *Naturwissenschaften* 13 (1925), pp. 93–108.

[11] Tim Craft et al. "Back to the Future? A Re-examination of the Aerodynamics of Flettner-Thom Rotors for Maritime Propulsion." In: *Flow, Turbulence and Combustion* 92.1 (2014), pp. 413–427. ISSN: 1573-1987. DOI: `10.1007/s10494-013-9486-4`. URL: `http://dx.doi.org/10.1007/s10494-013-9486-4`.

[12] A. Thom and Great Britain. Aeronautical Research Committee. *Effect of Discs on the Air Forces on a Rotating Cylinder*. Air Ministry. Aeronautical Research Committee. Reports and memoranda. Stat. Office, 1935.

[13] B.R. Clayton. "BWEA initiative on wind assisted ship propulsion (WASP)." In: *Wind Engineering and Industrial Aerodynamics* 19(1-3) (July 1985), pp. 251–276. DOI: `10.1016/0167-6105(85)90064-9`.

[14] Tim Craft et al. "Back To The Future: Flettner-Thom Rotors For Maritime Propulsion?" In: *Turbulence, Heat and Mass Transfer 7* 1 (2012). DOI: `10.1615/ICHMT.2012.ProcSevIntSympTurbHeatTransfPal.1150`.

[15] KM Lam. "Vortex shedding flow behind a slowly rotating circular cylinder." In: *Journal of Fluids and Structures* 25.2 (2009), pp. 245–262.

[16] K. Mobini and M. Niazi. "Large Eddy Simulation of Low Subcritical Reynolds NumberFlow across a Rotating Circular Cylinder." In: *WSEAS Transactions on Fluid Mechanics* 8 (July 2013), pp. 131–140.

[17] Elliott G. Reid. "Tests of Rotating Cylinders." In: (Dec. 1924).

[18] Katsumi Aoki and Takeshi Ito. "Flow Characteristics around a Rotating Cylinder." In: *Proc. Schl. Eng. Tokai Unix,Ser, E* 26 (2001), pp. 29–34.

[19] C. Badalamenti and S. Prince. "The Effects of Endplates on a Rotating Cylinder in Crossflow." In: *28th, AIAA Applied Aerodynamics Conference Honolulu, HI.* Reston, Va.: American Institute of Aeronautics and Astronautics, Aug. 2008.

[20] Tim Craft, Hector Iacovides, and Brian Launder. "Computational modelling of Flettner-rotor performance with and without Thom discs." In: *Proc.7th Conf. on Eng'ng Turbulence Modelling Measurement.* Marseilles, June 2010, pp. 152–157.

[21] Tim Craft, Hector Iacovides, and Brian Launder. "Dynamic performance of Flettner rotors with and without Thom discs." In: *Proc. 7th Symp. on Turbulence Shear Flow Phenomena, Paper 6C-3.* Ottawa, July 2011.

[22] *FLUENT 6.3 User's Guide.* URL: `https://www.sharcnet.ca/Software/Fluent6/html/ug/main_pre.htm`.

[23] Stephen B. Pope. *Turbulent Flows.* Cambridge University Press, 2001.

[24] Michael Breuer. "A challenging test case for large eddy simulation: high Reynolds number circular cylinder flow." In: *International Journal of Heat and Fluid Flow* 21.5 (2000). Turbulence and Shear Flow Phenomena 1, pp. 648 –654. ISSN: 0142-727X. DOI: `http://dx.doi.org/10.1016/S0142-727X(00)00056-4`. URL: `http://www.sciencedirect.com/science/article/pii/S0142727X00000564`.

[25] Dr.ir. W.-P. Breugem. "Lecture Slides of Turbulence A." TU Delft, Course code: WB1424ATU. Academic year: 2014-2015, Q3.

[26] Donald Coles. "The law of the wake in the turbulent boundary layer." In: *J. Fluid Mech.* 1 (1956), pp. 191–226.

[27] Stephen B. Pope. "Ten questions concerning the large-eddy simulation of turbulent flows." In: *New Journal of Physics* 6 (2004), pp. 1–24.

[28] Milton Van Dyke. *An Album of Fluid Motion.* 1982.

[29] D. K. Lilly. "The representation of small-scale turbulence in numerical simulation experiments." In: *Proc. IBM Scientijc Computing Symp. on Environmental Sciences.* Yorktown Heights, NY: IBM, Nov. 1966, pp. 195–210.

[30] P. Moin Kim J. and R. Moser. "Turbulence statistics in fully developed channel flow at low Reynolds number." In: *J. Fluid Mech.* 177 (1987), pp. 133–166.

[31] David R. Dowling Marc Perlin and Steven L. Ceccio. "Freeman Scholar Review: Passive and Active Skin-Friction Drag Reduction in Turbulent Boundary Layers." In: *Journal of Fluids Engineering* 138 (2016).

Appendices

A. Turbulence modelling

In this chapter a summary about the used turbulence models is intended to give. Turbulence is a very broad topic in engineering, thus here only the basics can be discussed. Apart from deriving the governing equations special emphasis will put on the implementation in FLUENT.

A.1. Introduction

The present problem is governed by the incompressible Navier-Stokes equations. The continuity:

$$\frac{\partial u_i}{\partial x_i} = 0 \tag{A.1}$$

and the 3 momentum equations:

$$\frac{\partial u_i}{\partial t} + u_j \frac{\partial u_i}{\partial x_j} = -\frac{1}{\rho}\frac{\partial p}{\partial x_i} + \nu \frac{\partial^2 u_i}{\partial x_j^2} \tag{A.2}$$

In fluid dynamics it is conventional to introduce the material or substantial differential operator:

$$\frac{D}{Dt} \equiv \frac{\partial}{\partial t} + \vec{u} \cdot \bigtriangledown \tag{A.3}$$

With the help of the above mentioned definition Equation (A.2) can be rewritten as:

$$\frac{Du_i}{Dt} = -\frac{1}{\rho}\frac{\partial p}{\partial x_i} + \nu \frac{\partial^2 u_i}{\partial x_j^2} \tag{A.4}$$

Due to the advection term (2^{nd} term on the left hand side in Equation (A.2)) the Navier-Stokes equations are non-linear differential equations. Mathematicians have been struggling with finding a solution for this type of equation for long time. They had no success in it so far. The problem is that with increasing the Reynolds number the effect of the nonlinear-term is more pronounced, hence the flow becomes more complicated. As a result, in most of the cases there will be more than one solution for the equations. Among the solutions, one will find time-dependent and unstable ones too. Unstable solutions can grow in time and quickly dominate the flow, thereby making the flow more and more complicated or even chaotic. In fluid dynamics we refer to these chaotic situations as turbulent flows.

In these type of flows turbulent motions extract energy from the flow through fluctuating motions. The fluctuations cause local instabilities inside the flow, as a result of these instabilities vortical structures, eddies pop up in the flow. These large eddies (the macro structures of the flow) are scaled with the characteristic length scale of the main flow:

$$u_0 \sim U \tag{A.5}$$

$$l_0 \sim L \tag{A.6}$$

in which scales denoted by capital letters refer to the scales of the main flow, whilst scales with lowercase letters and 0 subscripts to the scales of the macro structures. Furthermore, the energy extracted from the bulk is used for feeding these large eddies. Large eddies are unstable, thus they break up to smaller ones. This procedure continues till the eddies reach a size at the Kolmogorov lengthscale where they are stable. Finally, the energy extracted by the turbulent fluctuations dissipates at the Kolmogorov scale, increasing the internal energy of the fluid. This process is called Richardson energy cascade and is summed up in Figure A.1. Between the production conducted large and dissipation dominated Kolmogorov scales in the energy transport one more scale is present. This is the inertial subrange where production and dissipation are equally important.

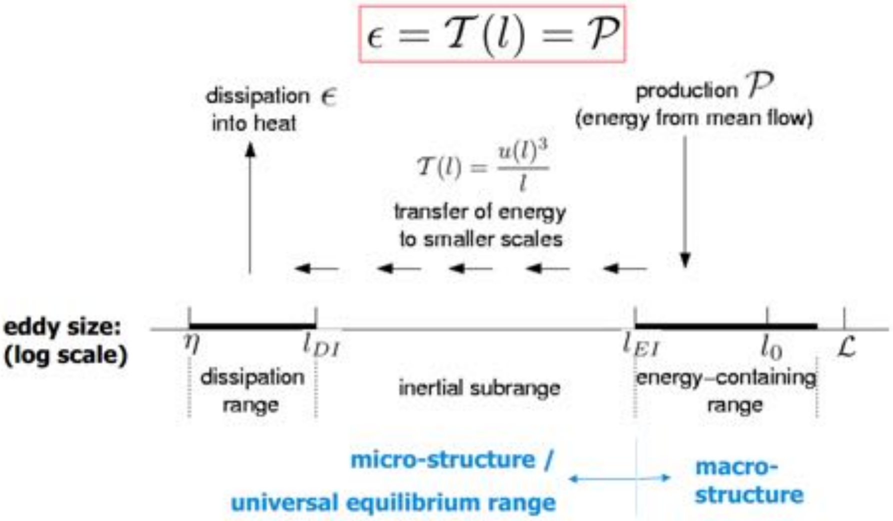
$\epsilon = \mathcal{T}(l) = \mathcal{P}$
dissipation ϵ into heat
production $\mathcal{P}$ (energy from mean flow)
$\mathcal{T}(l) = \frac{u(l)^3}{l}$
transfer of energy to smaller scales
eddy size: (log scale)
η
l_{DI}
l_{EI}
l_0
$\mathcal{L}$
dissipation range
inertial subrange
energy-containing range
micro-structure / universal equilibrium range
macro-structure

Figure A.1.: Schematic diagram of the energy cascade. Taken from Breugem [25]

According to the Richardson cascade the amount of turbulent energy extracted from the bulk is determined by the large eddies which are in the energy containing range. Figure A.2 shows the nature of the flow in the energy containing range as well as in the dissipation range.

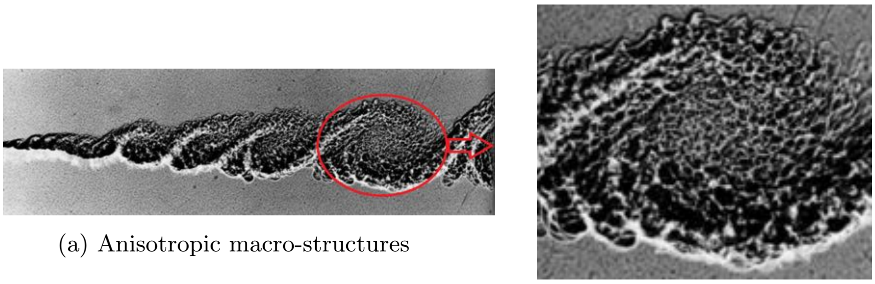

(a) Anisotropic macro-structures

(b) Isotropic micro-structures

Figure A.2.: Different scales in a turbulent mixing layer. Picture is taken from Van Dyke [28]

The pictures unambiguously depict the enormous difference between the two lengthscales' size. Furthermore, it is very important to note that the motions are not only different in their size but in their nature as well. The flow is strongly anisotropic at large scales, since the direction of the large eddies is determined by the bulk flow, whilst at Kolmogorov scale it is not possible to determine any dominant direction in the flow, so that small eddies are isotropic. Therefore, as one is moving towards smaller and smaller scales, inevitable information loss emerges about the creation of the smaller eddies and regarding the nature of the main flow.

We have seen that the Navier-Stokes equations cannot be solved (at least according to the current stage of science) analytically. However, they can be solved numerically and this is the subject of computational fluid dynamics. In order to numerically solve the Navier-Stokes equations one should either:

- discretise them on a grid which has resolution until the Kolmogorov scale, and directly solve them without turbulence modelling, this what we call direct numerical simulation (DNS), or
- apply turbulence model(s) in which the whole or just a fraction of the fluctuating part of the velocities is modelled.

In the next sections the two aforementioned approaches will be summed up. The current computations were carried out with RANS models as well as with Large Eddy Simulation (LES), thus these methods will be introduced in more detail.

A.2. Direct Numerical simulation (DNS)

The main disadvantage of the DNS is its computational cost, which makes it simply infeasible for high Reynolds numbers. The viscous dissipation rate scales as:

$$\epsilon \sim \frac{u_0^3}{l_0} \tag{A.7}$$

With the help of the viscous dissipation we can define the Kolmogorov length and velocity scales:

$$\eta = \left(\frac{\nu^3}{\epsilon} \right)^{1/4} \tag{A.8}$$

$$u_\eta = (\epsilon \nu)^{1/4} \tag{A.9}$$

So for the Reynolds number of the Kolmogorov scales we get that:

$$Re_\eta = \frac{u_\eta \eta}{\nu} = \frac{(\epsilon\nu)^{1/4} \left(\frac{\nu^3}{\epsilon} \right)^{1/4}}{\nu} = 1 \tag{A.10}$$

This proves the previous assumption that the viscous dissipation can play a role in a scale, where $Re \sim 1$. Let us assume two flows with the same geometry but different Reynolds number. The change in the Reynolds number is thus either associated with growth in the flow's velocity scale (and hence growth in the velocity scale of the macro structures) or diminution in viscosity. According to Equation (A.7) in case of greater velocity scale the large eddies provide more energy to the smaller scales than in the smaller velocity scale case. This implies that u_η should increase too. In order to keep the Reynolds number equal to 1 η should decrease. In other words, small eddies are still too energetic, they should break up even further to reach the stable case where $Re \sim 1$ so that they can be dissipated. Now, we consider the case where the velocity scale remains unchanged and the viscosity decays. In agreement with (A.7) the provided energy by the large scales does not vary either. However, conforming to Equation (A.8) the Kolmogorov lengthscale should decrease again. This means that in both cases we need to increase the resolution of the grid to be able to capture the smaller motions. With the help of Equation (A.8) the ratio between the micro and macroscales:

$$\frac{l_0}{\eta} \sim \left(\frac{u_0 l_0}{\nu} \right)^{3/4} \sim \left(\frac{UL}{\nu} \right)^{3/4} = Re^{3/4} \tag{A.11}$$

so that the number of grid cells should scale with $Re^{3/4}$ as well in order to fulfil the required resolution which really reveal the infeasibility of DNS for high Reynolds number.

A.3. Turbulence models

Unlike DNS, turbulence models cannot directly calculate all fluctuations in the flow field. As it was mentioned in the introduction, turbulence is represented by stochastic signals. In concern with Figure A.3 a stochastic signal can be decomposed into a resolved and a residual part. The base of turbulence modelling is that only the resolved part of the stochastic signals is calculated and the effect of the residual part is modelled. In order to obtain turbulence models one should apply operators on the Navier-Stokes equations and solve these model equations. Depending on the nature of the operator we can distinguish two distinct modelling techniques:

- the mean variables are calculated and all the turbulence fluctuations reside in the model
- certain amount of the turbulent fluctuations are calculated and only a fraction of the turbulent fluctuations is modelled

The most used Reynolds Averaged Navier-Stokes (RANS) model belongs to the first category, whereas Large Eddy Simulation belongs to the second.

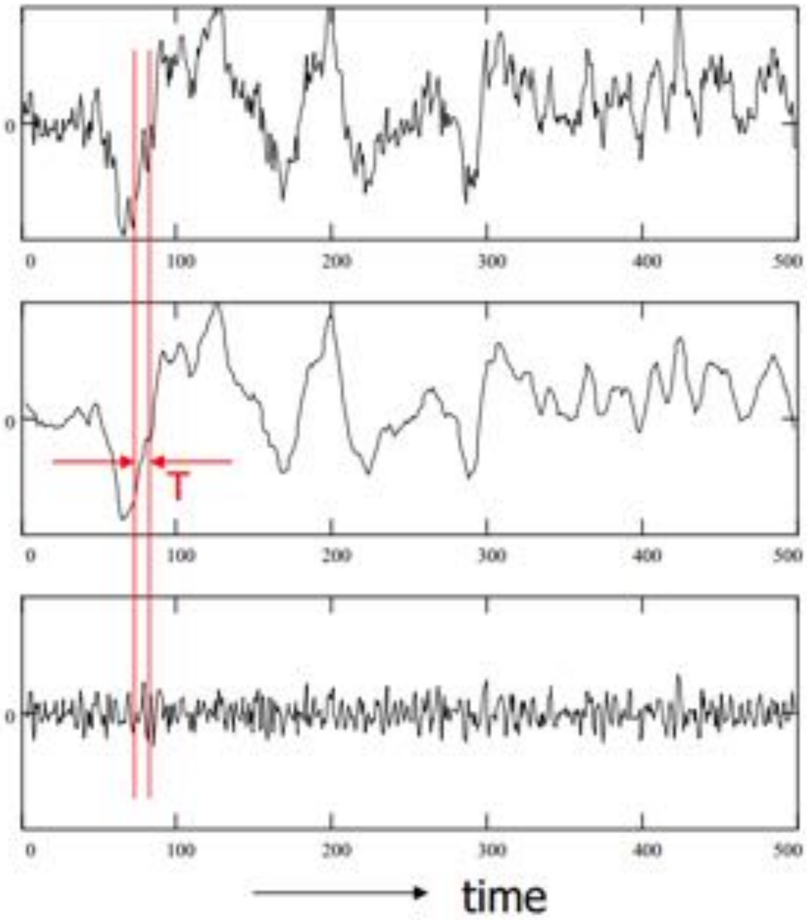

Figure A.3.: Stochastic signal and its decomposition. Upper picture: the signal itself, middle picture: the mean of the signal, lower picture: the fluctuating part of the signal. Taken from Breugem [25]

A.3.1. RANS models

According to the Reynolds decomposition an arbitrary signal can be divided into a mean and a fluctuating part (see also in Figure A.3):

$$f = \langle f \rangle + f' \tag{A.12}$$

where $\langle\ \rangle$ indicates the mean value and $'$ marks the fluctuating part.

RANS equations

In the Reynolds Averaged Navier-Stokes models one applies the Reynolds averaging operator on the continuity Equation (A.1) together with the momentum Equations (A.2). The resulting RANS equations:

$$\frac{\partial \langle u_i \rangle}{\partial x_i} = 0 \tag{A.13}$$

$$\frac{\partial \langle u_i \rangle}{\partial t} + \langle u_j \rangle \frac{\partial \langle u_i \rangle}{\partial x_j} = -\frac{1}{\rho}\frac{\partial \langle p \rangle}{\partial x_i} + \nu \frac{\partial^2 \langle u_i \rangle}{\partial x_j^2} - \frac{\partial \langle u_i' u_j' \rangle}{\partial x_j} \tag{A.14}$$

By analogy to Equation (A.3), we can also apply the Reynolds averaging operator to form the mean material derivative operator:

$$\frac{\langle D \rangle}{Dt} \equiv \frac{\partial}{\partial t} + \langle \vec{u} \rangle \cdot \triangledown \tag{A.15}$$

Rewriting Equation (A.14) with Equation (A.15) we arrive to a more compact form of the RANS equations:

$$\frac{\langle D \rangle \langle u_i \rangle}{Dt} = -\frac{1}{\rho}\frac{\partial \langle p \rangle}{\partial x_i} + \nu \frac{\partial^2 \langle u_i \rangle}{\partial x_j^2} - \frac{\partial \langle u_i' u_j' \rangle}{\partial x_j} \tag{A.16}$$

The RANS equations have a similar form to the Navier-Stokes equations. However a new term:$-\frac{\partial \langle u_i' u_j' \rangle}{\partial x_j}$ popped up on the right hand side of the momentum equations. We call this term: *Reynolds term* which is a symmetrical 3 dimensional tensor and it is the direct result of averaging the nonlinear term. After rewriting Equation (A.16) one arrives to the following form:

$$\rho \left(\frac{\partial \langle u_i \rangle}{\partial t} + \langle u_j \rangle \frac{\partial \langle u_i \rangle}{\partial x_j} \right) = -\frac{\partial}{\partial x_j} \left[\langle \sigma_{ij} \rangle + \tau_{ij}' \right] \tag{A.17}$$

in which:

$$\langle \sigma_{ij} \rangle = \underbrace{\langle p \rangle \delta_{ij}}_{\substack{\text{isotropic} \\ \text{part}}} - \underbrace{\rho \nu 2 \langle S_{ij} \rangle}_{\substack{\text{deviatoric} \\ \text{part}}} \tag{A.18}$$

is the mean molecular stress where:

$$\langle S_{ij} \rangle = \frac{1}{2}\left(\frac{\partial \langle u_i \rangle}{\partial x_j} + \frac{\partial \langle u_j \rangle}{\partial x_i}\right) \tag{A.19}$$

is the mean rate of strain and

$$\tau'_{ij} = \rho \langle u'_i u'_j \rangle \tag{A.20}$$

is the *Reynolds stress*. The interpretation of the Reynolds stress is that turbulent fluctuations act on the mean flow as if they induce an additional stress. The RANS equations in their current form are not closed, since we have 4 equations and 10 unknowns (3 velocity components, pressure, 6 Reynolds stress components), thus a closure model is needed for the Reynolds stress. The most widely used closure models are based on the Boussinesq hypothesis.

Boussinesq hypothesis

The Boussinesq hypothesis assumes that similarly to the mean molecular stress tensor σ_{ij}, the turbulent stress tensor τ'_{ij} also could be divided into an isotropic and a deviatoric part. Furthermore, as the deviatoric part of $\langle \sigma_{ij} \rangle$ is connected to the mean rate of strain $\langle S_{ij} \rangle$ through the molecular viscosity ν as the result of the constitutive equation, the deviatoric part of τ'_{ij} could be connected to the rate of strain of the mean flow field $\langle S_{ij} \rangle$ via an artificial *eddy-viscosity* ν_t. For introducing the Bousinnesq hypothesis, first let us define the turbulent kinetic energy, which is half the trace of τ'_{ij}:

$$k \equiv \frac{1}{2}\tau'_{ii} = \frac{1}{2}\langle u'^2 \rangle + \frac{1}{2}\langle v'^2 \rangle + \frac{1}{2}\langle w'^2 \rangle \tag{A.21}$$

With k we can decompose τ'_{ij}:

$$\tau'_{ij} = \underbrace{\frac{2}{3}\rho k \delta_{ij}}_{\substack{\text{isotropic part} \\ \text{(Turbulent pressure)}}} + \underbrace{\left(\tau'_{ij} - \frac{2}{3}\rho k \delta_{ij}\right)}_{\substack{\text{deviatoric part} \\ \text{(Turbulent shear stress)}}} \tag{A.22}$$

The *Turbulent pressure* in Equation (A.22) usually is not modelled, rather it is added to the mean pressure term in Equation (A.17) and the overall pressure is calculated. Nonetheless, for the *Turbulent shear stress* a closure model is set up, which is the *Boussinesq hypothesis*:

$$\tau'_{ij} - \frac{2}{3}\rho k \delta_{ij} = -\rho \nu_t 2 \langle S_{ij} \rangle \tag{A.23}$$

in which: ν_t is the eddy-viscosity.

Thus, one can see that according to the Boussinesq hypothesis the additional stress originates from advective transport of mean momentum by turbulence fluctuations. Finally, after substitution of Equation (A.23) into Equation (A.22) one can write:

$$\tau'_{ij} = \frac{2}{3}\rho k \delta_{ij} - \rho \nu_t 2 \langle S_{ij} \rangle \tag{A.24}$$

Equation (A.24) is often referred to as *Boussinesq approximation* in literature.

Let us have a closer look at the Boussinesq approximation. It is evident that with defining ν_t the RANS equations are closed, therefore models which use this approximation are called *Eddy-viscosity models.* The main advantage of these models is the simplicity. Nevertheless, we need to reveal the biggest drawback of the Boussinesq approximation: the approximation is inherently wrong, since it assumes that turbulence is isotropic in the flow. We have already seen the isotropy of the flow only holds at the Kolmogorov scales, however in RANS models all of the turbulence is modelled, thus the strongly anisotropic energy containing range is calculated according to isotropy too. In spite of this drawback, eddy-viscosity models perform very well for various flows, especially when the turbulence is local. Also what we loose in accuracy with modelling all of the turbulence, we gain back in computation time, since RANS models can be ran on relatively coarse grids. As such, they are widely used in industrial applications.

Scaling of eddy-viscosity in RANS models

The dimension of the eddy-viscosity is the same as the molecular viscosity's i.e $[\nu_t] = [\nu] = [m^2/s]$, hence ν_t should scale with a product of a velocity and length scale. Large fluctuations belong to the energy containing range, thus eddy-viscosity should scale with the mixing length and velocity of the energy containing range:

$$\nu_t \sim u_0 l_0 \tag{A.25}$$

Consequently, to define ν_t one should first find the mixing velocity: u_0 and the mixing length: l_0 of the large eddies and this is the subject of the *Two-equation eddy-viscosity turbulence models.*

Two-equation eddy-viscosity turbulence models

The first two equation model was the $k - \epsilon$ model introduced by Jones & Launder in 1972, the other very popular model is the $k - \omega$ by Wilcox in 1993. Here ω denotes the frequency of the turbulent eddies: $\omega \equiv \epsilon/k$ Nowadays, in any industrial package many varieties of these two basic models can be found. Moreover, new models keep turning up, increasing the accuracy or just simply customising the basic models for a certain type of flow.

The models are based on the proportionality between the turbulence kinetic energy and the mixing velocity, as well as between the viscous dissipation and the mixing length:

$$u_0 \sim \sqrt{k} \tag{A.26}$$

$$l_0 \sim \frac{u_0^3}{\epsilon} \sim \frac{k^{3/2}}{\epsilon} = \frac{k^{1/2}}{\omega} \tag{A.27}$$

Transport equations can be derived for k and ϵ or for k and ω. The solver then simultaneously solves the 2 equations and obtains an eddy-viscosity through a constant for every iteration step:

- ν_t for $k-\epsilon$:

$$\nu_t = C_\mu \frac{k^2}{\epsilon} \tag{A.28}$$

- ν_t for $k-\omega$:

$$\nu_t = C_\omega \frac{k}{\omega} \tag{A.29}$$

where C_μ and C_ω are model constants.

Here we only present the transport equations of the standard $k-\epsilon$ model, since in the thesis we refer to them.

- for k:

$$\frac{\langle D \rangle k}{Dt} = P_k + \frac{\partial}{\partial x_j}\left[\left(\nu + \frac{\nu_t}{\sigma_k}\right)\frac{\partial k}{\partial x_j}\right] - \epsilon \tag{A.30}$$

in which:

$$P_k = -\rho \langle u_i' u_j' \rangle \frac{\partial \langle u_i \rangle}{\partial x_j} = -\tau_{ij}' \frac{\partial \langle u_i \rangle}{\partial x_j} \tag{A.31}$$

in concern with the Boussinesq hypothesis:

$$P_k = 2\nu_t \langle S_{ij} \rangle \langle S_{ij} \rangle \tag{A.32}$$

- for ϵ:

$$\frac{\langle D \rangle \epsilon}{Dt} = C_{\epsilon 1} \frac{\epsilon}{k} P_k + \frac{\partial}{\partial x_j}\left[\left(\nu + \frac{\nu_t}{\sigma_\epsilon}\right)\frac{\partial \epsilon}{\partial x_j}\right] - C_{\epsilon 2}\frac{\epsilon^2}{k} \tag{A.33}$$

In Equation (A.30) and in Equation (A.33) σ_k, σ_ϵ, $C_{\epsilon 1}$ and $C_{\epsilon 2}$ are model constants which have been tuned to a variety of flows.

A.3.2. Boundary layer

In this section we suppose that the boundary layer is 2 dimensional (the extension in the z direction is 0 and the free stream flows in the x direction) and it is of *zero gradient boundary layer* type, which means that the pressure only varies in the horizontal direction.

Eddy-viscosity models in their current form: Equation (A.28) and Equation (A.29) cease to be valid in the boundary layer. The presence of the wall has a double effect on the flow:

- Eddies very close to the wall cannot have a size that scales with the main flow because they are blocked by the wall
- Eddies very close to the wall cannot have a velocity that scales with the main flow because they are slowed down by the wall

As a result of these assumptions, we need to define new velocity and length scales in the boundary layer. It was found that the variation of the flow along the wall is negligible comparing with the variation in the wall normal direction. Thus, if the mean flow flows over a flat horizontal plate, the *total shear stress* reduces:

$$\tau = \underbrace{-\rho\nu\frac{\partial\langle u\rangle}{\partial y}}_{\substack{\text{viscous shear}\\ \text{stress: } \sigma_\nu}} + \underbrace{\rho\langle u'v'\rangle}_{\substack{\text{turbulent}\\ \text{stress: } \tau'}} \tag{A.34}$$

Due to the no-slip and no-penetration boundary conditions, the *turbulent stress* in Equation (A.34) disappears at the wall, hence the *wall shear stress* becomes:

$$\tau_w \equiv -\tau(0) = \rho\nu\frac{\partial\langle u\rangle}{\partial y}\bigg|_{y=0} \tag{A.35}$$

Viscous scales

It is obvious that in the near wall region the viscosity and the wall shear stress are important parameters. Therefore the length and velocity scales of this region are connected to these parameters and they are defined as:

- *friction velocity:*

$$u_\tau \equiv \sqrt{\frac{\tau_w}{\rho}} \tag{A.36}$$

- *viscous length scale:*

$$\delta_\nu \equiv \frac{\nu}{u_\tau} \tag{A.37}$$

With the help of these scales we define two dimensionless quantities, namely:

– *dimensionless velocity:*

$$u^+ \equiv \frac{\langle u \rangle}{u_\tau} \tag{A.38}$$

– *wall unit:*

$$y^+ \equiv \frac{y}{\delta_\nu} = \frac{u_\tau y}{\nu} \tag{A.39}$$

Regions in the boundary layer

One can notice that y^+ is similar to a local Reynolds number, so it is expected that when y^+ is small (close to the wall) the viscous stress whilst for large y^+ (remote from the wall, but still in the boundary layer) the turbulent stress will govern the flow. Figure shows the fraction of the turbulent and viscous stress normalized by total shear stress in the near wall area:

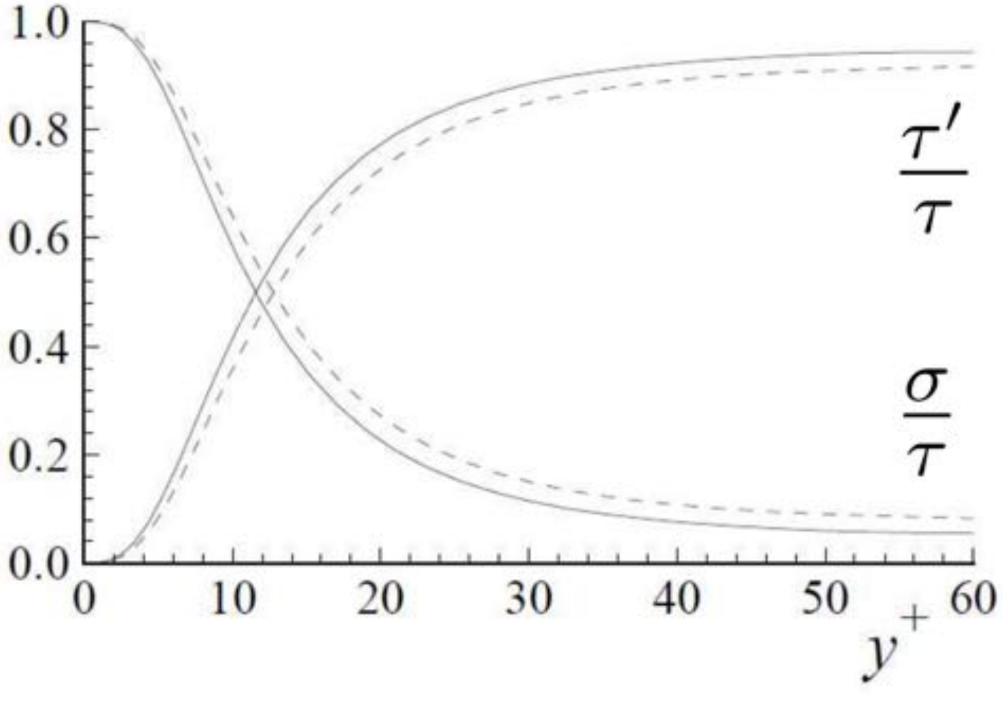

Figure A.4.: Profiles of the fractional contributions of the turbulent stress and viscous shear stress to the total stress. DNS data of Kim et al. [30]: dashed lines, Re = 5600; solid lines, Re = 13750.

We should note that Figure A.4 shows a result for a plane channel flow. The behaviour of the flow is not exactly the same in a plane channel and in the case of a boundary layer flow, however it is very similar. A plot about the contribution of the stresses would give almost identical results for a boundary layer. According to the DNS data of Kim et al. [30] depicted in Figure A.4, very close to the wall the viscous shear stress gives the whole contribution to the total shear stress. Moving further from the wall, the turbulent stress grows rapidly and the two stresses become equal at $y^+ \approx 12$. After this the turbulent stress slowly but surely overtakes the dominance. Finally, for $y^+ > 50$ the viscous shear stress is negligible since its contribution drops below 10 %. Consequently, the near-wall flow can be divided into two distinct regions:

- $y^+ < 50$: *viscous wall region*,
- $y^+ > 50$: *outer region*,

In the viscous wall region for $y^+ < 5$ the effect of turbulence stress disappears, thus this subregion is called: *viscous sublayer*.

Another division of the boundary layer exists which has mathematical considerations and it is used to determine the dimensionless velocity profiles as functions of wall unit. According to this the boundary layer comprises of:

- $y < 0.1\delta_x$: *inner layer*: the mean velocity profile is determined by the viscous scales and by the distance to the wall: y. The velocity profile is independent of the free stream velocity: U_0 and the boundary layer thickness: δ_x
- $y^+ > 50$: *outer layer*[1]: the mean velocity profile is independent of δ_ν but it is dependent on: U_0, δ_x, y and u_τ

In concern with these considerations one can write:

$$\frac{\partial \langle u \rangle}{\partial y} = f(\nu, u_\tau, \delta_x, y) \tag{A.40}$$

for the mean velocity gradient in the boundary layer. In Equation (A.40) we have 5 variables and 2 dimensions (length, time). Hence, according to the Buckingham Π theorem, the dependence of the variables can be written by 3 dimensionless group:

$$\frac{y}{u_\tau} \frac{\partial \langle u \rangle}{\partial y} = \Phi\left(\frac{y}{\delta_\nu}, \frac{y}{\delta_x} \right) \tag{A.41}$$

Law of the wall

As it was stated before in the inner layer the mean velocity profile depends only on : u_τ, y and δ_ν. As a consequence, Equation (A.41) reduces to:

$$\frac{y}{u_\tau} \frac{\partial \langle u \rangle}{\partial y} = \Phi_I\left(\frac{y}{\delta_\nu} \right) \tag{A.42}$$

Or equivalently:

---

[1] The *outer region* and the *outer layer* are equivalent. Their different names just stand for distinguishing the way how they have been defined.

$$\frac{\partial u^+}{\partial y^+} = \frac{1}{y^+}\Phi_I\Big(y^+\Big) \tag{A.43}$$

After integration one can write:

$$u^+ = f_w\Big(y^+\Big) \tag{A.44}$$

In which:

$$f_w\Big(y^+\Big) = \int\limits_0^{y^+} \frac{1}{\widetilde{y}}\Phi_I(\widetilde{y})d\widetilde{y} \tag{A.45}$$

Equation (A.44) is known as the *law of the wall.* The most important outcome of the law of the wall is that in the near-wall region u^+ solely depends on y^+. After having a closer look at the law we will see that the behaviour of $f_w(y^+)$ is different in very close to the wall (in the viscous sublayer) and remote from the wall.

The viscous sublayer

The boundary conditions for $f_w(y^+)$ at the wall: $f_w(0) = 0$ and $f'_w(0) = 1$. The Dirichlet type of boundary condition is due to no slip at wall ($u^+ = 0$), whilst the Neumann type is obtained by normalizing Equation (A.35) with the viscous scales $\left(\frac{\partial u^+}{\partial y^+}\Big|_{y^+=0} = 1\right)$. One can write the Taylor expansion for $f_w(y^+)$ for small y^+:

$$f_w(y^+) = f_w(0) + f'_w(0)y^+ + H.O.T. = y^+ \tag{A.46}$$

which yields:

$$u^+ = y^+ \tag{A.47}$$

in the near wall region. Experimental results, like the one which is depicted in Figure A.5, have revealed that the linear relation in Equation (A.47) holds in the whole viscous sublayer, so until $y^+ < 5$. The other region of the inner layer will be introduced later.

Velocity-defect law

Contrary to the inner layer, in the outer layer the effect of viscosity is negligible, so that Equation (A.41) becomes:

$$\frac{y}{u_\tau}\frac{\partial \langle u \rangle}{\partial y} = \Phi_O\left(\frac{y}{\delta_x}\right) \tag{A.48}$$

or equivalently:

$$\frac{\partial(\langle u\rangle/u_{\tau})}{\partial(y/\delta_x)} = \frac{1}{(y/\delta_x)}\Phi_O\left(\frac{y}{\delta_x}\right) \tag{A.49}$$

After integrating Equation (A.49), one arrives to the *velocity-defect law*:

$$\frac{U_0 - \langle u\rangle}{u_{\tau}} = F_D\left(\frac{y}{\delta_x}\right) \tag{A.50}$$

where:

$$F_D\left(\frac{y}{\delta_x}\right) = \int\limits_{y/\delta_x}^{1} \frac{1}{\widetilde{y}}\Phi_O(\widetilde{y})d\widetilde{y} \tag{A.51}$$

Overlap region

According to the definitions of the inner and outer layer for $50 < y^+ < 0.1\delta_x/\delta_\nu$ we have an *overlap region*. Consequently, the overlap region comprises of the outer region of the inner layer and the inner region of the outer layer. The general consideration is that in this region the flow is sufficiently remote from the wall for neglecting the effect of viscosity and similarly it is enough far from the end of the boundary layer, so the dependency of δ_x is still not important. This yields that the Φ functions on the right hand side of Equation (A.42) and Equation (A.48) can be represented by a single constant:

$$\Phi_I\left(y^+\right) = \Phi_O\left(\frac{y}{\delta_x}\right) = \frac{1}{\kappa} \qquad \text{in the overlap region} \tag{A.52}$$

in which:

$$\kappa = 0.41 \tag{A.53}$$

is the Von Kármán constant. After substitution of Equation (A.52) into Equation (A.43) one gets:

$$\frac{\partial u^+}{\partial y^+} = \frac{1}{\kappa}\frac{1}{y^+} \tag{A.54}$$

Equation (A.54) integrates to:

$$u^+ = \frac{1}{\kappa}\ln\left(y^+\right) + B \qquad \text{log law for inner layer} \tag{A.55}$$

Where B is a constant. In literature there is some variation for the exact value of B. In general, we can say $B \approx 5.2$. Now let us substitute Equation (A.52) into Equation (A.49) so that we arrive to:

$$\frac{\partial(\langle u\rangle/u_\tau)}{\partial(y/\delta_x)} = \frac{1}{\kappa}\frac{1}{(y/\delta_x)} \tag{A.56}$$

Which integrates to:

$$\frac{U_0 - \langle u\rangle}{u_\tau} = -\frac{1}{\kappa}\ln\left(\frac{y}{\delta_x}\right) + B_1 \qquad \text{log law for outer layer} \tag{A.57}$$

Depending on the nature of the flow: $B_1 \approx 0.2..0.7$. Both Equation (A.55) and Equation (A.57) are known as the *log(arithmic) law.* If one adds the log law formulation for the inner (Equation (A.55)) and for the outer layer (Equation (A.57)) together *the friction law* is obtained which provides a solution for u_τ:

$$\frac{U_0}{u_\tau} = \frac{1}{\kappa}\ln\left(\frac{\delta_\nu}{\delta_x}\right) + B + B_1 \tag{A.58}$$

Although the overlap region is confined to $50 < y^+ < 0.1\delta_x/\delta_\nu$ it was found that the log law is valid for: $30 \lesssim y^+ \lesssim 0.2\delta_x/\delta_\nu$

Velocity-defect law reconsidered

The log law describes the inner region of the outer layer until $y/\delta_x \approx 0.2$. However, for $y/\delta_x \gtrsim 0.2$ the mean velocity gradients deviates from the log law. In turbulence we refer to this discrepancy as: *wake contribution.* Cole [26] provides a formula which incorporates the wake effect, thus the velocity defect law can be written through the whole outer layer:

$$\underbrace{\frac{U_0 - \langle u\rangle}{u_\tau} = F_D\left(\frac{y}{\delta_x}\right)}_{\text{velocity-defect law}} = \underbrace{-\frac{1}{\kappa}\ln\left(\frac{y}{\delta_x}\right) + B_1}_{\text{log law for outer layer}} \underbrace{-\frac{\Pi}{\kappa}\mathrm{w}\left(\frac{y}{\delta_x}\right)}_{\text{law of the wake}} \tag{A.59}$$

in which:

$$\Pi = \frac{\kappa B_1}{\mathrm{w}(1)} \tag{A.60}$$

In Equation (A.59) w is the *wake function* and Π is the *wake strength parameter (Coles parameter).* The wake strength parameter is flow dependent, whereas for the wake function the commonly used approximation:

$$\mathrm{w}\left(\frac{y}{\delta_x}\right) = 2\sin^2\mathrm{w}\left(\frac{\pi}{2}\frac{y}{\delta_x}\right) \tag{A.61}$$

Buffer layer

So far in the boundary layer we have tracked all but the region: $5 < y^+ < 30$. This is the buffer region and it got its name because this is the transition region between the laminar and the turbulent region. It is known that the production of turbulent kinetic energy peaks at this region, thus it is essential to capture this region accurately. To determine the mean velocity profile in the buffer layer in Pope [23] an empirical guess provided by Van-Driest is given which is not written here in details for brevity. The base of the Van-Driest method is to create a smoothing function for the mean velocity from the velocity profiles in the viscous sublayer as well as from the log-layer. At the lower limit ($y^+ = 5$) the influence of the log-layer disappears, oppositely at $y^+ = 30$ the mean velocity is defined by the log-law. Commercial packages also uses smoothing functions for the buffer layer. The nature of the smoothing function is defined differently in every package.

Figure A.5 compares the solution obtained from the described laws with experimental results. One can see that in each region the laws are capable to give a very accurate approximation for the mean-velocity.

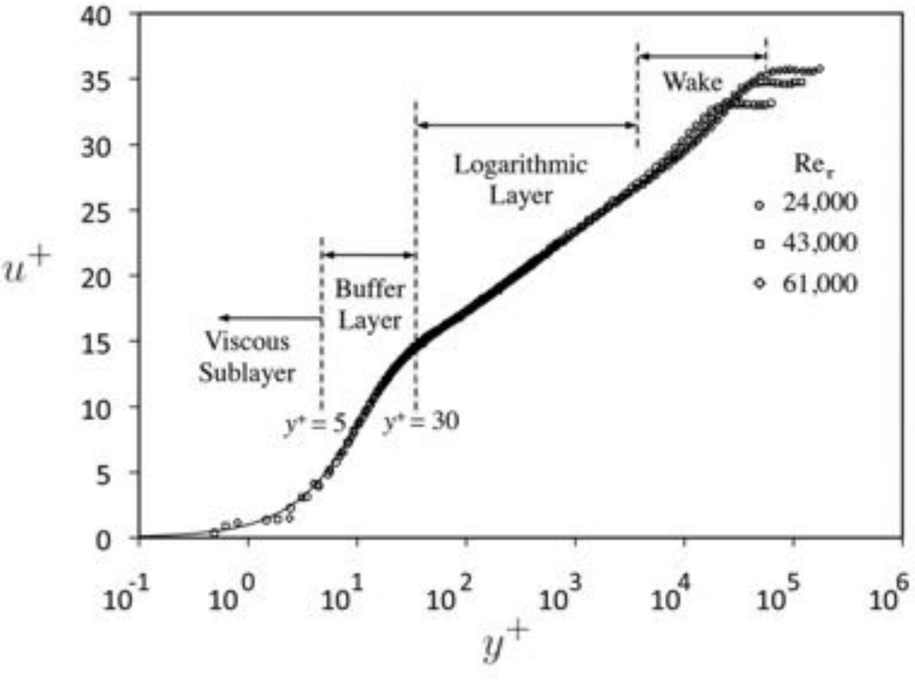

Figure A.5.: Mean velocity profile of a smooth-flat-plate turbulent boundary layer plotted in log-linear coordinates with viscous scales normalizations. Taken from: Perlin et al. [31]

Finally let us give a summary of the position of the different layers and regions which were mentioned in this section:

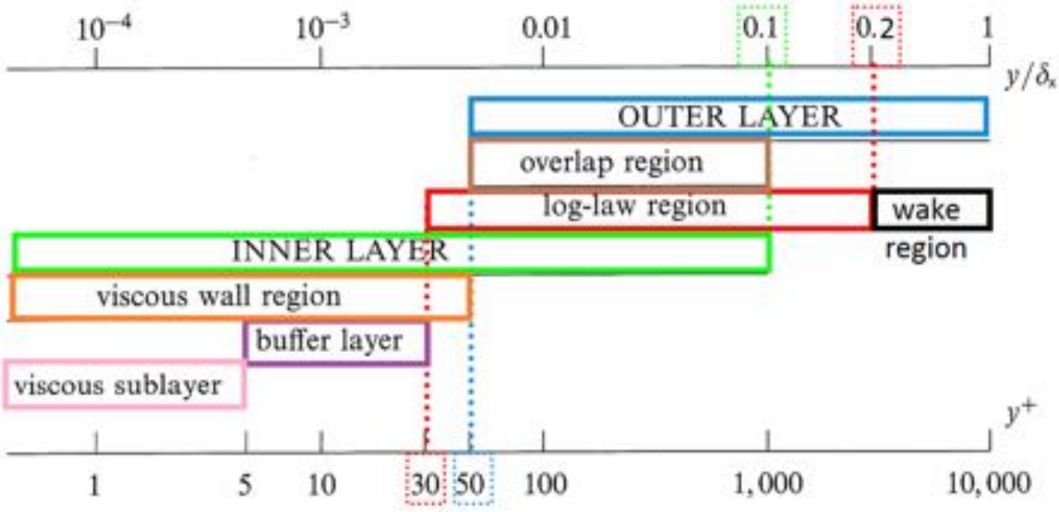
10^{-4}
10^{-3}
0.01
0.1
0.2
1
y/δ_x
OUTER LAYER
overlap region
log-law region
wake region
INNER LAYER
viscous wall region
buffer layer
viscous sublayer
y^+
1
5
10
30
50
100
1,000
10,000

Figure A.6.: Different layers and regions in a turbulent boundary layer

Eddy-viscosity in different layers

Similarly to the core of the flow eddy-viscosity should scale with the velocity and the length scale of the local large eddies. According to Figure A.6 the boundary layer can be divided to a viscous wall region, a log-law region and a wake region. We focus here our discussion on the overlap region.

Turbulent boundary layer and plane channel flow are identical all but in the wake region, hence for determining the turbulent viscosity in the log-law region one can again rely on plane channel flow results in Figure A.7. In this flow the log-layer is demarcated as: $50 < y^+ < 120$.

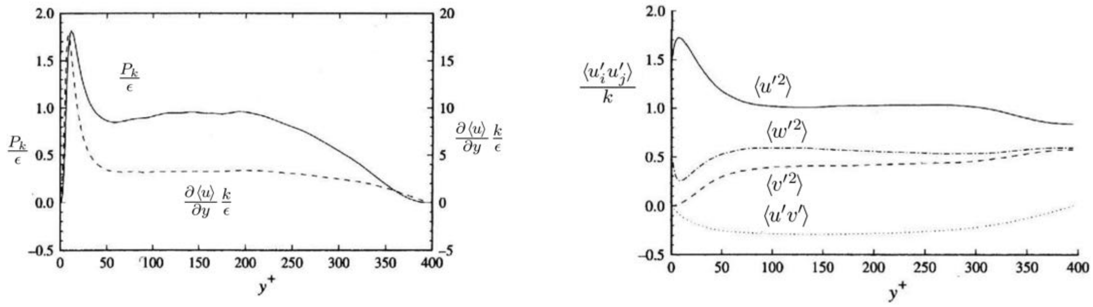

(a) Profiles of ratio of dissipation to production $\frac{P_k}{\epsilon}$ and normalized mean shear rate $\frac{\partial\langle u\rangle}{\partial y}\frac{k}{\epsilon}$

(b) Profiles of kinematic Reynolds stresses $\langle u_i'u_j'\rangle$ normalized by the turbulent kinetic energy

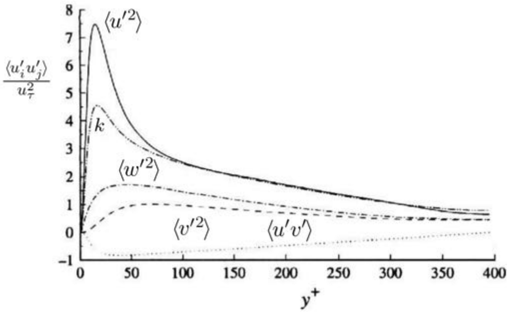

(c) Profiles of kinematic Reynolds stresses and turbulent kinetic energy normalized by wall friction velocity

Figure A.7.: Profiles of DNS of channel flow at Re = 13750. Results are obtained from Kim et al. [30]

With the help of the law of the wall as well as according to Figure A.7 one can write the three fundamental properties of the log-layer:

- the mean velocity gradient:

$$\frac{\partial u^+}{\partial y^+} = \frac{1}{\kappa}\frac{1}{y^+} \qquad \text{or} \qquad \frac{\partial\langle u\rangle}{\partial y} = \frac{1}{\kappa}\frac{u_\tau}{y} \tag{A.62}$$

- the local balance of production and dissipation:

$$P_k \approx \epsilon \tag{A.63}$$

- the local constancy of the normalized kinematic Reynolds stress:

$$\frac{\langle u'v'\rangle}{k} \approx -0.3 \qquad \text{or} \qquad \frac{\langle u'v'\rangle}{u_\tau^2} \approx -1 \tag{A.64}$$

For expressing the turbulent viscosity in the log-layer we use the local length (mixing-length: l_m) and velocity scales (mixing-velocity: u_*) as:

$$\nu_t = u_* l_m \tag{A.65}$$

Let us implicitly define the mixing-velocity:

$$u_* = |\langle u'v' \rangle|^{1/2} \tag{A.66}$$

After substitution of Equation (A.66) into Equation (A.65) together with the use of the Boussinesq hypothesis for the boundary layer ($\langle u'v' \rangle = \nu_t(\partial \langle u \rangle / \partial y)$) and the first property ($(\partial \langle u \rangle / \partial y) = u_\tau / (\kappa y)$) one arrives to:

$$\nu_t = l_m^2 \frac{1}{\kappa} \frac{u_\tau}{y} \tag{A.67}$$

According to the third property $|\langle u'v' \rangle| \approx u_\tau^2$. With the help of this consideration, in the log-layer:

- the velocity scale of the large eddies: u_τ
- the mixing length of the large eddies: $l_m = \kappa y$ which is known as: *Prandtl's mixing length hypothesis*. The most important result of Prandtl's mixing-length hypothesis is that eddies scales linearly with the distance to the wall. With this result it is just a matter of algebra to deduce that $\frac{\partial \langle u \rangle}{\partial y}$, $P_k = -\rho \langle u'v' \rangle \frac{\partial \langle u \rangle}{\partial y}$ and ϵ vary inversely, whilst the turbulent time scale $\tau = \frac{k}{\epsilon}$ varies linearly with y in the log-layer.

Finally we can write:

$$\nu_t = u_* l_m = l_m^2 \left| \frac{\partial \langle u \rangle}{\partial y} \right| = u_\tau \kappa y \tag{A.68}$$

for the turbulent viscosity in the log-layer.
The mixing length hypothesis is usually embedded into the standard wall functions' formulation in each solver, however the way how the other two regions are handled is different from package to package. Furthermore, only the mixing length in the log-layer has fundamental outcomes, thus the mixing lengths for the remaining regions are not introduced here in details . Nonetheless, it is worth to note that the mixing lengths are less than $l_m = \kappa y$ in both the viscous wall region and in the wake region.

Implementation in FLUENT

In the beginning of this section we shall mention that the $k - \omega$ model explicitly incorporates the near-wall treatment, thus the below decribed methods are only applicable for the $k - \epsilon$ model.

In FLUENT two fundamental methods exist to handle the boundary layer: "wall functions" and "near-wall modelling". In the standard $k - \epsilon$ model both methods use Equation (A.28) in the outer layer, however the viscosity affected inner layer is treated differently. In case of "wall functions" approach the viscous wall region is not resolved. To bridge the viscous wall region between the wall and the fully-turbulent outer layer semi-empirical "wall functions" are used. "Near-wall modelling" uses modified turbulence models in the vicinity of the wall, hence it is capable of resolving the viscous wall region too. Figure A.8 sums up the main difference between the two approaches:

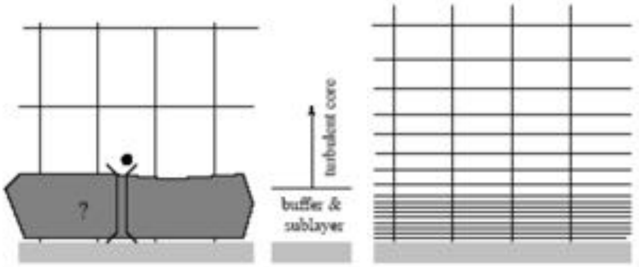

(a) Wall functions modelling (b) Near-wall modelling

Figure A.8.: Boundary layer modelling in FLUENT. Taken from: FLUENT User's Guide 12.10.1 [22]

Standard wall functions modelling method belongs to the "wall function" approach. It uses either the linear relation between u^+ and y^+ or if the node is outside the viscous sublayer the log-law employed. Since, nodes that are placed to the buffer layer are treated as they would be in the log-layer, it is highly recommended to not to put nodes there. In concern with the above mentioned wall laws, the mean velocity can be calculated. The friction velocity, u_τ can be obtained for instance from a node which is placed in the log-layer according to Equation (A.58). However, we should take into consideration that in a general CFD simulation neither the boundary layer thickness nor U_0 are known priory. Nonetheless, these quantities are functions of each other, thus they can be solved iteratively. The "k": Equation (A.30) is solved till the wall. The boundary conditions for k at the wall: $k = 0$ and $\partial k/\partial n = 0$ respectively. The derivative to the normal direction of the surface is only zero exactly at the wall, and hence moving more remote from the wall the production term G_k starts growing. FLUENT calculates the value of G_k in the wall adjacent cells on the basis of the local equilibrium hypothesis so that it assumes that these points are in the log-layer. The transport equation for ϵ is not solved, instead ϵ is calculated likewise assuming local balance of production and dissipation. Standard wall functions are widely used in the industry since they are robust and cheap. Nonetheless, the "wall function" approach ceases to be valid when the flow departs too much from the ideal case. In our simulation due to the fast rotation in the vicinity of the cylinders a strong body force is applied on the flow. As such, standard wall functions only could have been used with caution and it was wiser to fully resolve the boundary layer even though this made the computation more expensive.

Due to the limitations of standard wall function in FLUENT, a more elaborate treatment is also available. This is the *enhanced wall treatment*, which can also properly handle the nodes that are placed in the buffer layer. This treatment comprises of two sub-methods: *two-layer model* and *enhanced wall functions*. Depending on the resolution of the mesh FLUENT switches between the two sub-methods.

The *two-layer model* is used in case of finer meshes, where the mesh is fine enough to be

able to resolve the laminar sublayer (typically $y^+ \approx 1$). This model can again be subdivided into a viscosity-affected region and a fully-turbulent region. The categorization of the nodes in the boundary layer are carried out according to the local turbulent Reynolds number ($Re_y = y\sqrt{k}/\nu$). As it was mentioned before the standard model is used in the fully turbulent region. In the region very close to the wall the one-equation model of Wolfstein is applied. This one-equation model solves transport equations for the "momentum" and "k" according to Equation (A.16) and Equation (A.30). Nonetheless, transport equation is not solved for ϵ, it is instead calculated from "k". Furthermore, the most important thing is that eddy-viscosity is calculated differently from Equation (A.28). In the rest of the viscous affected region a blending function is applied which combines the two eddy-viscosity such that close to the wall the eddy-viscosity will be identical with the result from the Wolfstein model, while close to the outer layer eddy-viscosity approaches the standard model and in the region between a smooth transition is produced.
If the mesh is not fine enough to be able to fully resolve the viscous sublayer, but it is fine enough to contain points in the buffer layer *enhanced wall functions* are used for determining the velocity profiles in the boundary layer. Since this method is also a wall function method, similarly to the standard wall functions only the transport equation for "k" is solved until the wall, the mean velocity and ϵ are calculated. The boundary conditions for "k" are the same as in the standard wall function case. Nevertheless, G_k in the near-wall region is computed using the obtained velocity gradients from the wall functions. In the buffer layer the procedure is the same which was written in the previous section : the buffer layer is calculated via a smoothing function which combines the results from the viscous sublayer as well as from the log-law. Furthermore, enhanced wall functions are slightly different from the standard ones.

The goal of this section was to give a general overview of the applied wall functions for RANS calculations. The exact description of the above mentioned methods can be found in FLUENT User's Guide 12.10 [22]

Reynolds stress model (RSM)

So far we introduced the eddy-viscosity models which are based on the Boussinesq hypothesis. Another (and possibly more straightforward) solution for the closure is to derive and solve transport equations for each component of the Reynold stress. The main benefit of this model is its capability of accounting for anisotrophy. Nonetheless, many times the biggest part of error comes from the fact that the whole turbulence is modelled. As such, the additional cost involved in RSM (+2 equations in 2D or +5 equations in 3D comparing with eddy-viscosity models) does not always pay off in better accuracy. In the present problem the strong recirculation area in the wake of the cylinder definitely makes the turbulence non-local, therefore a superiority is expected from this model.

A.3.3. Large Eddy Simulation

In Large Eddy Simulation filtering operators are applied on the Navier-Stokes Equations (A.1)–(A.2). As a result of the filtering process, the large scales (eddies) are directly calculated while the residual motions (in the so-called subgrid-scales) are modelled. In a perfectly resolved LES these subgrid-scales lie in the universal equilibrium range (see in Figure A.1). Unlike RANS, LES simulations cannot be carried out effectively on 2D grids. Turbulent eddies are fundamentally known to be 3 dimensional, and since in LES we directly calculate the large eddies a 3D computational domain is inevitable. The main rationales in directly calculating the large eddies are:

- By far the biggest fraction of the turbulent kinetic energy is stored in the large fluctuations. Furthermore, momentum, mass and other passive scalars are transported mostly by large eddies as well.
- Large eddies are anisotropic. The boundary conditions as well as the geometry mainly influence the large eddies.
- Contrary, small eddies are more isotropic and hence, turbulence models that assume isotropy (like the eddy-viscosity models) can model them effectively.

Due to these considerations one can expect that LES is superior to RANS when large unsteadiness plays an important role in the flow, such as for flow over bluff bodies (where vortex shedding and unsteady separation appear), so also in the present problem. RANS and LES, as it will be shown later are very similar in many senses. This is not surprising since averaging is also a filtering process. Hence RANS can be regarded as the upper limit of LES where the filter is that wide to only be capable of resolving the fluctuations of the mean flow and the residual fluctuations i.e. the whole turbulence resides in the subgrid model. Therefore, the derivation of the LES or RANS model equations have exactly the same analogy. Due to the similarities, RANS knowledge comes in very handy in the explanation of LES. We will also refer back to the RANS section and make comparisons between the two models. Nevertheless, one should always keep in mind that despite the similarities, RANS is just a special case of filtering and consequently LES is a more general model, this fact will yield substantial differences between the two models.

Required resolution for LES

The easiest way to imagine the LES calculation is if we apply the filtering operator to a real signal e.g. to an experimental or to a DNS result. To further simplify the problem this time we only take the horizontal component of the velocity field. In Figure A.9 such a velocity component together with its filtered and residual part is depicted:

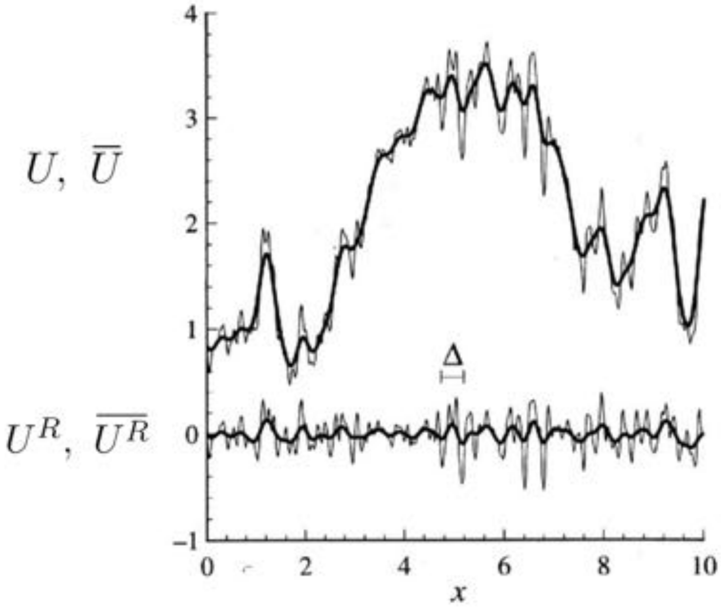

Figure A.9.: Upper curves: a sample of the horizontal component of the velocity field $U(x)$ together with its filtered field $\overline{U}(x)$ (bold line), residual field $U^R(x)$ and the filtered field of the residual field $\overline{U^R}(x)$ (bold line). Taken from Pope [23]

In the LES procedure as we mentioned before the filtered part of the velocity component is directly calculated taking into account the effect of the residual part through a turbulence model. As such if one defines LES as a physical process, a filter with filter width $\triangle$ should be sought which in the wave number space of the solution effectively annihilates all Fourier-modes whose wave numbers are greater than the cut off wave number and in the same time it has no effect of the lower wave number modes. Subsequently, the obtained filtered equations can be solved numerically on a grid with spacing h. This procedure simplifies further if we consider LES as a numerical method, which is the subject of computational fluid dynamics. In this case finite volume discretization already incorporates the filtering procedure which means: $\triangle = h$. Or in other words the finer the mesh the larger the number of the resolved eddies is and the less fraction will be modelled. Then, the trivial question rises: how fine should the resolution be of the computational mesh?

Before answering this very important question it is wise to clarify the main goal of an LES. The main purpose of an LES simulation is to achieve statistical equality between the real and the filtered flow field. We will demonstrate this with an example for the velocity field Let us apply the filtering operator to a real flow field such as shown in Figure A.9:

$$U_i = \underbrace{\overline{U_i}}_{\substack{\text{filtered}\\ \text{part}}} + \underbrace{U_i^R}_{\substack{\text{residual}\\ \text{part}}} \tag{A.69}$$

One can apply a statistical operator to this field:

$$Q^{U_i} = \mathcal{Q}\{U_i\} \tag{A.70}$$

The aim of the LES is to apply a filter on the flow field which leads to statistical equality between the real and the filtered flow field:

$$Q^{U_i} = Q^{\overline{U_i}} \tag{A.71}$$

Therefore, $\triangle$ should be as small to be able to assure that the residual part only has negligible statistical influence. One can also notice that $\triangle$ is very dependent on the boundary conditions and flow type. A good example for the boundary condition: at the wall, comparing with the rest of the flow field "there are no large eddies" and hence, the mixing length is changed. The influence of the flow type could be easily understood through turbulent combustion, where the rate-controlling processes of molecular mixing and chemical reaction occur at the smallest scales. Obviously these examples require smaller $\triangle$ than a high Reynolds number free-shear flow where the information is mostly represented by the large scales. It is generally accepted that if at least 80 % of the turbulent kinetic energy resides in the filtered velocity components the two terms in Equation (A.71) tend to be equal.

Now let us assume that one defines a filter which ensures the equality in Equation (A.71). Next, we can apply a decomposition to the numerical model:

$$m_i = \underbrace{w_i}_{\substack{\text{resolved}\\ \text{part}}} + \underbrace{r_i}_{\substack{\text{residual}\\ \text{part}}} \tag{A.72}$$

in which:

m_i: is the numerical velocity field

w_i: is the resolved part of the numerical velocity field

r_i: is the residual part of the numerical velocity field

and we also apply the statistical operator:

$$Q^{m_i} = Q^{w_i} + Q^{r_i} \tag{A.73}$$

The main discrepancy between the physical and the numerical decomposition is that while in the physical LES the resolved part is perfect, in the numerical LES it is modelled. Consequently, the resolved field's statistics, Q^{w_i} depends on the filter, on the discretization scheme and on the model as well. We note here that $\overline{U_i}$ cannot be equal to w_i even if we assume that the residual part is perfectly modelled. This is the direct result of the fact that both $\overline{U_i}$ and w_i are random 3 dimensional fields so that their future evolution is not determined by their current state. In order to emphasize the difference, the experimental results are written with capital, whilst the calculated ones with lowercase letters. From the numerical LES point of view therefore the main goal is to use an appropriate spacing h on which the turbulence model as well as the discretization scheme are capable of operating with negligible error and can assure the statistical equality:

$$Q^{w_i} = Q^{\overline{U}_i} \tag{A.74}$$

Unambiguously, if the resolution is bad, i.e. h is too big a significant information will be in the residual part of the numerical model. Since (see later in the Smagorinsky model) the residual motions in LES are modelled much simpler than in the RANS case, a not fine enough grid resolution completely spoils the results and we can produce an LES calculation which is rather a poor RANS.
In real life no one is interested in the equality in Equation (A.75), instead we directly try to achieve:

$$Q^{U_i} = Q^{w_i} \tag{A.75}$$

which points out how the filtering and discretizing merge together: $\triangle = h$ in the numerical LES case. Nevertheless, this equality unfortunately cannot always be reached due to the previously mentioned strong dependency on the flow type. Figure A.10 illustrates Q^{m_i} and Q^{w_i}, Q^{r_i} in two different flows. The figures belong to unrealistically high Reynolds number, where the intermediate asymptote $Q_I^{m_i}$ in the inertial subrange is known to be present.

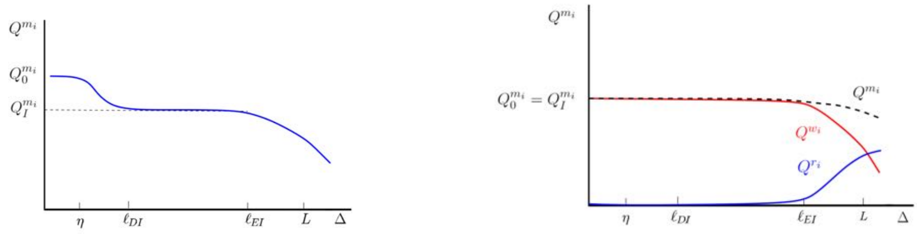

(a) Q^{m_i} as a function of $\triangle$ in a flow with controlling processes in the Kolmogorov scales. $Q_0^{m_i}$ indicates the statistics of the DNS solution

(b) Q^{w_i} and Q^{r_i} as a function of $\triangle$ in a flow without controlling processes in the Kolmogorov scales. $Q_0^{m_i}$ indicates the statistics of the DNS solution

Figure A.10.: LES statistics in two distinct flow types. Taken from: Pope 2004 [27]

One can see that in Figure A.10a (which roughly represents a turbulent combustion) the desired equality in Equation (A.75) is only achieved in the Kolmogorov scales, so the grid resolution should be in the order of DNS resolution. As a consequence, this flow type is not recommended for LES modelling. Contrary, in Figure A.10b (which loosely can be interpreted as a free-shear flow case) the contribution of Q^{r_i} disappears in the beginning of the inertial subrange, yielding statistical equality between the LES and the DNS field i.e.: $Q^{w_i} = Q^{m_i} = Q_I^{m_i} = Q_0^{m_i} = Q^{U_i}$. Or in other words: with only resolving the energy containing range we can calculate the statistics of DNS, this fact makes Large Eddy Simulation the most accurate turbulence model.

In Figure A.10 two extreme cases were depicted. Real flows are somewhere between these two examples. In terms of LES simulation it is desirable to approach the free-shear flow case so that to oppress the statistical influence of the residual part. To finally draw a conclusion, in a flow which is applicable for LES, it is deemed that if $h < l_{EI}$ then $Q^{m_i} \approx Q_0^{m_i} = Q^{U_i}$. In order that the residual statistics do not have a significant contribution i.e.: $Q^{w_i} \approx Q^{m_i} \approx$

$Q_I^{m_i} \approx Q_0^{m_i} = Q^{U_i}$ the 80-90% of the turbulent kinetic energy should be resolved. The amount of resolved kinetic energy is not known priory, moreover it changes with the flow in each iteration step. Nevertheless, it can be estimated after the simulation to get insight regarding the resolution.

Computational cost of LES

In computational cost LES falls between RANS and DNS. Comparing with DNS, the enormous computational cost arising from resolving the Kolmogorov scales is saved. To have an idea about the saving, Figure A.11 shows the solution domain in wavenumber space for a DNS calculation of isotropic turbulence:

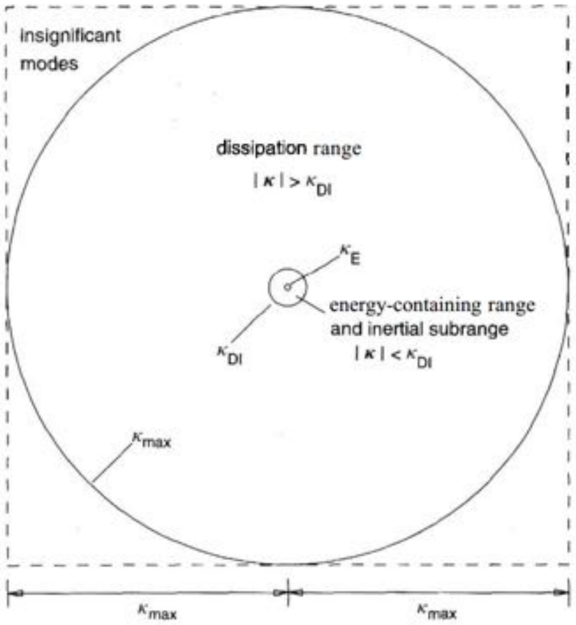

Figure A.11.: The solution domain in wavenumber space for a DNS of isotropic turbulence. Only 0.016% of the modes lie within the sphere of radius K_{DI}, representing motions in the energy-containing range and in the inertial subrange. Taken from Pope [23]

In consonance with Figure A.11 there are orders of magnitude difference between the cost of DNS and LES. On the other hand, unfortunately LES is orders of magnitude more expensive than RANS. The finer grid radically raises the computational cost. It is known that halving the spacing h increases the required memory and CPU time by factors of 8 and 16, respectively. Furthermore, according to Figure A.10 LES is extremely sensitive for the resolution: results from a too coarse grid are inferior to RANS results, on the contrary refinement in the inertial subrange does not contribute to better accuracy but higher prices! Apart from the higher resolution, in LES the flow field will be unsteady even if the mean flow does not change in time. Accordingly, to obtain accurate statistical results, LES should be ran for significantly longer time (i.e. more iteration steps are needed) than in RANS.

We have seen that LES could be feasible for higher Reynolds number than DNS, however in case of resolving all the energy containing range i.e. $h < l_{EI}$ the resolution scales with the Taylor microscale, the scale of the inertial subrange, see in Figure A.1. The ratio between the Taylor microscale and the Integral length scale is:

$$\frac{\lambda}{l_0} = \sqrt{10} Re^{-1/2} \tag{A.76}$$

which implies that the resolution should also scale with $\sqrt{10} Re^{-1/2}$. Moreover, in the near wall regions, due to the smaller scales of the local large eddies even finer resolution is needed: $h_{wall} << l_{EI}^{\text{main flow}}$. As mentioned before, computational cost scales with h^{-4}, hence with local refinements one can easily trigger a cost explosion. Consequently, keeping the resolved turbulent kinetic energy above 80% also in the near wall region is not feasible for very high Reynolds number and the use of wall functions (even if $y^+ \approx 1$!) are inevitable.

To sum up, LES might become one day the Holy Grail of CFD. Nevertheless, nowadays, accuracy still comes with a high price.

The filtered Navier-Stokes i.e. the LES equations

By analogy to the Reynolds decomposition, an arbitrary signal can be decomposed to a filtered and a residual part:

$$f = \bar{f} + f^R \tag{A.77}$$

The filtered Navier-Stokes equations read:

$$\frac{\partial \overline{u_i}}{\partial x_i} = 0 \tag{A.78}$$

$$\rho \left(\frac{\partial \overline{u_i}}{\partial t} + \overline{u_j} \frac{\partial \overline{u_i}}{\partial x_j} \right) = -\frac{\partial}{\partial x_j} \left[\overline{\sigma_{ij}} + \tau_{ij}^R \right] \tag{A.79}$$

in which:

$$\overline{\sigma_{ij}} = \bar{p} \delta_{ij} - \rho \nu 2 \overline{S_{ij}} \tag{A.80}$$

is the filtered molecular stress where:

$$\overline{S_{ij}} = \frac{1}{2} \left(\frac{\partial \overline{u_i}}{\partial x_j} + \frac{\partial \overline{u_j}}{\partial x_i} \right) \tag{A.81}$$

is the filtered rate of strain and

$$\tau_{ij}^{R} = \rho\Big(\overline{u_i u_j} - \overline{u_i}\,\overline{u_j}\Big) \tag{A.82}$$

is the *Reynolds stress of the residual motions.* We can see that the LES and RANS equations indeed have exactly the same form, nevertheless in the definition of τ_{ij}^{R} we can find a substantial difference, namely: the filtered residual field is not 0: $\overline{u_i^R} \neq 0$. We note here that the mean of the residual field is not 0 either: $\langle u_i^R \rangle \neq 0$. According to the equations a closure is needed here as well, this is the subject of the next section

Smagorinsky model

The Smagorinsky model was introduced by Smagorinsky in 1963 and it was generalised to its current form by Lilly in 1967. Although this model is deemed to be by far not the most accurate closure for LES, it is a base of many subsequently evolved LES model, hence its demonstration is mandatory. The Smagorinsky model is very similar to the RANS eddy-viscosity models in a sense that both use the Boussinesq hypothesis. However, unlike RANS eddy-viscosity models, the Smagorinsky model explicitly defines the length and velocity scales and hence transport equations are not needed.

Similarly to the RANS deduction, let us introduce the *residual kinetic energy*, which is the half of the trace of τ_{ij}^{R}:

$$k^{R} \equiv \frac{1}{2}\tau_{ii}^{R} \tag{A.83}$$

With the help of k^R the *anisotropic residual stress tensor*:

$$\tau_{ij}^{r} \equiv \tau_{ij}^{R} - \frac{2}{3}\rho k^{R}\delta_{ij} \tag{A.84}$$

Like in the RANS case the *isotropic residual stress* is not modelled, rather it is added to the filtered pressure $\bar{p}$. Finally, τ_{ij}^{r} is connected to the filtered velocity field via the Boussinesq hypothesis:

$$\tau_{ij}^{r} = -\rho\nu_r 2\overline{S_{ij}} \tag{A.85}$$

in which the eddy-viscosity of the residual motions is modelled by analogy to the mixing-length hypothesis (Equation (A.65):

$$\nu_r = l_S^2\overline{S} \tag{A.86}$$

where $\overline{S}$ is the *charactersitic filtered rate of strain*:

$$\overline{S} \equiv \Big(2\overline{S_{ij}}\,\overline{S_{ij}}\Big)^{1/2} \tag{A.87}$$

and l_S is the *Smagorinsky lengthscale* which is taken to be proportional to the filter width through the *Smagorinsky coefficient*, C_S:

$$l_S^2 = (C_S \triangle)^2 \tag{A.88}$$

In the *Standard Smagorinsky model* C_S is constant and according to Lilly [29] in high Reynolds number turbulent flows with a filter in the inertial subrange: $C_S = 0.17$. Keeping C_S to be constant everywhere in the flow yields that the standard model cannot distinguish the fundamentally different regions in the flow. For example, in the laminar region C_S should be 0 and because of the reduced turbulent scales in the near wall area, C_S must be decreased compared with its value in the core region. Another problem is that in real flows there can be local *backscatter* which is an inverse energy transfer process i.e the energy is transferred from the residual motions to the filtered motions. Obviously, this effect cannot be captured either by any eddy-viscosity or by a Smagorinsky model. Furthermore, in transitional flows as well as for homogeneous flows the Smagorinsky model is too dissipative, i.e. too much energy is transferred to the residual motions.

Despite its drawbacks the Smagorinsky model is widely used in industry, since it is cheap. Besides, we will see later that with a little modification its performance can be tuned in the boundary layer.

Implementation in FLUENT, the Smagorinsky-Lilly and the WALE model

Since in the standard model C_S is constant everywhere in the flow, in the log-layer it is inherently incapable of producing a wall distance dependent lengthscale and hence giving back the logarithmic velocity profiles. In order to correct this in the *Standard Smagorinsky model* of FLUENT a slightly different Smagorinsky lengthscale is applied which accounts for the log-layer:

$$l_S = min\Big(\kappa d,\, C_S V^{1/3}\Big) \tag{A.89}$$

in which:

κ: von Kármán constant

d: distance to the closest wall

C_S: the Smagorinsky constant, here $C_S = 0.1$

V: volume of the computational cell

However, this model still cannot reproduce the correct wall asymptotic behaviour (very close to the wall $\langle u'v' \rangle \sim -y^3$, see in Figure A.7) for wall bounded flows. As such, in the simulations the Wall-Adapting Local Eddy-Viscosity (WALE) Model was used which can correctly model this area as well. The detailed description of the model can be found in 12.9.3 FLUENT [22].

Near wall treatment in LES and its implementation in FLUENT

In LES, for he near wall treatment two fundamentally different approaches exist:

- LES with near wall resolution (LES-NWR): a very fine grid is used which is capable of resolving the 80 % of the turbulent kinetic energy even in the whole wall region.
- LES with near wall modelling (LES-NWM): a coarser grid is used and like in the introduced FLUENT's models in the wall region a smaller lengthscale is applied when the mesh is not fine enough

Obviously, LES-NWR gives more accurate results. Nevertheless, resolving the boundary layer extremely increases the computational cost and beyond a Reynolds number LES-NWR is simply not feasible. To demonstrate this we estimate the required dimensionless grid spacing in the log-layer of a zero-gradient boundary layer (the one which was introduced in the RANS case) for Reynolds number of our simulation, i.e. for $Re = 140000$. Combining Prandtl's mixing length hypothesis with Equation (A.76) gives the required dimensionless grid spacing for a good resolved LES in the log-layer:

$$\triangle^{+}\left(y^{+}\right) \approx \lambda^{+}(y^{+}) = l_0^{+}(y^{+})\sqrt{10}Re^{-1/2} = \kappa y^{+}\sqrt{10}Re^{-1/2} \tag{A.90}$$

in which the terms with plus sign in the superscripts are made dimensionless by δ_ν.

Substitution of $Re = 140000$ gives:

$$\triangle^{+} \approx 0.001833y^{+} \tag{A.91}$$

In a mesh for LES calculation, as a rule of thumb, the growth rate between cells should be kept under 1.05 thus, the local refinements close to the walls imply global refinement of the grid, hence leading to a cost explosion.

In FLUENT the default LES wall functions use the linear relation between u^{+} and y^{+} in the viscous sublayer and in the log-layer the log-law is applied. In the buffer layer the two laws are blended by analogy to the RANS enhanced wall treatment. It is worth noting that these wall laws were deduced from the RANS equations, and hence applying them to LES means that in the wall adjacent cells the filtered velocity field is represented by the modelled mean velocity field. Although this does not seem to be theoretically correct, in practice, usually it gives good results, obviously with same limitations as for RANS. Alternatively, the Werner-Wengle wall functions can be used, which is a sort of two layer method based on the wall shear stress. In the simulations the default wall functions were used. The detailed description of the wall functions can be found in FLUENT User's Guide 12.10.6 [22]

Further closure models for LES

Due to the limitations of the Smagorinsky model, new models have been recently developed. Here we intend to give a brief summary about the two most important models.

The *dynamic Smagorinsky model* was introduced by Germano in 1991. The base of the method is that with applying a double filtering process on the velocity field $C_S\,(x_i\,,t)$ can be calculated. Hence this model accounts for the different lenghtscale regions. Additionally, in the calculation of τ^r_{ij}, $C_S\,(x_i,\,t)$ is introduced, unlike in the standard model where C^2_S was used. Consequently, the dynamic model also can capture the backscatter.

The normal and dynamic Smagorinsky models assume local equilibrium between the extracted energy at macroscales and the dissipated one at micro scales. This is the direct result of the algebraic nature of the models, that only incorporates information from the filtered flow field. In accordance with this τ^r_{ij} is related to $\overline{u_i}$ at the same time and in the neighbourhood of x_i. It is more realistic to account for history and non-local effect, so that similarly to the one-equation RANS models, instead of defining the subgrid mixing velocity as $l_S\overline{S}$, one can calculate the mixing velocity by solving an additional transport equation for k^R.

Although the dynamic Smagorinsky as well as a model which includes transport equation for k^R are capable of accurately modelling the turbulence in the residual motions, they all have their shortcomings too. The dynamic model can be unstable because of the backscatter and solving one more transport equation always raises the computational cost. Besides, in LES calculations the main goal is to resolve the energy containing range as much as it is possible. In such well resolved cases, the involved cost and complexity of these models are not justified by a guaranteed increase in accuracy.

B. Velocities in the wake

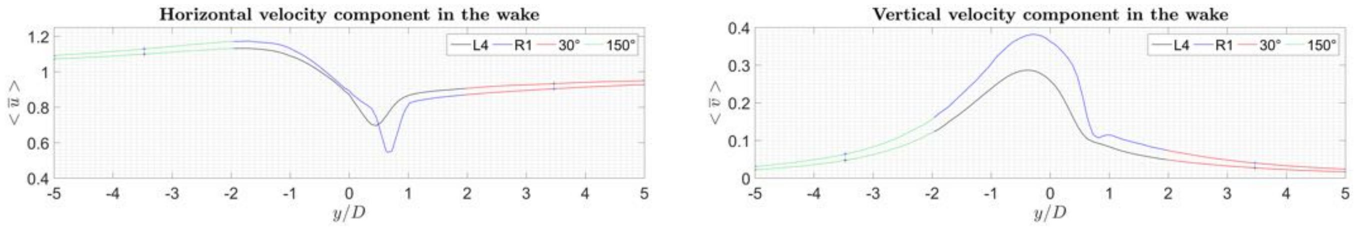

Figure B.1.: Velocities with R1 at 30° and 150°.

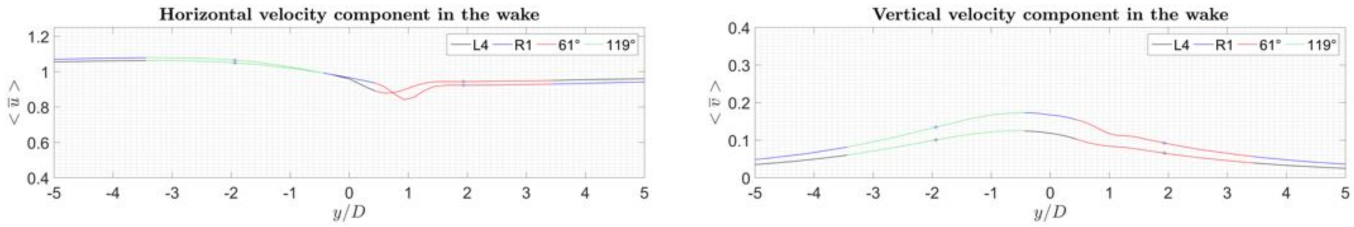

Figure B.2.: Velocities with R1 at 61° and 119°.

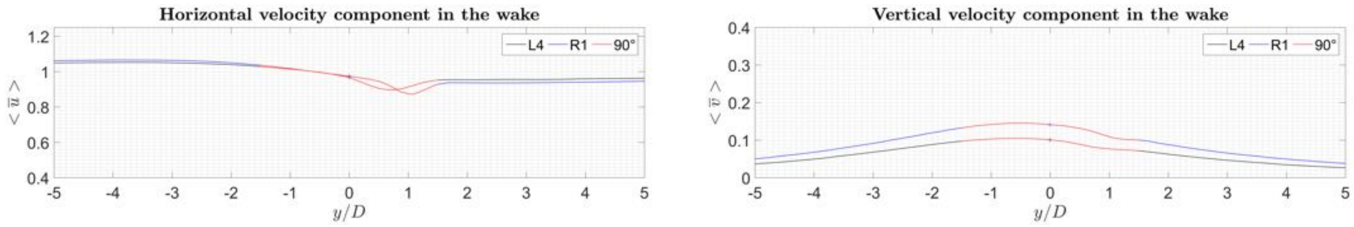

Figure B.3.: Velocities with R1 at 90°

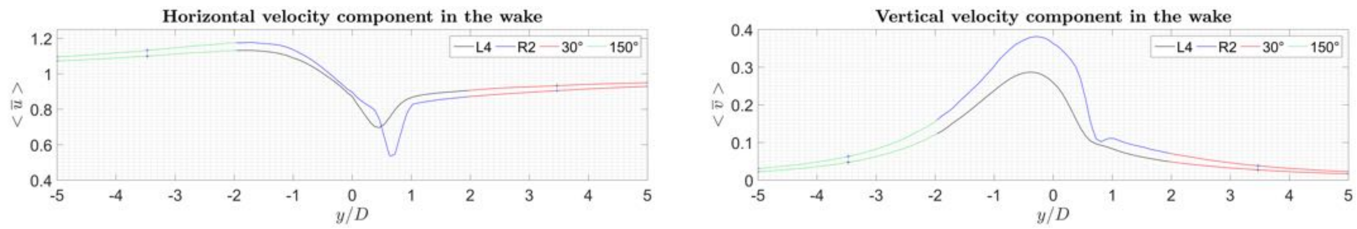

Figure B.4.: Velocities with R2 at 30° and 150°.

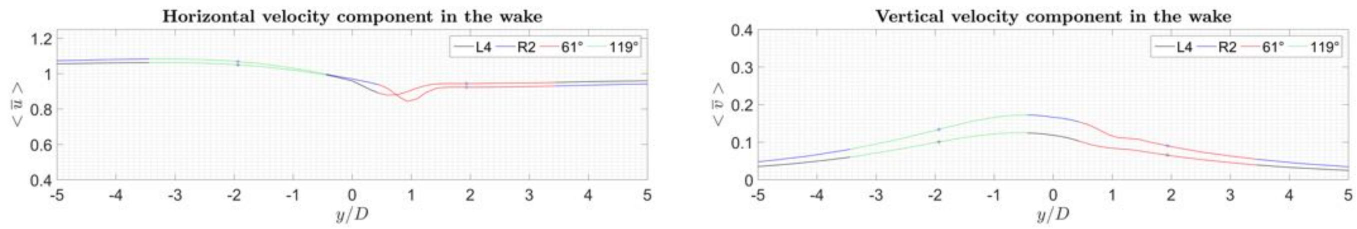

Figure B.5.: Velocities with R2 at 61° and 119°.

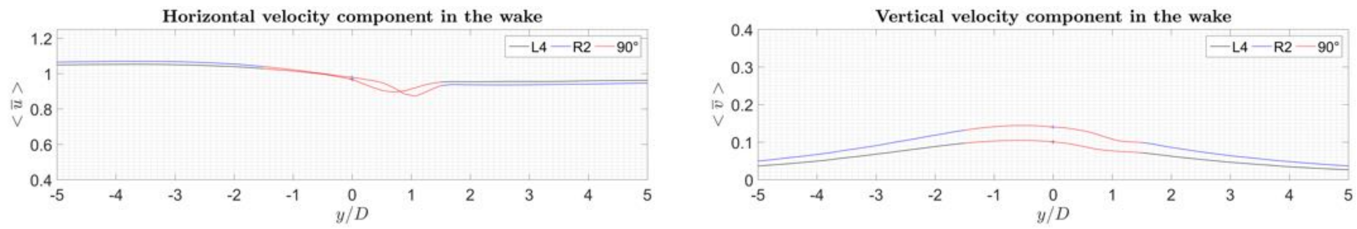

Figure B.6.: Velocities with R2 at 90°

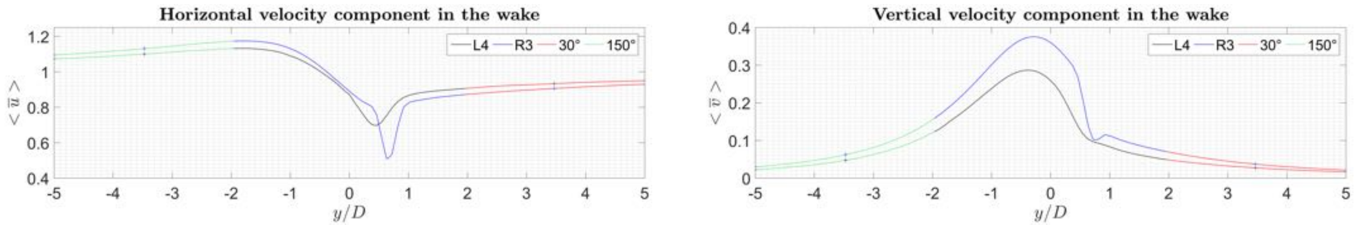

Figure B.7.: Velocities with R3 at 30° and 150°.

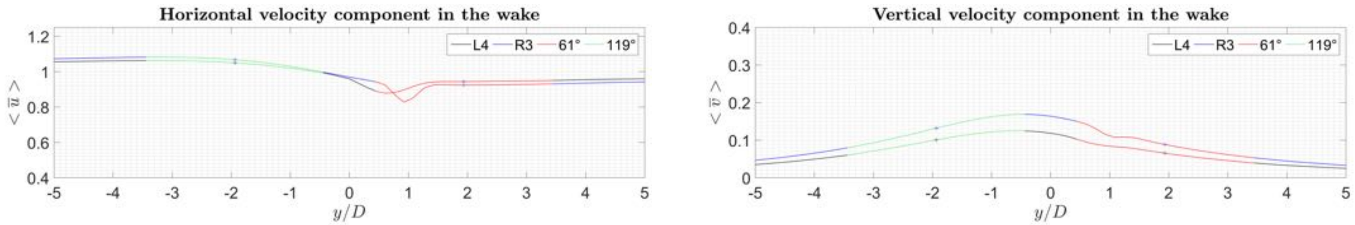

Figure B.8.: Velocities with R3 at 61° and 119°.

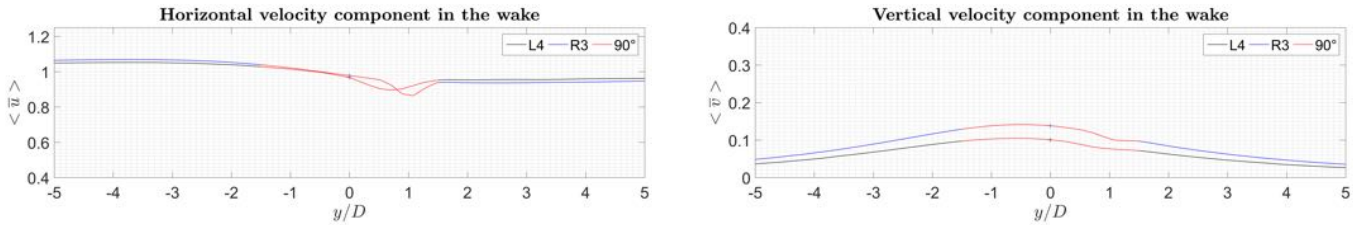

Figure B.9.: Velocities with R3 at 90°

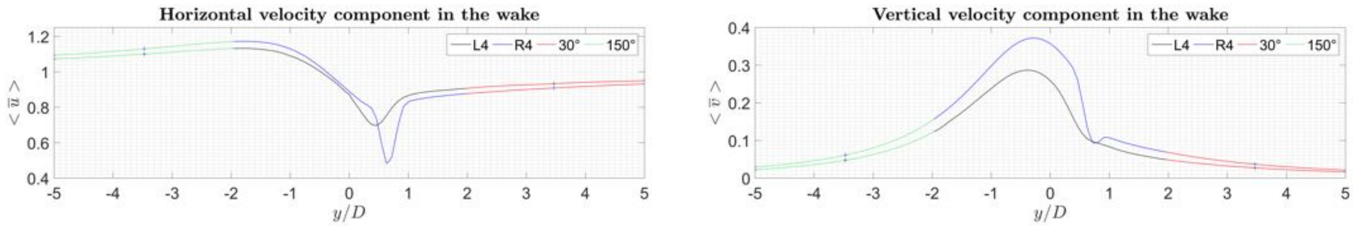

Figure B.10.: Velocities with R4 at 30° and 150°.

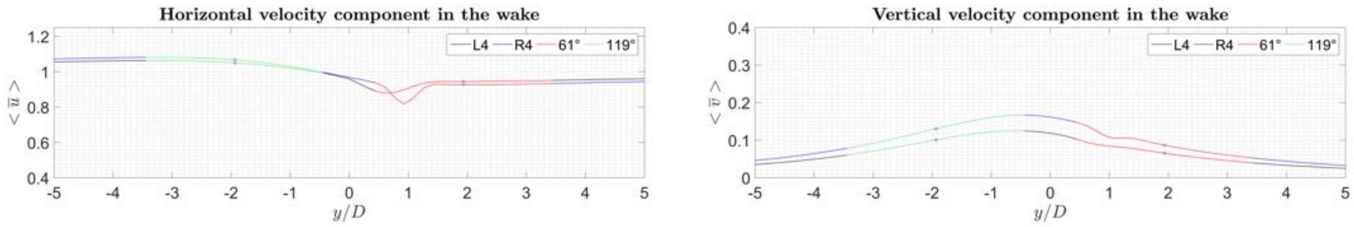

Figure B.11.: Velocities with R4 at 61° and 119°.

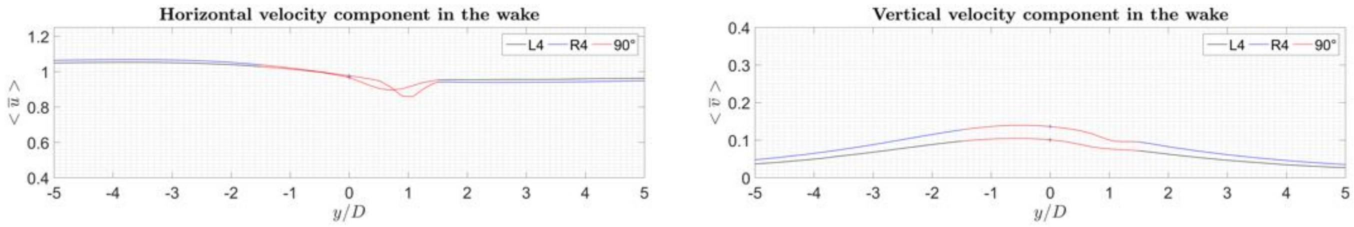

Figure B.12.: Velocities with R4 at 90°

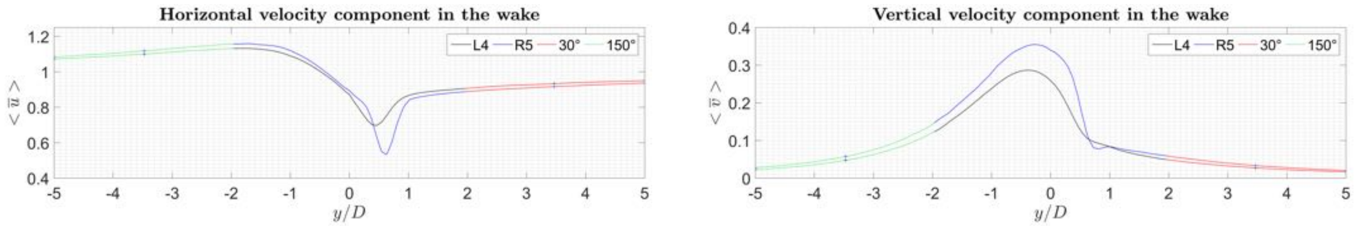

Figure B.13.: Velocities with R5 at 30° and 150°.

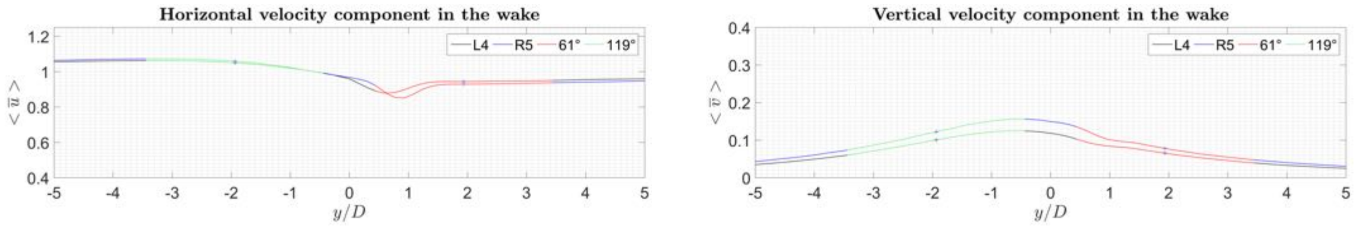

Figure B.14.: Velocities with R5 at 61° and 119°.

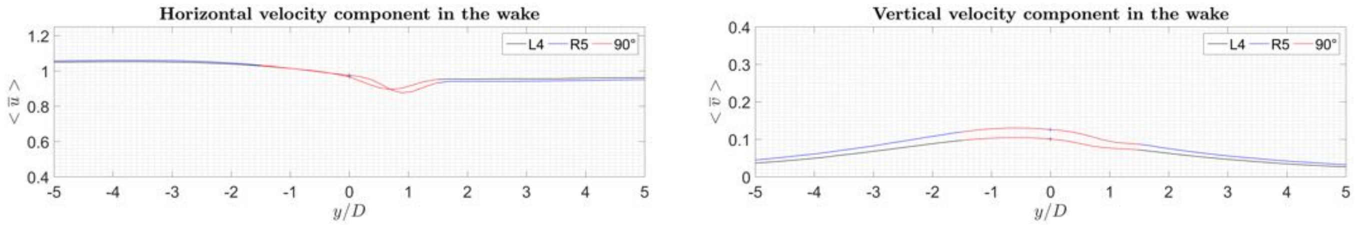

Figure B.15.: Velocities with R5 at 90°

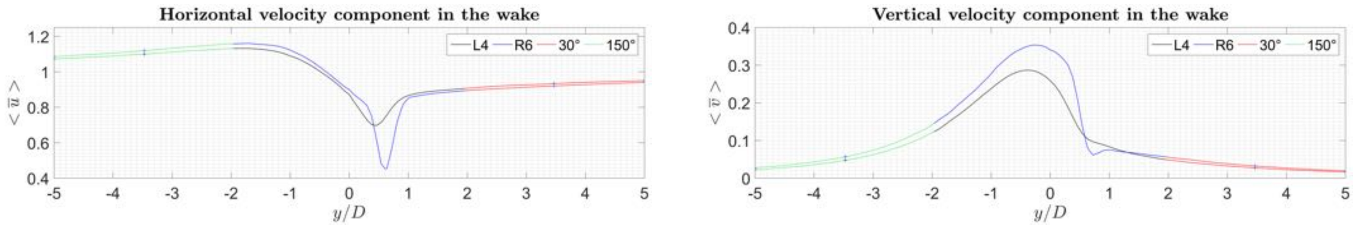

Figure B.16.: Velocities with R6 at 30° and 150°.

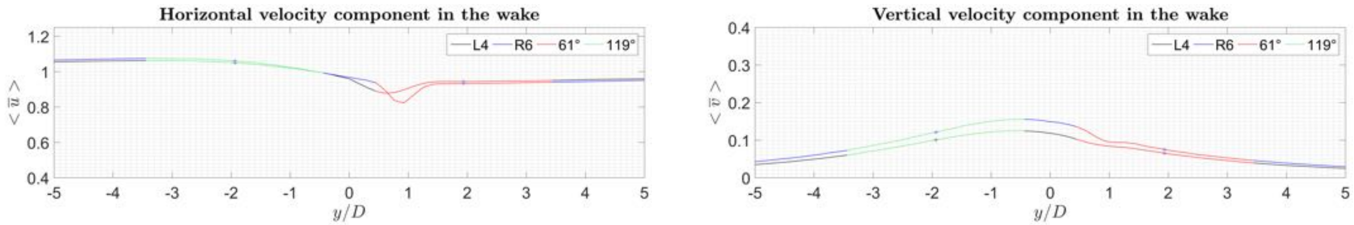

Figure B.17.: Velocities with R6 at 61° and 119°.

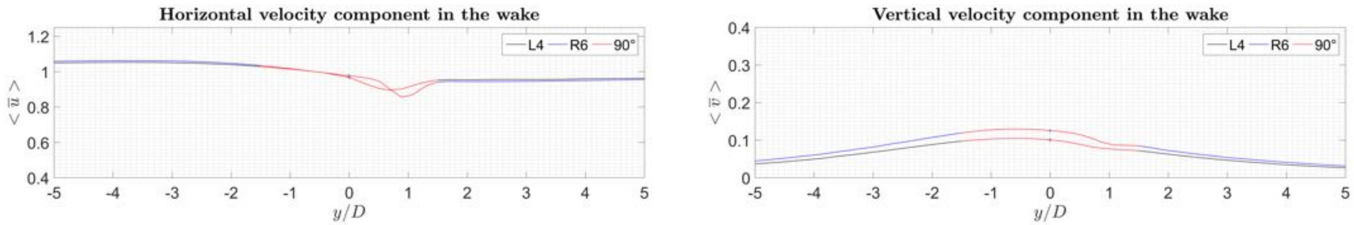

Figure B.18.: Velocities with R6 at 90°

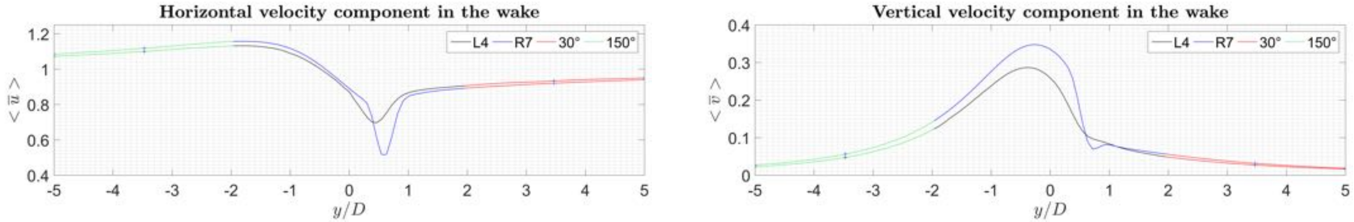

Figure B.19.: Velocities with R7 at 30° and 150°.

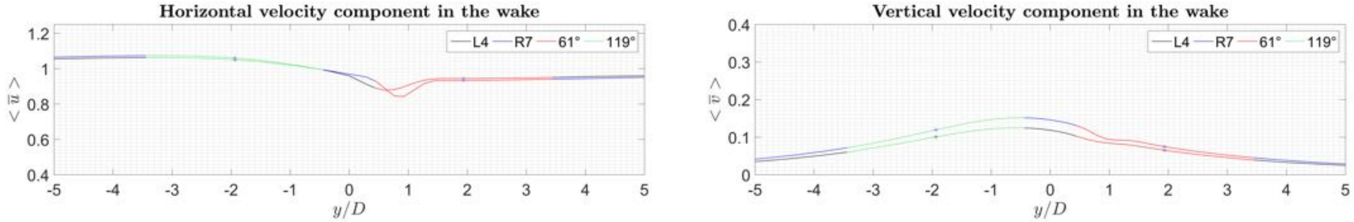

Figure B.20.: Velocities with R7 at 61° and 119°.

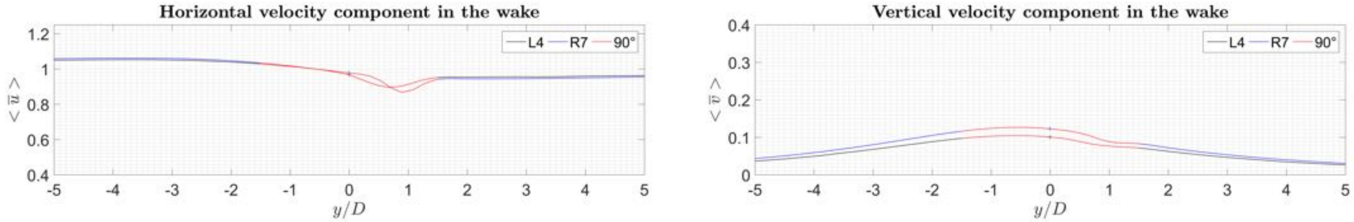

Figure B.21.: Velocities with R7 at 90°

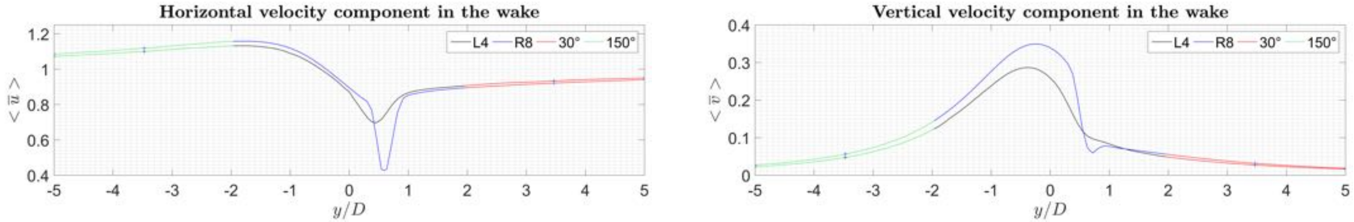

Figure B.22.: Velocities with R8 at 30° and 150°.

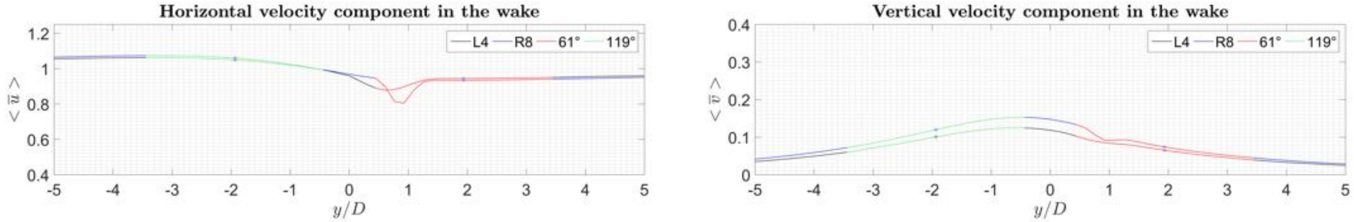

Figure B.23.: Velocities with R8 at 61° and 119°.

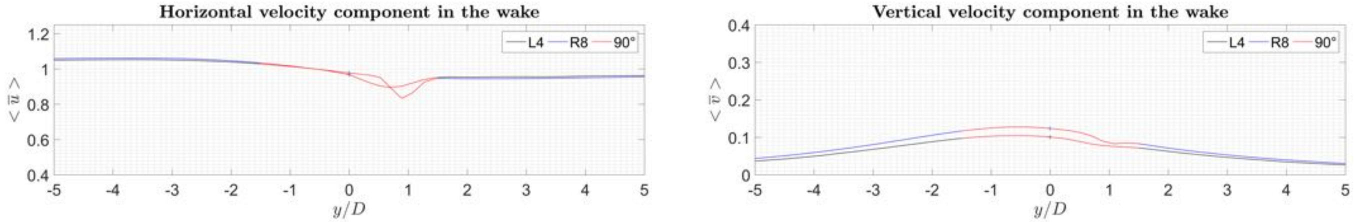

Figure B.24.: Velocities with R8 at 90°

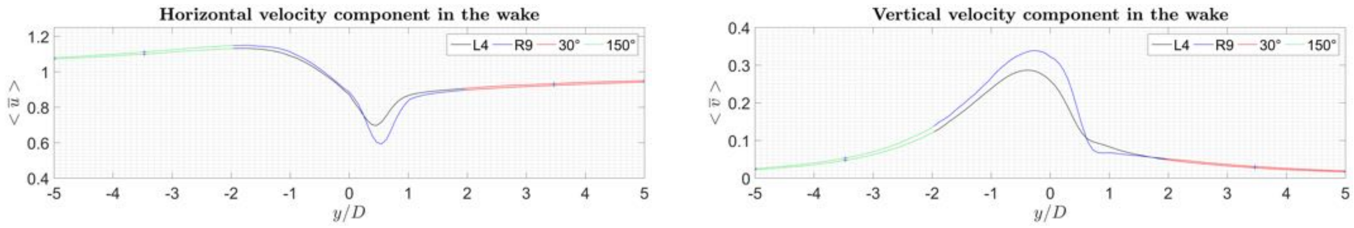

Figure B.25.: Velocities with R9 at 30° and 150°.

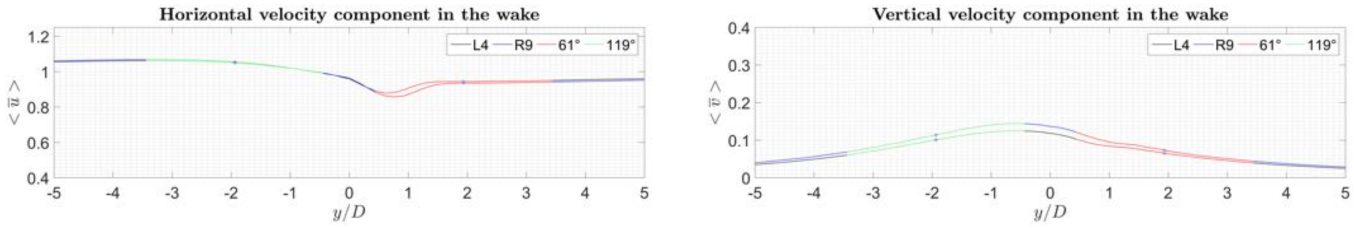

Figure B.26.: Velocities with R9 at 61° and 119°.

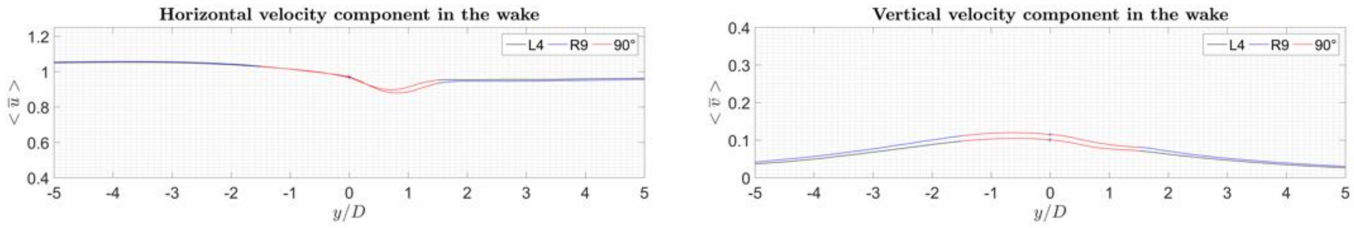

Figure B.27.: Velocities with R9 at 90°

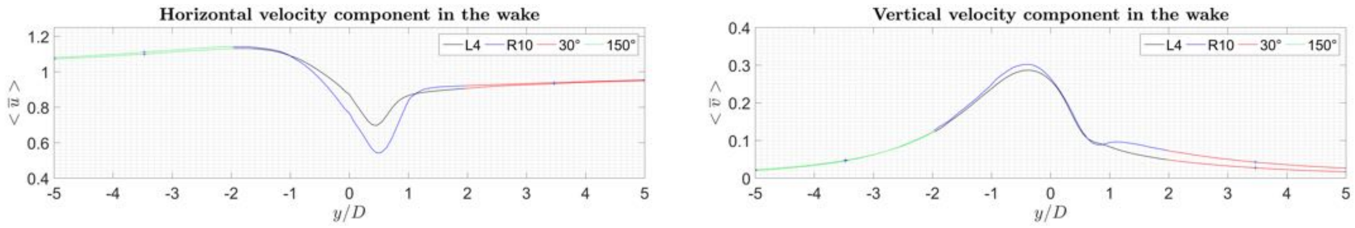

Figure B.28.: Velocities with R10 at 30° and 150°.

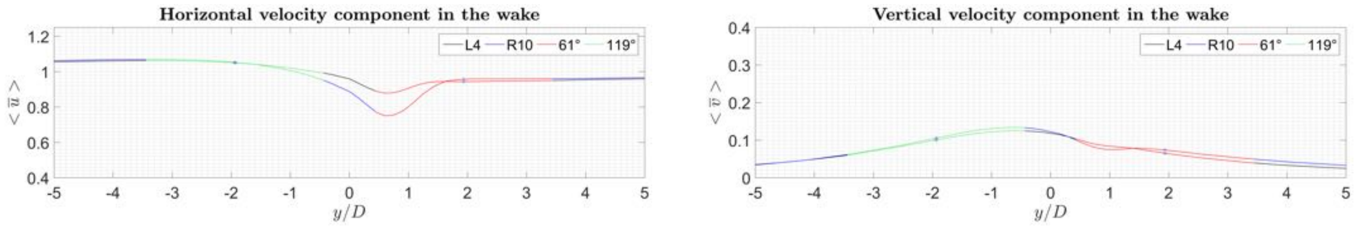

Figure B.29.: Velocities with R10 at 61° and 119°.

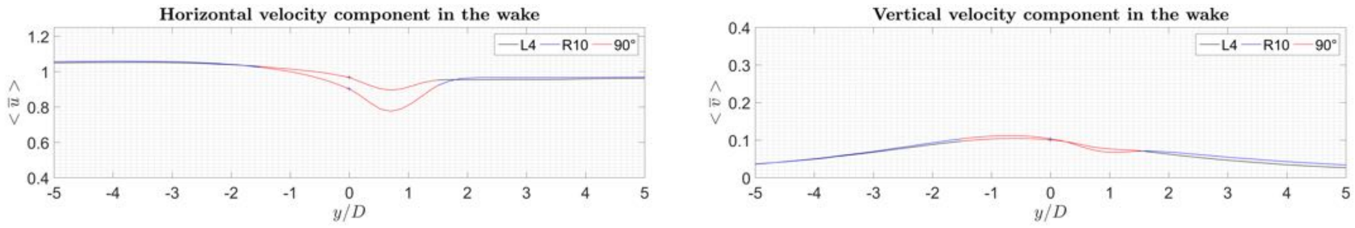

Figure B.30.: Velocities with R10 at 90°

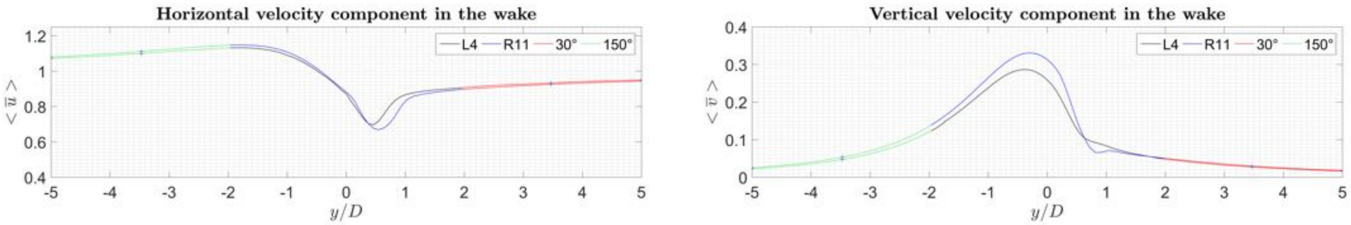

Figure B.31.: Velocities with R11 at 30° and 150°.

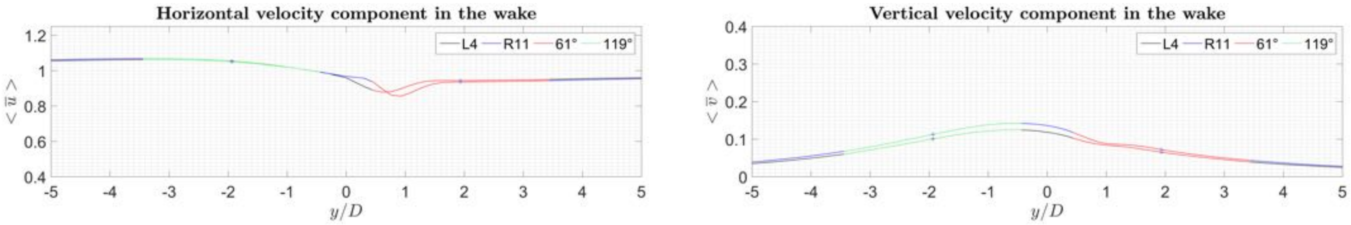

Figure B.32.: Velocities with R11 at 61° and 119°.

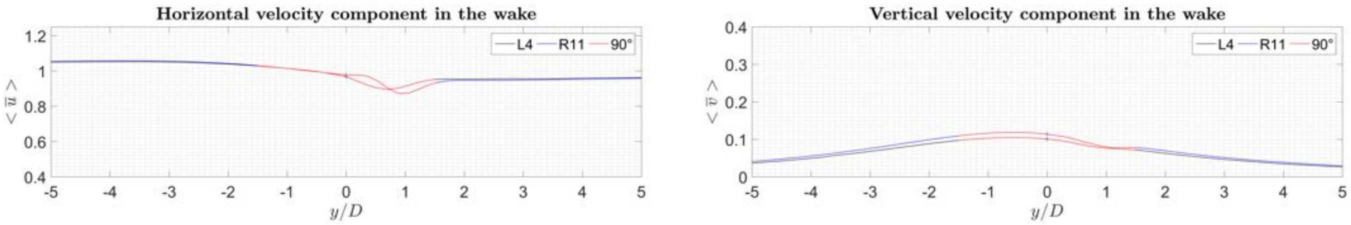

Figure B.33.: Velocities with R11 at 90°